Timing Diagnostics and Coherent Harmonics from a test-FEL

Cutic, Nino

2011

Timing Diagnostics and Coherent Harmonics from a Test-FEL

Nino Čutić

Doctoral Thesis
2011

Lund University

Timing Diagnostics and Coherent Harmonics from a Test-FEL

Printed in Sweden by Media-Tryck, Lund, 2011

MAX-lab, Lund University
P.O. Box 118
SE–221 00 Lund
Sweden

http://www.maxlab.lu.se

ISSN 0284-1258

ISRN LUNTDX-NTMX–1010–SE

ISBN 978-91-7473-106-4

Laser, eh, is about coherence, not power!
Rodolfo Bonifacio

ABSTRACT

The test free-electron laser (test-FEL) at MAX-lab in Lund demonstrated for the first time circularly polarized coherent femtosecond pulses at 66 nm wavelength. A 375 MeV electron bunch was seeded by a femtosecond laser at 263 nm and coherent harmonics were extracted in an APPLE-II type elliptical undulator. A thermionic gun with a barium oxide cathode was adapted for photocathode operation, and the performance of the gun was tested. Measurements showed the production of 200 pC of electrons with a normalized emittance of 5.5 mm mrad and a quantum efficiency of $1.1 \cdot 10^{-4}$. To ensure the electron bunch overlap with the 500 fs seed laser pulse and to measure the bunch length, an electro-optical spectral decoding setup was built. The bunch length of about 1 ps was measured and it was determined that the long-term drifts in timing were accelerator-related. Electro-optical spectral decoding was used for the first time for online feedback to stabilize the overlap between the laser pulse and the electron bunch. This stabilization ensured lasing of the FEL on every shot and contributed to the detection of higher linearly polarized harmonics (44 nm). This thesis presents an introduction to the processes that occur in the undulators: modulation, bunching and radiation. It describes the test-FEL setup and the emittance of an electron beam. Electro-optical spectral decoding is explained and its advantages and limitations are discussed. The feedback based on a simple controller is presented.

POPULÄRVETENSKAPLIG SAMMANFATTNING

I denna avhandling ges en introduktion till fyra artiklar där resultat från och delar av en frielektron-laser (FEL) beskrivs. Denna typ av laser skiljer sig från de konventionella lasrar de flesta av oss har träffat på, t.ex. i form av en laserpekare. Den första märkbara skillnaden är att frielektron-lasrar är stora, ofta flera hundra meter långa. De kräver en accelerator och långa magnetstrukturer, s.k. undulatorer, för att fungera. Istället för att använda material som kristaller, halvledare, gaser eller plasma, använder de istället fria obundna elektroner. Högenergetiska elektroner från acceleratorn förlorar lite energi och alstrar ljus i undulatorerna.

Den FEL som presenteras här är ca 60 m lång. Syftet med anläggningen är att studera produktion av ljus med korta våglängder och variabel polarisation. Polarisation är en viktig egenskap hos ljus med många tillämpningar inom vetenskap och teknik. Genom att använda den existerande acceleratorn på MAX-lab, en konventionell laser och två undulatorer, manipuleras elektronerna att alstra ljus med godtycklig polarisation och kortare våglängd än den konventionella laser som används för att starta processen. Växelverkan mellan elektronerna och ljus från den konventionella lasern förbättrar kvaliteten på ljuset från FELen. Metoden att starta frielektronlasern med en konventionell laser kallas seeding (sådd).

För att detta ska fungera måste man träffa elektronpulsen med en laserpuls i både tid och rum. Att överlappa dem rumsligt är inte så utmanande, men överlapp tidsmässigt kan vara det. Elektronpulsen är ungefär en tredjedels millimeter lång och laserpulsen ungefär en tiondels, och båda färdas med ljusets hastighet. Elektro-optisk laserteknik användes för att kontrollera och mäta det tidsmässiga överlappet mellan elektroner och laserpuls. Tekniken användes också för att, via återkoppling av laserns fördröjning, säkerställa överlapp för varje skott. Detta ger en klar förbättring av anläggningen till en mycket liten kostnad.

POPULAR SCIENTIFIC INTRODUCTION

This thesis presents an introduction to four papers describing the components and the results from a free-electron laser (FEL) at MAX-lab in Lund. This type of laser is very different from conventional lasers familiar to most of us, like laser pointers. The first noticeable difference is that FELs are very large. They consist of an accelerator and a long magnetic devices called undulators. They can easily be hundreds of meters long. Instead of using materials like crystals, semiconductors, gases or plasmas, this laser instead uses electrons themselves. The high-energy electrons from the accelerator feed the FEL and, at the expense of a slight loss in energy, produce light in undulators.

The FEL presented in this work is about 60 m long, and the aim of these studies was to investigate the production of short-wavelength light with variable polarization. Polarization is an important property of light applied widely in technology and science. Using the existing MAX-lab accelerator, a conventional laser and two undulators, the electrons were manipulated to produce light with arbitrary polarization and wavelength shorter than that of the conventional laser used in this process. The interaction of electrons with a laser pulse from the conventional laser improves the properties of the light produced by the FEL. Starting the free-electron laser with a conventional laser is called seeding.

For seeding to work, it is necessary for the laser pulse to hit the bunch of electrons exactly in time and position. Overlapping the pulse spatially is not so challenging, but temporal overlapping can be. The electron bunch is about a third of a millimeter long and the laser pulse about a tenth of a mm, and both are traveling at speed of light. An electro-optical laser technique was used to measure and achieve the overlap. It was also used to develop feedback that ensures overlap on every shot. This significantly improved the operation of the test-FEL at a very low cost.

PREFACE

I started my PhD studies in May 2007, on a project called MAXLAS, which was a collaborative project between Lund University, the Lund Laser Centre and MAX-lab. MAXLAS was an EU funded Marie Curie Early Stage Research Training project. The first three years of my position were financed by the EU (Marie Curie) and the last year by Lund University. The work was carried out at MAX-lab, which is a Swedish national laboratory in Lund. The main objective of my PhD studies was to build an electro-optical system that could be used to measure the arrival time of a bunch of electrons relative to the seed laser pulse, and possibly measure the electron bunch length. Considering the limited number of people engaged in this project, the work actually spanned almost all aspects of running the test-FEL, from the electron gun to the spectrometer. I participated in the daily running and measurements and essentially everything that involved the test-FEL. This allowed me to obtain a broader understanding of the whole project and the interesting physics behind it. Working at MAX-lab on this project was varied and interesting, and I am glad that I had the chance to participate in it. The most impressive achievement of the FEL team was the creation of at 66 nm in circular polarization in the spring of 2010 – a small world record, at least until FERMI in Trieste starts operating in circular mode.

Scope and outline of this thesis

This thesis includes four of several publications I have worked on. They were published during my time in Lund and are about the test-FEL. An introduction to the papers and the related theory are given here, on a level that a new graduate student should be comfortable with. The intended audience is researchers and students in groups in a similar field of research. An effort has been made to present material that concerns only the test-FEL, but the principles are of interest and useful for other projects.

This thesis is divided in six chapters, two of which are Introduction and the chapter Summary and Outlook. The two most important are Chapter 2 (Coherent harmonic generation) and Chapter 5 (Electro-

optical spectral decoding). Chapter 2 presents the theory behind the test-FEL, and is related to Paper **II** and slightly to Paper **I**. Paper **II** describes how the harmonics are produced and, for the first time, the production of 66 nm light with circular polarization. Chapter 5 describes the electro-optical technique that functions as a longitudinal diagnostic and is most related to Papers **III** and **IV**. Chapter 4 provides a short introduction to emittance and a technique for measuring the emittance. The material in that chapter is most relevant for Paper **I**. Chapter 3 describes the hardware of the test-FEL and is important and related to all the other chapters. The papers follow the development of the project and they cover different aspects of one machine. For example, the work presented in Paper **II** depended highly on the work that resulted in Papers **I**, **III** and **IV**. Some of the chapters are concluded with a short discussion that presents the wider scope in which that chapter relates to other chapters and papers.

Acknowledgements

I am grateful to many people who have supported me and helped me during these years. To Sverker Werin who was my thesis supervisor, for being available whenever I needed his advice and for asking tricky questions that almost always meant I had to go dig deeper into the subject. He managed to find a good balance between supervision and allowing me to work independently, which made the work more engaging and fruitful, and increased my ability to contribute to the group. I am also grateful to my co-supervisor Anne L'Huillier for her optimism, encouragement and great courses in lasers.

I would like to thank everyone who worked on the test-FEL: Filip Lindau, for his extensive contribution to the electro-optical setup, for improving my knowledge about lasers as well as good company and sense of humor; Sara Thorin for her help, and for dealing with the output of simulation codes that most of us tried to avoid; Mathias Brandin, for being a friend and showing me around MAX-lab and accelerator during my early days; Francesca Curbis, Christian Erny, Karsten Holldack and Erik Mansten for their company and contributions to the project; and Johannes Barhdt, for his help and comprehensive answers to all my questions about undulators.

The MAXLAS project included five other students financed by Marie Curie Actions who started at about the same time as I did on different projects. Because of our common interests and being in the same situation we became friends, which helped fill the social gap when moving to another country: Marko Swoboda, Jörg Schwenke, Ralf Nüske, Jens Uhlig and Guillaume Genoud. I would also like to thank my MAX-lab "co-combatants" for their help, advice and company: Magnus Sjöström and Anders Hansson, as well as Magnus Lundin, Simon Leemann, Dionis Kumbaro, Erik Wallén, Elsayed Elafifi, Annika Nyberg, Henrik Enquist and Mikael Eriksson. I

would like to thank MAX-lab personnel, specially Elisabeth Dahlström and Helena Ullman, and those at the Lund Laser Center who helped with experiments and equipment: Xinkui He and Anders Persson. Thanks to Dinh C. Nguyen from Los Alamos for a great course on free-electron lasers during USPAS in Albuquerque; and Bernd Steffen and Laurens Wissmann from DESY for fruitful discussions on electro-optical schemes.

I would like to thank my diploma work advisor Slobodan Milošević and all my teachers and professors who, through many years of effort, have made it possible for me to complete this thesis. Zahvaljujem se mojim roditeljima, sestri i široj obitelji na podršci tijekom svih ovih godina. Thanks my to wife Lali, for her proof reading and suggestions, and I apologize for being mentally absent while writing this thesis. Love you Teddy.

List of Publications

This thesis is based on the following papers, which will be referred to by their Roman numerals in the text.

I **Photocathode operation of a thermionic RF gun**
S. Thorin, N. Čutić, F. Lindau, S. Werin and F. Curbis.
Nucl. Instrum. Meth. A **606**, 291–295 (2009).

II **Vacuum ultraviolet circularly polarized coherent femtosecond pulses from laser seeded relativistic electrons**
N. Čutić, F. Lindau, S. Thorin, S. Werin, J. Bahrdt, W. Eberhardt, K. Holldack, C. Erny, A. L'Huillier and E. Mansten.
Phys. Rev. Spec. Top. Accel. Beams **14**, 030706 (2011).

III **Characterization of the arrival time jitter at the MAX-lab test-FEL using electro-optical spectral decoding**
N. Čutić, C. Erny, F. Lindau and S. Werin.
Nucl. Instrum. Meth. A **626–627**, 16–19 (2011).

IV **On-line arrival time and jitter measurements using electro-optical spectral decoding**
N. Čutić, F. Lindau, S. Werin and E. Mansten.
Proceedings of FEL10, Malmö, Sweden, THOA4 (2010).

ADDITIONAL PUBLICATIONS

The work in this thesis also resulted in the following publications.

1 **Seeding of the test-FEL at MAX-lab**
N. Čutić, F. Curbis, F. Lindau, S. Thorin and S. Werin.
Proceedings of EPAC08, Genoa, Italy, MOPC006 (2008).

2 **Progress of the commissioning of the test-FEL at MAX-lab**
S. Thorin, F. Curbis, N. Čutić, F. Lindau, S. Werin, M. Abo-Bakr, J. Bahrdt and K. Holldack.
Proceedings of EPAC08, Genoa, Italy, MOPC032 (2008).

3 **Commissioning of the test FEL at MAX-lab**
F. Curbis, N. Čutić, F. Lindau, S. Thorin, S. Werin, M. Abo-Bakr, J. Bahrdt and K. Holldack.
Proceedings of FEL08, Gyeongju, Korea, FRAAU06 (2008).

4 **Characterisation of the beam from thermionic RF-gun adapted for photo cathode operation**
S. Thorin, N. Čutić, F. Lindau, S. Werin and F. Curbis.
Proceedings of FEL09, Liverpool, UK, TUPC33 (2009).

5 **The test FEL facility at MAX-lab**
S. Werin, N. Čutić, F. Lindau, S. Thorin, J. Bahrdt, K. Holldack and C. Erny.
Proceedings of FEL09, Liverpool, UK, TUPC34 (2009).

6 **An electro-optical system for MAX-lab test-FEL facility**
N. Čutić, F. Lindau, S. Thorin, S. Werin and C. Erny.
Proceedings of FEL09, Liverpool, UK, WEPC79 (2009).

7 **The MAX-IV injector as a soft X-ray FEL driver**
S. Werin, N. Čutić, M. Eriksson, F. Lindau and S. Thorin.
Proceedings of FEL10, Malmö, Sweden, WEPA11 (2010).

8 **First results of coherent harmonic generation at the MAX-lab test FEL**
N. Čutić, F. Lindau, S. Thorin, S. Werin, C. Erny, A. L'Huillier, E. Mansten, J. Bahrdt and K. Holldack.
Proceedings of FEL10, Malmö, Sweden, WEOA4 (2010).

ABBREVIATIONS

APPLE	Advanced Polarizing Photon Light Emitter
B-field	Magnetic field
BBO	Beta Barium Borate
CCD	Charge-Coupled Device
CEP	Carrier-Envelope Phase
CHG	Coherent Harmonic Generation
CPA	Chirped Pulse Amplification
DESY	Deutsches Elektronen-Synchrotron
DFG	Difference Frequency Generation
DS	Delay Stage
E-field	Electric field
EO	Electro-Optical
EOSD	Electro-Optical Spectral Decoding
EOTD	Electro-Optical Time Decoding
FEL	Free Electron Laser
FLASH	Free-electron LASer in Hamburg
FWHM	Full Width at Half Maximum
GaP	Gallium Phosphide
GVD	Group Velocity Dispersion
HGHG	High Gain Harmonic Generation
HWP	Half-Wave Plate
HZB	Helmholtz Zentrum Berlin
IR	Infra-Red
LCLS	Linac Coherent Light Source
LLC	Lund Laser Centre
MO	Master Optical Oscillator
PID	Proportional Integral Derivative (controller)
QWP	Quarter-Wave Plate

rms	Root Mean Square
SASE	Self-Amplified Stimulated Emission
SFG	Sum Frequency Generation
TDC	Transverse Deflecting Cavity
THG	Third Harmonic Generation
UV	UltraViolet
VUV	Vacuum UltraViolet
XFEL	X-ray Free Electron Laser
YAG	Yttrium Aluminium Garnet
ZnTe	Zink Telluride

CONTENTS

Papers

CHAPTER 1

INTRODUCTION

The history of free-electron lasers (FELs) begins after the Second World War. In 1947 John R. Pierce published a paper on exponential gain in traveling wave tubes [1], and periodic magnetic structures (undulators) appear in the publications of Ginzburg and, independently, Motz in the 1950's [2]. Improvements continue, Phillips noticed that density modulation of electron beam can be achieved by interaction with transverse components of RF fields [3]. A historical overview of these contributions can be found in [4]. Since so many people have contributed to their development, it would not be fair to say that the FEL was discovered by one single person, although John Madey comes closest, with his paper published in 1971 [5]. He also demonstrated the intensity gain of the FEL signal at Stanford. Colson showed that Madey's theory could be simplified [6]. The technology of FELs received a further boost thanks to the Strategic Defense Initiative by the US in the 1980's, with plans to use FELs to shoot down nuclear missiles. Modern FELs for scientific purposes have developed into research facilities, similar to synchrotron light sources, where users come to perform their measurements. The more well-known of these are FLASH in Germany, XFEL in Japan and LCLS in the US, which are pushing wavelength (and engineering) frontiers.

The first conventional laser was produced in 1957. Q-switching as a method of generating high peak powers was demonstrated in 1962 [7]. Mode locking opened the doors for femtosecond pulses in 1964 [8], and chirped pulse amplification in 1985 allowed significant improvement is laser intensity [9]. The frontier of attosecond pulses was opened in 1987 with high harmonic generation [10, 11], and the use of such pulses together with free-electron lasers has recently been achieved [12].

Seeded FELs employ a combination of developments in FELs and conventional lasers. The coherence qualities and high power of conventional laser are used to improve the properties of FEL light. Methods of seeding are available only at wavelengths where coherent

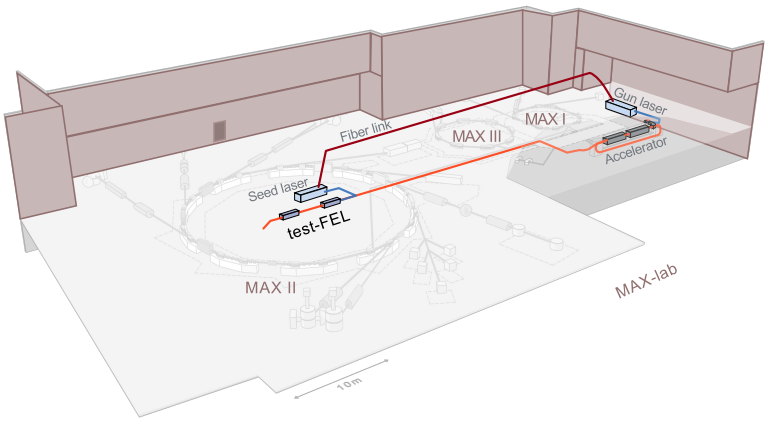

Figure 1.1. *Layout of MAX-lab. The accelerator used for all three rings, nuclear physics experiments and the test-FEL is in the basement. The test-FEL is positioned inside the MAX II ring and uses the radiation shielding of the ring. This allows easy access to the components of the FEL.*

lasers are available.

The test-FEL at MAX-lab is a seeded free-electron laser, and it was constructed with the goal of gaining experience in this field of research, and developing a source of vacuum-ultraviolet light with variable polarization. The project is a joint venture between the Lund Laser Centre (LLC), MAX-lab and the Helmholtz Zentrum Berlin (HZB), which provided the undulators. The undulators are positioned inside the MAX-II ring. Apart from its beam dump, the test-FEL does not have separate radiation shielding, but shares the shielding with the ring. The accelerator serves three storage rings, nuclear physics research and the test-FEL. The layout of the lab is shown in Figure 1.1. In order to generate high peak currents, the electron gun (source of electrons), which operates thermionically, is used as a photocathode gun. The electrons are accelerated to 375 MeV, compressed to about 1 ps and transported to the undulators.

The undulators consist of series of permanent magnets. They are constructed in such a way that the magnetic field they produce is perpendicular to the axis of the undulator but alternates in direction along the axis. An electron beam traveling along the axis will thus be influenced by an alternating magnetic field. The electrons produce light in the direction of the electron beam (i.e. the forward direction). The wavelength of the light depends on the energy of electrons, the period of the magnetic field (also called the undulator period) and the strength of the magnetic field. The intensity of the light can be significantly increased by bunching the electrons into small microbunches, separated by one wavelength of the light.

CHAPTER 2

COHERENT HARMONIC GENERATION

This chapter describes the generation of coherent harmonics. A scheme in which the interaction between relativistic electrons and a laser pulse inside an undulator is used to induce bunching of electrons within the electron bunch, with a period of the wavelength of the laser light. Higher harmonics of this bunching are then used to produce light in another undulator at a frequency that is a harmonic of the laser.

2.1 Introduction

This chapter is divided into three main parts that describe modulation, bunching and radiation. All three processes take place throughout the undulators and one cannot easily separate them from each other. However, they are descibed in a certain order since their importance on the final result changes along the way. Modulation is described first, followed by bunching and finally radiation.

As we will see in the radiation section the goal is to achieve grouping, or bunching, of electrons into small microbunches inside

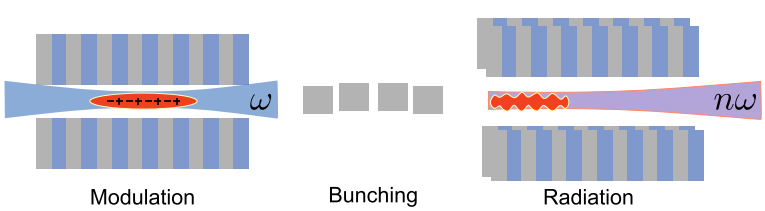

Figure 2.1. *Overview of coherent harmonic generation. In the first radiator (modulator) the energy within the bunch is modulated using a seed laser pulse. Energy modulation is converted to density modulation in the first undulator and the dispersion chicane. The radiation is extracted at a higher harmonic from the second undulator.*

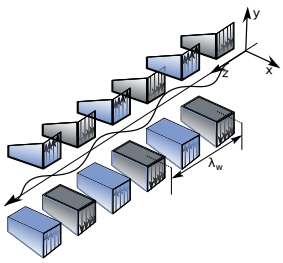

Figure 2.2. *The coordinate system used. Electrons travel in the z-direction and wiggle in x, while their y-coordinates remain constant.*

the electron bunch in such a way that the distance between microbunches in the laboratory frame equals the wavelength of the light that is to be produced. The distance can also be an integer multiple of the wavelength of the light that is being produced, in which case we talk about harmonics. Microbunching will lead to coherence of the light pulse produced, resulting in a huge increase in power. To reach this goal we first modulate the energy of electrons within the bunch and then use the difference in energy to make some of the electrons travel a longer path, and some of them a shorter path, through a series of magnets. In order to achieve modulation, the electrons must interact with a light field inside an undulator. This light can be produced by the electrons themselves, or we can add a laser pulse in the first undulator. If we add the laser the process will start faster and the length of the first undulator can be shorter, although these are not the only advantages of using a laser instead of the light spontaneously produced by the electrons. The first undulator is *the modulator*. The second undulator, *the radiator*, is used to extract the radiation at a multiple of the original laser frequency. Throughout this thesis, the term undulator will be interchangeably used with the term wiggler[1].

2.2 Modulation

Modulation is a process in which the energy of the electrons within the bunch is modulated (changed) so that certain parts of the bunch have excess energy, while other parts have less energy than the average. These domains are interleaving. The excess or lack of energy is relative to the resonance energy level set by the resonance condition (explained in 2.2.2). The energy of the electrons is influenced by the light present inside the undulator. The light in our case is generated by an external laser. The way in which the electrons travel through an undulator is crucial for the ensuing energy exchange between the light and electrons.

In this section we solve the equations of motion for an electron traveling through an undulator. This is given special attention since the nature of electron movement causes the production of harmonics of radiation in planar undulators, but not in helical undulators. This is addressed in the chapter on radiation (Section 2.4). Once the equations of motion have been solved, we add the laser field and require that the energy of the electrons is changed (i.e. that the laser field does some work). This will lead to the simple pendulum-like Hamiltonian for the whole process. Analysis of the phase space then gives a somewhat clearer picture of what leads to microbunching. The processes

[1] This is because these two are similar, the only difference between them being the angle through which they force the electrons to "wiggle" relative to the opening angle. This ratio of angles is given by the K-parameter which is discussed later. Undulators have K-parameters smaller than one, while wigglers have K-parameters much higher than one. Our undulators/wigglers have K-parameters comparable to one.

described are those taking place in the first undulator of our test-FEL, and provide the background for modulation testing (Paper **II**).

It is very important to stress that these equations are not complete. The equations we are about to consider stem from the Lorentz equation and describe the motion of electrons within an undulator and a light field [6]. Maxwell's equations must be included, and they lead to a description in which energy is conserved. When including Maxwell's equations it is necessary to deal with two additional equations that describe how the light field changes when the electrons emit radiation, or gain energy from the field [13, 14]. These equations are not treated here, since the modulation can be explained without them[2]. When it comes to radiation, Maxwell's equations are implicitly included, and are not presented explicitly in this thesis. The additional two equations are absolutely crucial for the description of X-ray free-electron lasers since seed pulses are not available, and the only way of generating X-ray light for the electrons to interact with is to produce it from the electrons themselves.

In the following section the motion of electrons through a planar undulator, and their simultaneous change in energy is described. It will be shown that the trajectory of electrons in the reference frame moving with average electron velocity has a shape resembling the number 8. Although highly relativistic electrons move almost at the speed of light, the average velocity will be slightly lower due to the undulator. This is because the electrons "wiggle" which reduces their longitudinal velocity. This means that the light entering the undulator will overtake, or slip past the electrons since it is traveling at the speed of light; this is called *slippage*. The transverse oscillations of electrons relative to the oscillations of the laser field, specifically the phase between them, will determine the exchange of energy between the laser and electrons. One way to ensure that this energy exchange does not die out due to slippage is to apply the resonant condition, which requires that electrons travel one wiggle period while the light travels that wiggle period plus one more light period (Figure 2.6).

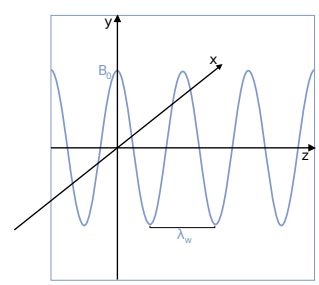

Figure 2.3. *Idealized 1D magnetic induction inside an undulator with a period of λ_w.*

2.2.1 Electron motion in an undulator without a laser field

We assume a planar undulator/wiggler with a periodic magnetic field of the form (as in Figure 2.3)

$$\mathbf{B} = B_y\,\hat{\mathbf{y}} = B_0\cos(k_w z)\hat{\mathbf{y}} \tag{2.1}$$

where the undulator wave number $k_w = 2\pi/\lambda_w$ is given by the length of a wiggler period λ_w (typically centimeters). The wiggler has N_w periods. In order to solve the motion of an electron inside the wiggler one can start from the Lorentz force:

$$\mathbf{F} = e\,B_y\,(\hat{\mathbf{x}}v_z - \hat{\mathbf{z}}v_x) \tag{2.2}$$

[2] In case of a seeded FEL.

which leads to only two coupled equations for the x and z coordinates:

$$\gamma m \ddot{x} = e\, B_y\, v_z \tag{2.3}$$
$$\gamma m \ddot{z} = -e\, B_y\, v_x \tag{2.4}$$

There is no motion in the y-direction. We take $v_x \ll v_z$ since the magnetic (B) field is such that v_x never becomes significant (wiggle angles are always very small). We use the approximations $v_x \ll c$, $v_z \approx \beta c$, and express v_x as

$$v_x = \frac{\mathrm{d}x}{\mathrm{d}t} = \frac{\mathrm{d}z}{\mathrm{d}t}\frac{\mathrm{d}x}{\mathrm{d}z} = v_z x' \tag{2.5}$$

where one more differentiation, while keeping v_z constant, leads to

$$\ddot{x} = v_z^2 x'' = c^2 x'' \tag{2.6}$$

With this and equation (2.3) we obtain the second derivative of x with respect to z:

$$x''(z) = \frac{e\,B_0 v_z}{\gamma m c^2}\cos(k_w z) \approx \frac{e\,B_0}{\gamma m c}\cos(k_w z) \tag{2.7}$$

Integrating twice leads to the transverse position

$$x(z) = -\frac{e\,B_0}{\gamma m c k_w^2}\cos(k_w z) + x_0' z + x_0 \tag{2.8}$$

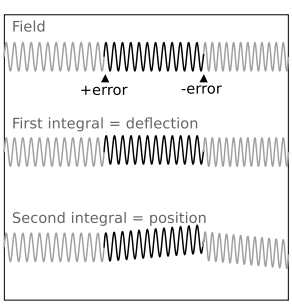

Figure 2.4. *Errors in the undulator lead to offsets in deflection and position. Undulators usually have coils with DC current running through them that correct for the nonzero integral of the field. The main contribution to this offset is from fringe fields (at the ends of the undulator).*

In the absence of field errors in the undulator[3] (see Figure 2.4), assuming the correct initial position and momentum of the electron, and introducing the K-parameter

$$K \equiv \frac{e\,B_0}{m c k_w} \tag{2.9}$$

which depends only on the undulator, the transverse position can be written:

$$x(z) = -\frac{K}{\gamma k_w}\cos(k_w z) \tag{2.10}$$

Using $v_x = v_z x' \approx c x'$ gives the horizontal velocity as

$$v_x(z) = \frac{cK}{\gamma}\sin(k_w z) \tag{2.11}$$

We can now find changes in v_z from v_x by substituting v_x into

$$v^2 = v_x^2 + v_z^2 = \beta^2 c^2 \tag{2.12}$$

[3] If the B-field, described by a cosine, would due to an imperfection get a phase shift by a +error and later along the undulator lost the phase shift (-error) this would in first integral contribute to deflection of the electron while second integral would contribute to the position offset.

Assuming conservation of energy ($\beta = \text{const.}$) any transverse motion (wiggling) comes at the expense of axial/longitudinal speed v_z. Transverse motion of the electrons inside the wiggler reduces their longitudinal speed v_z. With the trigonometric identity $\sin^2\alpha = (1-\cos 2\alpha)/2$ and the approximation $(1+x)^\alpha = 1+\alpha x$ for $x \ll 1$ when applying the square root we obtain v_z expressed as the average velocity $\bar{v}_z$ in the z-direction plus the oscillatory term:

$$v_z(z) = \bar{v}_z + \frac{K^2 c}{4\gamma^2}\cos(2k_w z) \tag{2.13}$$

$$\bar{v}_z \equiv c\left(1 - \frac{2+K^2}{4\gamma^2}\right) \tag{2.14}$$

Separating the z coordinate into an average and an oscillatory part $z = \bar{z} + z_{\text{osc}}$ where $\bar{z} = \bar{v}_z t$ and using identities for cosine of a sum and solve

$$v_{\text{osc}} = \frac{\mathrm{d}z_{\text{osc}}}{\mathrm{d}t} = \frac{K^2 c}{4\gamma^2}\cos(2k_w(\bar{z} + z_{\text{osc}})) \tag{2.15}$$

to obtain the longitudinal position expressed in terms of the average position. Similarly for x-oscillations, we obtain:

$$\begin{aligned} z_{\text{osc}}(\bar{z}) &= \frac{K^2}{8\gamma^2 k_w}\sin(2k_w\bar{z}) \\ x_{\text{osc}}(\bar{z}) &= -\frac{K}{\gamma k_w}\cos(k_w\bar{z}) \end{aligned} \tag{2.16}$$

The electrons wiggle left and right while traveling through the undulator, but also oscillate a little backwards and forwards. This leads to a figure of 8 shape since the oscillations in the longitudinal direction have twice the frequency of transverse oscillations. By comparing the amplitudes of the oscillations we see that the longitudinal oscillations are a factor of $K/(8\gamma)$ smaller.

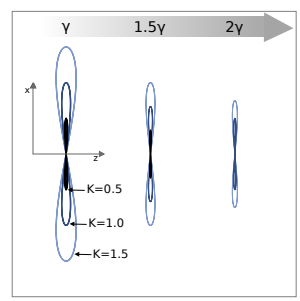

Figure 2.5. *Electron motion described by equations (2.16) in the reference frame of average velocity resembles the number 8. This motion gives rise to higher harmonics for incoherent radiation produced by the undulator. The oscillations in z are enlarged in this image and, in reality, they are a factor of $K/(8\gamma)$ smaller than transverse oscillations.*

2.2.2 Electron motion in an undulator with a laser field

The motion of an electron within an undulator in the transverse direction allows the exchange of energy between the electron and the light field propagating along the undulator. This light field will have an electric (E) field component in the transverse direction, allowing for energy exchange. The light field is produced by a classical laser and introduced into the undulator for the purpose of electron energy modulation. However, some criteria must be fulfilled in order for the average of this energy exchange not to be zero, as the electrons and the laser field are traveling along the undulator. We will now study the basics of this exchange and the requirements that must be met. We model the laser field as a linearly polarized plane wave. We follow only the electric field and neglect the interaction with the magnetic com-

ponent of light[4]. The laser's E-field has only an x-component, and is a traveling wave along z with wave number $k_L = 2\pi/\lambda_L$ and circular frequency $\omega_L = 2\pi\nu$:

$$E_L(z,t) = E_{L0}\cos(k_L z - \omega_L t) \tag{2.17}$$

A change in the electron's energy can be expressed as a product of the current it creates and the electric field

$$\frac{\mathrm{d}W}{\mathrm{d}t} = j E_L = -e\dot{x}E_L = -e v_z x' E_L \approx -ecx' E_L \tag{2.18}$$

By inserting x' and expressing a product of sine and cosine as a sum of two sines we obtain

$$\frac{\mathrm{d}W}{\mathrm{d}t} = -\frac{ecKE_{L0}}{2\gamma}\left[\sin((k_w + k_L)z - \omega_L t) + \sin((k_w - k_L)z + \omega_L t)\right] \tag{2.19}$$

Since we are interested in the energy exchange (between the laser field and an electron) we note that this will happen inside the undulator in the case when the two sine terms do not oscillate over time, so that their integral over time is zero. The argument of the first sine we will call θ_+ and of the second θ_- which can be written collectively as:

$$\theta_\pm \equiv (k_w \pm k_L)z \mp \omega_L t \tag{2.20}$$

We are presently interested in the situation when at least one of the sines is not oscillating in time, which means the theta is constant:

$$\frac{\mathrm{d}\theta_\pm}{\mathrm{d}t} = (k_w + k_L)\bar{v}_z \mp \omega_L = 0 \tag{2.21}$$

With the dispersion relation in vacuum ($\omega_L = c k_L$) this gives two criteria

$$\lambda_L = \pm\lambda_w\left(\frac{2+K^2}{4\gamma^2}\right) \tag{2.22}$$

The second criterion cannot be fulfilled. It is easy to check that if the first criterion is fulfilled then θ_- is oscillating rapidly (with an average of zero), which means that only the first sine term contributes if the parameters are set such that

$$\begin{aligned} \lambda_L &= \lambda_w\left(\frac{2+K^2}{4\gamma^2}\right), \text{or} \\ k_L &= k_w\left(\frac{4\gamma^2}{2+K^2}\right) \end{aligned} \tag{2.23}$$

This is known as the *resonance condition.* This requirement is equivalent to demanding that in time it takes electrons to travel one period

[4]The assumption is made that the laser vector potential is small compared to the wiggler vector potential by a factor of γ^2 since the vector field scales with λ; this is not the same as assuming that the laser B-field is smaller than the undulator B-field, (see [15], page 79).

of wiggle, the light travels the same distance plus one more light wavelength. For the energy change we can write (discarding the ± notation and using only θ instead of θ_+):

$$\frac{dW}{dt} = \frac{d(\gamma mc^2)}{dt} = -\frac{ecKE_{L0}}{2\gamma}\sin\theta \tag{2.24}$$

The sign of the energy change (gain or loss) depends only on θ, which is often referred to as the ponderomotive phase. By introducing another dimensionless parameter analogous to the K-parameter we obtain the change in γ as:

$$\frac{d\gamma}{dt} = -\frac{ck_LKL}{2\gamma}\sin\theta \tag{2.25}$$

$$L \equiv \frac{eE_{L0}}{mc^2k_L} \tag{2.26}$$

The L-parameter is proportional to the laser E-field, in the same way as K-parameter is proportional to the B-field from the undulator. In order to fulfill the criterion in (2.23) several parameters can be varied: the wavelength of the light, the K-parameter of the undulator, and the energy of the electron. The wavelength of the light is fixed since this is the most difficult parameter to change (requires major changes to the laser). Similarly for the energy of the electrons. Luckily, the remaining parameter can be changed. The K-parameter can be changed by opening or closing the undulator (this effectively increases or reduces B_0). So far we have considered one electron with a certain γ, interacting with the field in the undulator. In reality, electrons from the accelerator come in bunches containing hundreds of millions of electrons, and their energy is distributed around an average energy[5] γ. This distribution of energy is called the *energy spread*. We now need to make an important distinction, the average energy of electrons, γ, is not necessarily the same as the resonant energy that fulfills the resonance condition. For a fixed K-parameter and wavelength of the laser light, the electron energy that fulfills the energy exchange criteria will be referred to as the resonant gamma, γ_R:

$$\gamma_R \equiv \sqrt{\frac{k_L(2+K^2)}{4k_w}} \tag{2.27}$$

Since we have established that the energy change depends on the ponderomotive phase, we are interested in how that phase evolves along the undulator. We start with the derivative of the phase:

$$\frac{d\theta}{dz} = (k_w + k_L) - \frac{\omega_L}{\bar{v}_z} \tag{2.28}$$

[5]Although we talk about energy, the constant factor from $\gamma m_e c^2$ is omitted, and we write only γ. Whenever actual energy is needed γ must be multiplied by $m_e c^2$.

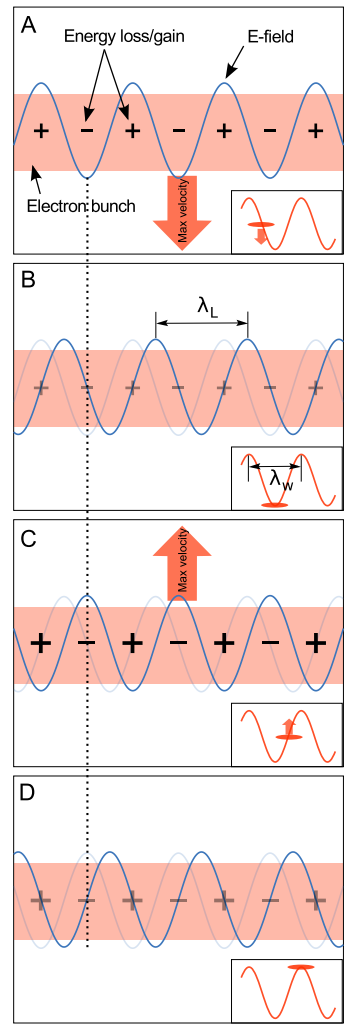

Figure 2.6. *In the time the electron travels one wiggle period the light travels the same distance plus one light wavelength (since it travels faster through the undulator). This leads to the same formula (2.23) as the requirement that the ponderomotive force remains constant in time. (A) Those electrons for which the E-field is pointing in the opposite direction to their velocity will gain energy. The images in the lower right corner show the point of the wiggle period we are looking at in this situation. (B) A quarter of a wiggle period later, the light has advanced ahead of the electrons. At this point, the transverse velocity of the electrons is zero and there is no energy exchange. (C) Similar to (A), but the velocity is pointing the other direction and the same electrons gain energy. (D) Similar to (B).*

and by inserting the dispersion relation, resonant k_L from equation (2.23) and expressing the average velocity $\bar{v}_z$ from (2.14) through the approximation

$$\frac{1}{\bar{v}_z} = \frac{1}{c}\left(1 + \frac{2+K^2}{4\gamma^2}\right) \tag{2.29}$$

we obtain the equation

$$\frac{\mathrm{d}\theta}{\mathrm{d}z} = 2k_w \frac{\Delta\gamma}{\gamma_R} \tag{2.30}$$

where we have introduced $\Delta\gamma$ as $\Delta\gamma \equiv \gamma - \gamma_R$ and assumed that $\gamma/\gamma_R \approx 1$. We can rewrite equation (2.24) for energy change by writing:

$$\frac{\mathrm{d}}{\mathrm{d}z}\left(\frac{\Delta\gamma}{\gamma_R}\right) = \frac{1}{\gamma_R}\frac{\mathrm{d}\gamma}{\mathrm{d}z} = \frac{1}{\gamma_R}\frac{\mathrm{d}\gamma}{\mathrm{d}t}\frac{\mathrm{d}t}{\mathrm{d}z} \tag{2.31}$$

This leads to two coupled equations that describe the change in phase and energy along the z-coordinate:

$$\frac{\mathrm{d}\theta}{\mathrm{d}z} = 2k_w \frac{\Delta\gamma}{\gamma_R} \tag{2.32}$$

$$\frac{\mathrm{d}}{\mathrm{d}z}\frac{\Delta\gamma}{\gamma_R} = -\frac{k_L K L}{2\gamma_R^2}\sin\theta \tag{2.33}$$

This can be similarly rewritten with respect to time, and with the abbreviation $v \equiv \Delta\gamma/\gamma_R$ it becomes:

$$\frac{\mathrm{d}\theta}{\mathrm{d}t} = 2ck_w v \tag{2.34}$$

$$\frac{\mathrm{d}v}{\mathrm{d}t} = -\frac{ck_L K L}{2\gamma_R^2}\sin\theta \tag{2.35}$$

These two equations are similar to Hamilton's equations of a mathematical pendulum [16], due to that resemblance we can write:

$$\frac{\mathrm{d}\theta}{\mathrm{d}t} = \frac{\partial H}{\partial v} = 2ck_w v \tag{2.36}$$

$$\frac{\mathrm{d}v}{\mathrm{d}t} = -\frac{\partial H}{\partial \theta} = -\frac{ck_L K L}{2\gamma_R^2}\sin\theta \tag{2.37}$$

Like Hamilton's equations for mathematical pendulum, these lead to a similar Hamiltonian, which with a constant of integration such that $H(0,0) = 0$, becomes:

$$H(v,\theta) = ck_w v^2 + \frac{ck_L K L}{2\gamma_R^2}(1-\cos\theta) \tag{2.38}$$

We will use this Hamiltonian to see the character of the solutions to the equations obtained. It should be noted that the dimensions of our Hamiltonian are inverse seconds (frequency), and it will thus describe the frequency of rotation of a certain electron within a potential depending on the electron's initial position. One should not think of it as describing the energy of an electron, since this is contained in v.

2.2.3 Phase space and the Hamiltonian

We introduce ξ and Ω and rewrite the Hamiltonian and the Hamilton equations:

$$H(\xi,\theta) = \frac{\xi^2}{2} + \Omega^2(1-\cos\theta) \tag{2.39}$$

$$\xi^2 \equiv 2k_w c\nu^2 \tag{2.40}$$

$$\Omega^2 \equiv \frac{ck_L KL}{2\gamma_R^2} \tag{2.41}$$

$$\frac{\mathrm{d}\xi}{\mathrm{d}t} = -\Omega^2\sin\theta \tag{2.42}$$

$$\frac{\mathrm{d}\theta}{\mathrm{d}t} = \xi \tag{2.43}$$

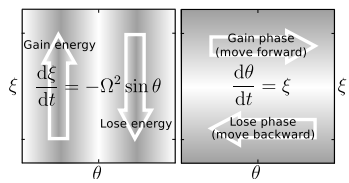

Figure 2.7. *(left) The electron energy change depending on its phase according to Hamilton's equations. Electrons gain energy proportional to $-\sin\theta$. (right) The electron phase (position) change depending on its energy deviation from the resonant energy according to Hamilton's equations. Electrons with excess of energy move forward (positive θ).*

θ, which we have named ponderomotive phase, corresponds to a coordinate ζ along the z-axis; as an angle it wraps (takes same value again) after a period negligibly longer than λ_L

$$\zeta \equiv \frac{\theta}{k_w + k_L} = \frac{\theta}{2\pi}\frac{\lambda_w\lambda_L}{\lambda_w+\lambda_L} \approx \frac{\theta}{2\pi}\lambda_L \tag{2.44}$$

$$z(t) = \bar{v}_z t + \zeta(t) \tag{2.45}$$

Here we have ignored[6] z_{osc}. When an electron has a higher value of θ this means it is moving forward in the electron bunch. The range of θ is from $-\pi$ to π. If it goes forward more than π, the phase wraps and becomes $-\pi$ again. However, the electron then belongs to another segment (the segment ahead). In this way, the whole electron bunch is split into segments, each one optical wavelength long. There are typically thousands of such segments, and in our case we follow only one and assume that the same thing, through periodicity, happens to all the others. The coordinate ξ is only rescaled energy deviation from the resonance condition ν. Apart from the scaling, the coordinate ξ still represents a lack or excess of energy relative to γ_R, so in that respect the coordinate is nothing new, only the scaling has changed. Ω is the angular frequency. From Hamilton's equations we can write the equation for θ, and from this equation it becomes clear that Ω represents the frequency

$$\ddot{\theta} + \Omega^2\sin\theta = 0 \tag{2.46}$$

We recognize this as a pendulum equation, commonly solved for small angles, that leads to free oscillations with frequency Ω. However, we are now interested in all solutions, not just the small-angle solutions. We are interested in curves in phase space (a space containing all possible ξ and θ) where the Hamiltonian is constant $H(\xi,\theta) = H_c$. The Hamilton equations tell us that the electrons rotate clockwise in

[6] This can be justified by looking at the amplitude of z_{osc} at the resonance condition. The amplitude reduces to $\frac{\lambda_L}{(4\pi(1+2/K^2))} \approx \frac{\lambda_L}{8\pi}$.

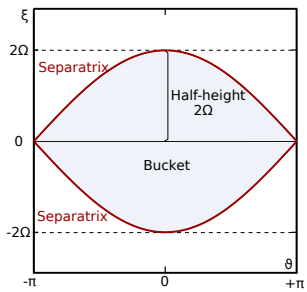

Figure 2.8. *The separatrix forms the borders of the bucket. The height of the bucket is proportional to the square root of the laser's E-field (fourth root of the intensity).*

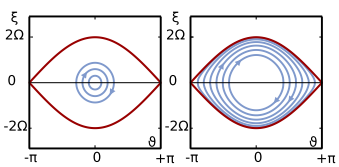

Figure 2.9. *Small-angle solutions behave as a harmonic oscillator with characteristic frequency Ω_0 (left). Large-angle solutions (right) have an oscillation frequency depending on the phase θ_{max} which is always smaller than Ω_0.*

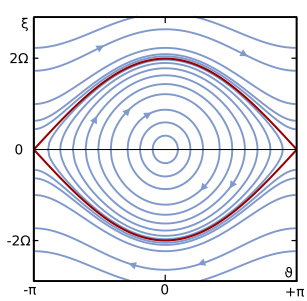

Figure 2.10. *Complete phase space diagram with all solutions. It can be seen that electrons with positive θ (on the right side) lose energy and electrons in the upper half move forwards (positive energy offset).*

phase space. We will divide the regions of interest based on the characteristics of the solutions. A pendulum can oscillate around a stable equilibrium (sway) or rotate if it has enough angular momentum. Similar to classical mechanics, we can find a curve in phase space that separates the two regions of rotation and oscillation from each other. This curve is called the *separatrix*[7] and is given by:

$$\xi_s = \pm 2\Omega \cos\left(\frac{\theta}{2}\right) \tag{2.47}$$

The value of the Hamiltonian on the separatrix is $H_{cs} = 2\Omega^2$. Two points ($\xi = 0$, $\theta = \pm\pi$) and the center of the bucket ($\xi = 0$, $\theta = 0$) are equilibrium points. Only the latter one is stable. Theoretically, electrons with such phase-space coordinates do not move in phase-space. Anything inside the separatrix is called the bucket[8]. We see that from the definition of Ω, the amplitude of the bucket depends on the laser's electric field. We define the bucket half-height as the maximum ξ value on the separatrix

$$\xi_{\max} = 2\Omega = \sqrt{\frac{8ck_w}{2+K^2}KL} \tag{2.48}$$

If we look at small-angle solutions we can approximate $\sin\theta \approx \theta$ and this leads to an equation for a harmonic oscillator with the expected solution $\theta = \sin(\Omega_0 t)$. These solutions are presented in the phase space diagram by circles close to the center of the bucket. The oscillation frequency Ω_0 is known as the synchrotron frequency. Large-angles do not allow such an approximation. The oscillation frequency depends on $\theta_{\max}$. Solving this problem leads to a complete elliptical integral of the first kind[9] κ. The oscillation frequency can be written as

$$\frac{\Omega}{\Omega_0} = \frac{\frac{\pi}{2}}{\kappa\left(\sin\frac{\theta_{\max}}{2}\right)} \tag{2.49}$$

Using an approximation for κ this can be written as (up to about $\theta_{\max} = \frac{3}{4}\pi$):

$$\frac{\Omega}{\Omega_0} \approx \frac{1}{1+\frac{1}{4}\sin^2\left(\frac{\theta_{\max}}{2}\right)} \tag{2.50}$$

from which it is apparent that the frequency falls for larger values of $\theta_{\max}$.

[7] The equation for the separatrix is obtained by calculating the "energy" level in $H(\xi = 0, \theta = \pm\pi)$ and then inserting into the Hamiltonian.

[8] This is in analogy with the RF buckets in storage rings.

[9] The elliptical integral of the first kind can be calculated numerically and tabulated. It is usually denoted K but here we use κ in order not to confuse it with the undulator parameter K. Some properties of κ: $\kappa(0) = \frac{\pi}{2}$; $\kappa(\alpha) = \frac{\pi}{2}(1+\alpha^2/4+9\alpha^4/64+\ldots)$; $\kappa(\alpha \to \frac{\pi}{2}) = \infty$. κ is a constantly growing function as we approach $\alpha = \frac{\pi}{2}$.

Motion outside the bucket is untrapped motion where electrons are traveling to segments ahead (if they are above the bucket) or towards segments behind (if they are below the bucket). This is analogous to the pendulum that has enough angular momentum to just rotate. Once electrons find themselves in a bucket they will not leave it, and electrons outside it will not enter it. This is not entirely true. It is only true within the limits of the theory we have developed so far. It is possible for electrons to enter or leave the bucket if the bucket itself grows or shrinks. So far we have not discussed this option (from the beginning our laser field amplitude E_{L0} was assumed constant). The bucket does grow due to the energy lost by the electrons. This is exactly where the energy of the free-electron lasers comes from. Electrons are made to lose energy and give it to the light bucket. This allows even more electrons to be captured and the laser field is generated. However, the theory of high-gain FELs is much more complicated and is outside the scope of this thesis. To explain the modulation that takes place inside the test-FEL this theory will suffice.

We now have the mechanism to completely describe energy modulation. An electron bunch with bunch length σ_e enters the undulator. We assume a homogeneous density of electrons, "flat top", for a bunch with a length of about a thousand or so periods of λ_L. We use this assumption as the argument for periodicity between buckets. We also assume a light pulse with constant intensity for as long as it lasts. Energy modulation requires a strong light field, and pulsed lasers are used to deliver such strong electric fields. The undulator is set to a K-parameter such that the light from the laser satisfies the resonance condition where γ, the average energy of the electrons, now equals γ_R. Such electrons will lie on a line in phase space with $\xi = 0$ and take all the values of θ. In Figures 2.11 – 2.13 we track 19 such electrons and the projection of their current position. The projection corresponds to their spatial density in the longitudinal direction. Rotation in phase space starts due to their interaction with the light and their energy is modulated. A small modulation in density occurs. After Figure 2.12 our model ceases to be valid. Further along the undulator the two equations that describe the change in the light bucket due to the radiation from electrons must be included. We now either need Maxwell's equations, or we can continue our model without them. In the latter case our model will be valid only for low currents. That is, if the number of electrons is low enough not to significantly change the light field. If we continue beyond modulation and with a low current, we still arrive at similar results to the theory that includes Maxwell's equations. The reader should be aware that this is a distortion of the proper four-equation model. Two important states of electron distribution follow, microbunching in Figure 2.13 (left) and overbunching in Figure 2.13 (right). The electrons start to accumulate at a certain position. Electrons will bunch together inside each bucket and then again periodically after each λ_L, through the whole electron bunch. This is *microbunching*. As we will see later, microbunching

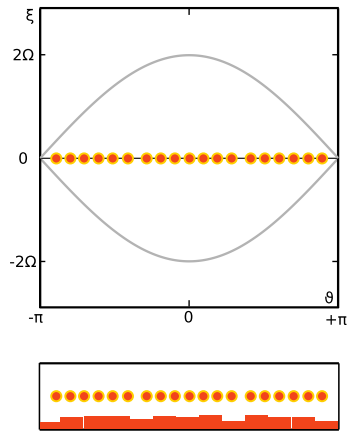

Figure 2.11. *An electron bunch with homogeneous longitudinal density starts interacting with the laser inside the undulator. The lower image shows the longitudinal position of the electrons divided into bins, that is, the longitudinal density, which is homogeneous.*

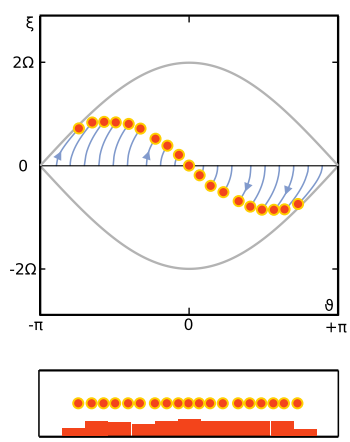

Figure 2.12. *The energy becomes modulated and some electrons have extra energy (relative to the resonance condition), and some have less. The changes in the longitudinal density are very small.*

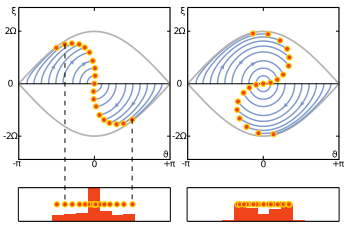

Figure 2.13. *After a distance along the undulator good bunching is produced. Most of the electrons are longitudinally grouped. Emission from them will add coherently with electrons in buckets ahead and behind them (left). If the interaction continues too long the overbunching begins and density modulation falls (right).*

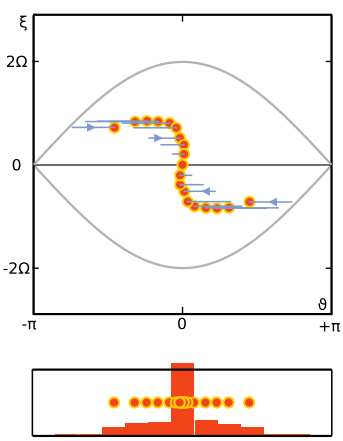

Figure 2.14. *Compression causes electrons with higher energy to end up in front of the center of the bucket and those with lower energy behind. When compression is applied to the situation in Figure 2.12 it can be used to achieve microbunching.*

is the cause of the high intensity and coherence produced by free-electron lasers. The problem at smaller facilities is that it takes many undulator periods for microbunching to develop. For that reason we are interested only in "imprinting" the energy changes and then finding another way to make microbunching develop faster. If our undulator is too short for microbunching to develop we will stop at the situation as shown in Figure 2.12. The energy change along the bunch is somewhat linear around the center (the chirp in the energy is relatively linear) and this linear trend can be used for compression. We therefore leave the interaction with light (exit the undulator) and use compression.

2.3 Compression and bunching

In general, compression means a process in which something is made shorter. Throughout this thesis the compression of several things is discussed, for example, an electron bunch in an accelerator or a laser pulse during chirped pulse amplification (CPA). In this section we are looking for a compression phenomenon that will make electrons with lower energy travel a longer path and electrons with higher energy travel a shorter path. This will lead to a conversion from energy modulation to density modulation along the bunch, similar to microbunching. This compression will be very weak compared to the compression performed in the accelerator to make the whole electron bunch shorter, and will thus not influence the length of the electron bunch. We have seen already that electrons with different energies perform oscillatory motion through an undulator with higher or lower amplitudes, and move with different speeds depending on their energy. We have seen that longitudinal velocity $\bar{v}_z$ depends on the energy (γ) of an electron and the amplitudes of "the figure of 8" motion were also dependent on the energy of the electron. Thus, electrons with different energies taking different paths already happens in an undulator. The easiest and conventional way in accelerator physics to obtain the desired effect is to use chicanes. A chicane is a segment of electron beam pipeline (transport) that has several (usually three or four) dipole magnets, some of which are displaced in order to force electrons with different energies to travel different path lengths. The inset of Figure 2.15 shows such a chicane. The chicane allows us to achieve microbunching from energy modulation, although our undulator is not sufficiently long. A parameter that describes how good a device is in translating energy deviation into different paths is called R_{56}. R_{56} is a parameter connecting the longitudinal displacement Δz to the momentum (energy) offset $\frac{\Delta p}{p}$ in the following way. Its dimension is [length].

$$\Delta z = R_{56}\frac{\Delta p}{p} \tag{2.51}$$

It is easy to recognize what this means in our phase space since, as we have seen, $\Delta z \sim \Delta\theta$ and $\frac{\Delta p}{p} \sim \frac{\Delta E}{E}$ which with certain limitations[10] is the same as $\frac{\Delta\gamma}{\gamma_R} \sim \sqrt{\xi}$. That is to say, R_{56} specifies how much an electron is being pushed forwards in phase space because of its energy deviation. Figure 2.14 illustrates this and how it can lead to microbunching. If we use too large a value of R_{56} this leads to *overbunching* and is counterproductive since it ruins the density modulation. Chicane dipoles are usually electromagnetic, and it is possible to control how much compression the chicane is causing. We now proceed to calculate R_{56} for a chicane consisting of four electromagnets. Figure 2.15 shows only half of such a chicane since it is symmetric (the inset shows the complete chicane).

The distance between the two halves, being independent of energy, can be neglected. The path length through the first half of the chicane (half-path) for energy E is z:

$$\frac{z(E)}{2} = 2l_{\text{arc}}(E) + \frac{d}{\cos\alpha(E)} \tag{2.52}$$

and the total path difference is twice that. ρ (radius of curvature) can be calculated using the following formula:

$$\rho[m] = \frac{\sqrt{\frac{E^2}{c^2} - m^2c^2}}{eB} \approx \frac{10^9}{c}\frac{E[GeV]}{B[T]} \tag{2.53}$$

where B is the magnetic field. We usually know the peak field of the magnets, but this falls on the sides of the magnets. A particle traveling through such a magnet will be influenced by a certain field integral Φ. This integral depends on the current I running through the coils and can be obtained through $\Phi = \phi I$. ϕ [Tm/A] can be measured. The integral is usually measured or simulated numerically. We shift from the integral of the field to the nominal B and effective length l_{eff}, as would be the case if we had a dipole magnet with an ideal magnetic field inside and no field outside (this is called the hard edge approximation). Such an ideal dipole would need to be l_{eff} long to give the same field integral. In principle, we decided to keep the magnetic field but had to adjust the length of the dipole. From Figure 2.15 we have that $\rho\sin\alpha = l_{\text{eff}}$ and $\rho\alpha = l_{\text{arc}}$. The deflection angle α is then:

$$\alpha = \frac{c}{10^9}\frac{\phi\ I}{E[GeV]} \tag{2.54}$$

We rewrite the R_{56} definition as:

$$R_{56} = \frac{dz}{dE}\ E = \frac{dz}{d\alpha}\frac{d\alpha}{dE}\ E \tag{2.55}$$

[10] Technically, E is the average energy of the electrons, while γ_R is set by the undulator and the laser. This comparison holds as long as the electrons' average γ is not far from γ_R, and those are the cases we are interested in here.

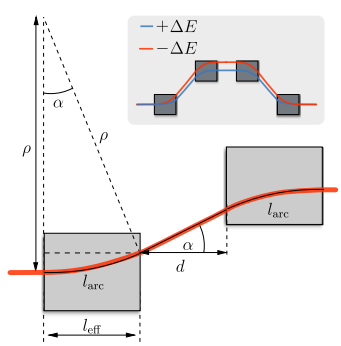

Figure 2.15. *One half of a chicane consisting of four dipole magnets. Parameters used in the calculation are shown. The inset figure shows the complete chicane and the fact that the longer path is taken by electrons with an energy lower than the average.*

Since

$$z = 4\rho\alpha + 2\frac{d}{\cos\alpha} = 4\frac{l_{\text{eff}}}{\sin\alpha}\alpha + 2\frac{d}{\cos\alpha} \tag{2.56}$$

we have for both derivatives

$$\frac{\mathrm{d}z}{\mathrm{d}\alpha} = 4\, l_{\text{eff}}\frac{\sin\alpha - \alpha\cos\alpha}{\sin^2\alpha} + 2\, d\frac{\sin\alpha}{\cos^2\alpha}$$
$$\frac{\mathrm{d}\alpha}{\mathrm{d}E}\, E = -\frac{c}{10^9}\frac{\Phi}{E^2}E = -\alpha$$

Finally, R_{56} becomes:

$$R_{56} = -\alpha\left[4\, l_{\text{eff}}\frac{\sin\alpha - \alpha\cos\alpha}{\sin^2\alpha} + 2\, d\frac{\sin\alpha}{\cos^2\alpha}\right]$$

The vertical displacement D can be easily read out from Figure 2.15 and its numerical values are shown later in Figure 3.4.

$$\begin{aligned} D &= 2\,\rho\,(1-\cos\alpha) + d\,\tan\alpha \\ &= 2\,\frac{l_{\text{eff}}}{\sin\alpha}(1-\cos\alpha) + d\,\tan\alpha \end{aligned}$$

2.4 Radiation

Radiation[11] produced by the relativistic charges in a magnetic field is called *synchrotron radiation.* The radiation is a result of the acceleration of the charged particles. Electrons can be steered in a magnetic field, and this corresponds to a considerable change in velocity (vector quantity) components. No change in speed (scalar quantity) is necessary and thus the energy can remain practically the same. The energy of relativistic electrons is significantly higher than that of the radiation they produce, and we often consider their energy to remain unchanged, although there are small losses that are turned into light. An electron passing through a dipole will produce radiation in a forward tangential direction in a flashlight-like cone with an opening angle inversely proportional to the electron energy. It is possible to significantly improve the spectral and spatial characteristics of the light produced by stacking N_w dipoles, one after the other, while changing the direction of the magnetic field to keep the radiation traveling straight. Such devices are called wigglers or undulators. The total power of radiation [16] produced by an undulator per electron is [12]

$$P_{\text{sp}} = \frac{e^4\gamma^2 B_0^2}{12\pi\epsilon_0 c m^2} = \frac{e^2 c\gamma^2 K^2 k_w^2}{12\pi\epsilon_0} \tag{2.57}$$

[11] By radiation we mean the radiation of light and not ionizing radiation in general.

[12] The same as produced by a bending magnet which has a field that is $\sqrt{2}$ weaker than the peak field of the undulator. This can be understood by remembering that the field of the undulator is $B_0\sin(k_w z)$ so the average square to which the average radiation is proportional is $B_0^2/2$.

As we can see, the power depends quadratically on the K-parameter, and does not depend on the number of periods N_w. This is the total power of the radiation, and one should keep in mind that the undulator will spectrally (and spatially) concentrate the radiation. *This* concentration will yield the increase in useful radiation impinging on a detector, although the total power is independent of N_w. Assuming N_e electrons entering the undulator such that their longitudinal distribution along the bunch is random and relatively homogeneous, they will radiate as they pass through the undulator. The phases of radiation produced by each one of them will be distributed, like their positions. This will give light of intensity that is proportional to N_e (E-field proportional to $\sqrt{N_e}$). If we write the E-field produced by each electron as $\cos\Psi_i$ the intensity will be proportional to the number of electrons:

$$I_{\text{sp}} \sim \left(\sum_{i=1}^{N_e} \cos\Psi_i \right)^2 = \sum_{N_e} \cos^2\Psi_i \sim N_e \tag{2.58}$$

since all the mixed terms after squaring cancel each other out due to the random distribution of phases. This radiation is called *spontaneous radiation*. If the electrons are not homogeneously spaced but come in one bunch that is much shorter than the wavelength of the light produced, or they come microbunched (see Figure 2.16) so that their phases are correlated, the mixed terms will not cancel out, and the radiation produced will be proportional to the square of the number of electrons according to:

$$I_{\text{co}} \sim \left(\sum_{i=1}^{N_e} \cos\Psi_i \right)^2 = \sum_{i=1}^{N_e} \cos^2\Psi_i + \sum_{i,j;i\neq j}^{N_e,N_e} \cos\Psi_i \cos\Psi_j \sim N_e^2 \tag{2.59}$$

as there are $({N_e}^2 - N_e)$ mixed terms. Since N_e can easily be on the order of 10^7 this means seven orders of magnitude more radiation! Not only that, the radiation is coherent and is thus called *coherent radiation*. This is the whole purpose of microbunching (for which we needed modulation and compression).

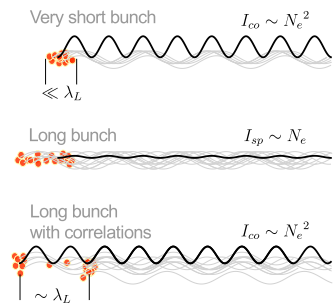

Figure 2.16. *A very short electron bunch would produce coherent radiation. Since no accelerator available today can produce bunches with lengths less than the wavelength of light, one way of regaining the coherence of the radiation is to introduce correlations between positions of the electrons within the electron bunch. The bunch then does not need to be shorter than the wavelength of the coherent light it produces.*

2.4.1 Spontaneous radiation from a planar undulator

The wavelength of the light produced depends, on the electron energy, undulator K-parameter and period of the undulator λ_w. The spectral characteristics will depend on the angle at which the radiation is observed relative to the axis of the undulator. For electrons, in their reference frame, the period of the undulator is relativistically contracted to $\frac{\lambda_w}{\gamma}$. Accounting for the relativistic Doppler effect will add an additional factor of $\frac{1}{2\gamma}$, which leads to the wavelength of the light produced of $\frac{\lambda_w}{2\gamma^2}$. Adding corrections for the reduced traveling speed through the undulator due to wiggling introduces the factor

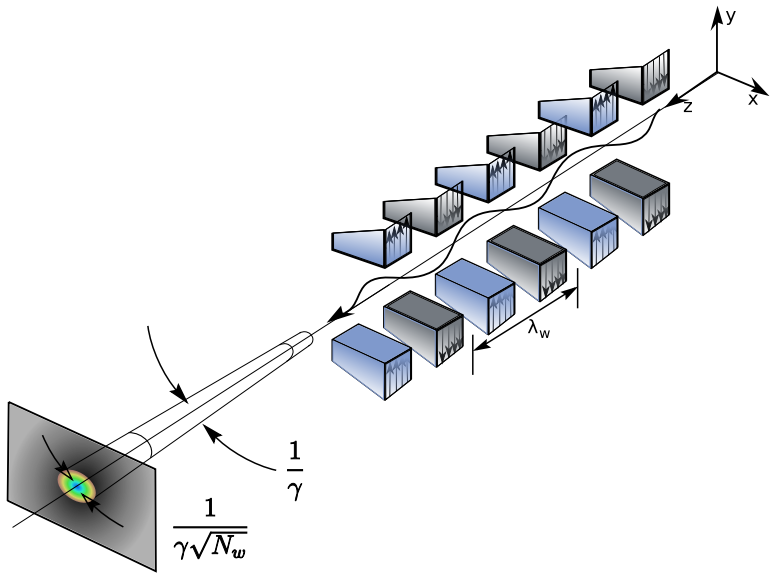

Figure 2.17. *Radiation produced by the undulator spreads with an opening angle inversely proportional to γ, but the central part, with a bandwidth of $\frac{\Delta\lambda}{\lambda} = \frac{1}{N_w}$, narrows with $\sqrt{N_w}$ [17].*

$(1+\frac{K^2}{2})$, and by adding the angular dependence to it we finally obtain

$$\lambda_L = \frac{\lambda_w}{2\gamma^2}\left(1+\frac{K^2}{2}+\gamma^2\theta^2\right) \tag{2.60}$$

This wavelength we call the *fundamental*. The angle θ is an angle between a detector and the axis of the undulator. The fundamental is not the only wavelength produced by a planar undulator. The undulator will also produce higher harmonics (multiples of the frequency) with wavelength $\frac{\lambda_L}{n}$, where n is an integer. When n has the value one, we obtain the fundamental, otherwise we get the second and third harmonics, and so on. Due to the transverse properties of these modes, even modes will not be directly visible on the axis ($\theta = 0 \implies n = 1,3,5,\ldots$). Even modes will be visible if we are observing slightly off-axis, or if the opening angle of the on-axis detector is large enough. The origins of these higher harmonics are longitudinal oscillations in the average reference frame and transverse relativistic effects [17, 18]. The angular dependence of the radiation will be responsible for a slight red shift with increasing angle. This also means that the spectra seen by a detector of finite-size (finite opening angle) will be asymmetric and show red "tails". From Wiedemann [18] and [15] we know that the photon flux from a beam with current I and σ

and π polarization is given by:

$$\frac{d\dot{N}_{\rm ph}(\omega)}{d\Omega} = \frac{e^2}{4\pi\epsilon_0\hbar c}\gamma^2 N_w^2 \frac{d\omega}{\omega}\frac{I}{e}\sum_{n=1}^{\infty} n^2(F_\sigma^2 + F_\pi^2){\rm Sinc}^2 \tag{2.61}$$

$${\rm Sinc} \equiv \frac{\sin\pi N_w \frac{\omega-\omega_n}{\omega_1}}{\pi N_w \frac{\omega-\omega_n}{\omega_1}} \tag{2.62}$$

$$F_\sigma \equiv \frac{2\gamma\theta\Sigma_1\cos\phi - K\Sigma_2}{1+\frac{K^2}{2}+\gamma^2\theta^2} \tag{2.63}$$

$$F_\pi \equiv \frac{2\gamma\theta\Sigma_1\sin\phi}{1+\frac{K^2}{2}+\gamma^2\theta^2} \tag{2.64}$$

where

$$\Sigma_1(n) \equiv \sum_{m=-\infty}^{\infty} J_{-m}(u)J_{n-2m}(v) \tag{2.65}$$

$$\Sigma_2(n) \equiv \sum_{m=-\infty}^{\infty} J_{-m}(u)(J_{n-2m-1}(v)+J_{n-2m+1}(v)) \tag{2.66}$$

$$u \equiv \frac{\omega}{\omega_1}\frac{\bar{\beta}K^2}{4\left(1+\frac{K^2}{2}+\gamma^2\theta^2\right)} \tag{2.67}$$

$$v \equiv \frac{\omega}{\omega_1}\frac{2\bar{\beta}K\gamma\theta\cos\phi}{\left(1+\frac{K^2}{2}+\gamma^2\theta^2\right)} \tag{2.68}$$

$$\bar{\beta} \equiv \beta\left(1-\frac{K^2}{4\gamma^2}\right) \tag{2.69}$$

and θ is an angle relative to the beam axis while ϕ is an azimuthal angle. This looks quite complicated. The important parts of the last equation are the spectral and spatial components. The Sinc function separates harmonics in the frequency domain and reaches a maximum only for one harmonic (all other harmonics have negligible contribution to the Sinc function). It also describes the frequency bandwidth of the spontaneous radiation. The absolute bandwidth of each mode remains the same, but relative to the central frequency of each mode the bandwidth falls as

$$\frac{\Delta\omega_n}{\omega_n} = \frac{1}{nN_w} \tag{2.70}$$

F_σ and F_π describe the amplitudes of modes in the spatial domain for two polarizations. The σ polarization corresponds to a polarization where the E-field lies in the plane in which the electrons are wiggling (in our case, the x-plane) while π is orthogonal plane. Figure 2.20 shows the spatial distributions of a number of photons for the first four harmonics. The spatial distribution is the reason why only odd harmonics are visible on the axis ($\theta = 0$). Increasing N_w concentrates the radiation better spectrally and angularly since it reduces

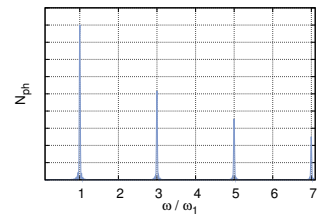

Figure 2.18. *Spectrum from a planar undulator visible on-axis (in a square covering angle $\frac{0.1}{\gamma}\times\frac{0.1}{\gamma}$). The detector can see only odd harmonics. The intensity of the harmonics relative to the fundamental depends on the K-parameter.*

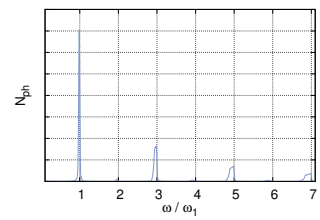

Figure 2.19. *Spectrum of a planar undulator (integrated number of photons) emitted into a square detector that covers an angle $\frac{0.6}{\gamma}\times\frac{0.6}{\gamma}$). Even harmonics become visible but have much lower intensity. Odd harmonics show red-shifted asymmetry.*

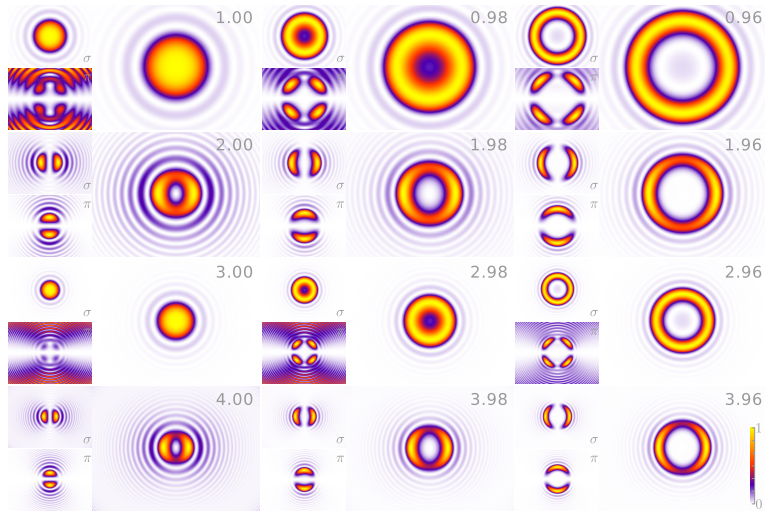

Figure 2.20. *Calculated transverse distribution of radiation for the fundamental, second, third and fourth harmonics in a narrow bandwidth around given frequencies. The frequencies are expressed as a factor of the fundamental frequency. Each image shows the total distribution and on the left separately for each kind of polarization (σ polarization upper images, π polarization lower images). Each image is normalized to the maximum intensity in that image. For example, a pattern given by the π polarization for an image with frequency* 1.00 *is not visible in the total distribution. This means that the relative contribution of this polarization is small. Note the absence of on-axis radiation for even harmonics. The parameters describing the undulator are: $K = 2.5$, $N_w = 10$, and $\lambda_w = 2.5$ cm. The electron $\gamma = 1000$. The x-axis covers an angle of $\frac{3}{2\gamma}$.*

the flashlight-like cone angle in which the radiation is predominantly transmitted. This formula can be somewhat simplified if one is only interested only in the on-axis case.

It is worth pointing out that a K-parameter much smaller than 1 means that the on-axis detector will see radiation from all parts of the sinusoidal path through the undulator, while $K > 1$ means that the flashlight cone does not always illuminate the detector, and the detector receives only radiation from certain parts of electron's path. Fourier transform of such radiation leads to more harmonics (wigglers, $K \gg 1$) compared to an undulator ($K \ll 1$) and the absence of even harmonics on the axis in the undulator case.

2.4.2 Spontaneous radiation from a helical undulator

A helical undulator is an undulator in which the magnetic field rotates along the central axis, while in the planar it was only changing direction in one plane. The rotating magnetic field causes the electrons to travel in a helical path along the undulator and changes the polariza-

tion of the radiation produced. One way to construct an undulator that is able to switch between linear and helical mode is an APPLE-II type undulator. APPLE stands for Advanced Polarizing Photon Light Emitter [19]. This type of undulator consists of four arrays of permanent magnets, see Figure 2.21. In practice, the permanent magnets in one such array of APPLE-II type undulators are not stacked vertically, but are arranged in a so-called Halbach I configuration in order to achieve higher fields, as shown in Figure 2.22. The period of the undulator is four magnet segments long, with orientation $+y$, $+z$, $-y$, $-z$ for the upper arrays and $+y$, $-z$, $-y$, $+z$ for the lower arrays. These arrays can be moved individually in the longitudinal direction. Depending on the displacement, the radiator can produce any required kind of polarization. The undulator will produce pure circular polarization only for certain shifts between arrays, while for all the other shifts this polarization will, in general, be elliptical, see the Appendix.

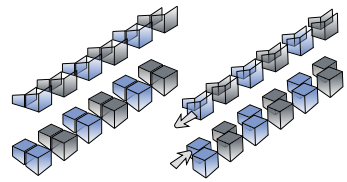

Figure 2.21. *The upper and lower half of a planar undulator are divided into four arrays. Diagonal elements can be shifted back and forth to create a magnetic field that changes direction along the undulator. Anti-parallel movement of two diagonal arrays, as shown here, will give rotated linear polarization. Parallel movement of diagonal arrays gives elliptical polarization, and in special cases circular polarization.*

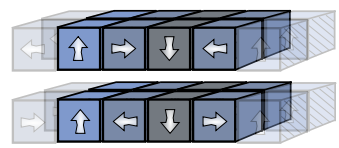

Figure 2.22. *One period of an APPLE-II type undulator has four magnet segments in four arrays. Two diagonal arrays can be translated in the z -direction. This configuration is called Halbach I.*

Shifting two diagonal arrays forward or backward over a certain distance changes the magnetic field in the undulator, causing the electrons to travel in a helical path along the undulator. In case of circular polarization the electrons will travel along a helix around a central axis with a radius of [16]

$$r_{\text{hel}} = \frac{K}{\gamma k_w} \tag{2.71}$$

The longitudinal speed will be constant (unlike the planar undulator)

$$v_z \approx c\left(1 - \frac{1+K^2}{2\gamma^2}\right) \tag{2.72}$$

and thus we *will not have higher harmonics*. This difference in electron motion will also lead to different wavelengths of the fundamental

$$\lambda_L = \frac{\lambda_w}{2\gamma^2}\left(1+K^2\right) \tag{2.73}$$

because the factor originating from the velocity in the z-direction is changed. A magnetic field that twists like a right-handed screw will cause electrons to travel in a way that will give left circular polarization (positive helicity[13]).

The following equation describes the transverse properties of circularly polarized radiation coming from a helical undulator [21] for which it is assumed that $N_w \gg 1$ and θ is small; the number of pho-

[13] Quote from [20], pg. 300.

> (...) the rotation is counterclockwise when the observer is facing into the oncoming wave. This wave is called left circularly polarized in optics. In the terminology of modern physics such a wave is said to have positive helicity.

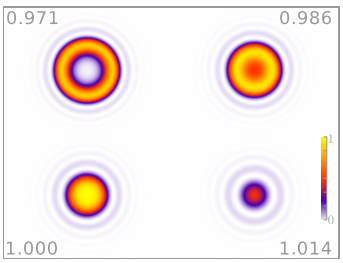

Figure 2.23. *Transverse profile of radiation from a helical undulator for four frequencies close to the fundamental frequency. The values give the fractions of the fundamental frequency. This undulator had the same parameters as the planar undulator in Figure 2.20, but here the x-axis covers an angle of* $3/\gamma$.

tons per second is:

$$\frac{d\dot{N}_{\rm ph}(\omega)}{d\Omega} = \frac{2e^2\gamma^2 N_w^2}{\pi\epsilon_0\hbar c}\frac{d\omega}{\omega}\frac{I}{e}\sum_{n=1}^{\infty}\left(\frac{n\xi}{K}\frac{\sin(\nu_n)}{\nu_n}\right)^2 F_c(n\chi) \tag{2.74}$$

$$F_c(n\chi) \equiv J_{n+1}^2(n\chi)+J_{n-1}^2(n\chi)-\frac{2+2K^2}{K^2}J_n^2(n\chi) \tag{2.75}$$

$$\chi \equiv \frac{2K\gamma\theta}{1+K^2+\gamma^2\theta^2} \tag{2.76}$$

$$\xi \equiv \frac{K^2/2}{1+K^2+\gamma^2\theta^2} \tag{2.77}$$

$$\nu_n \equiv \left(n-\frac{\omega}{2\gamma^2\omega_w}\left(1+K^2+\gamma^2\theta^2\right)\right)N_w\pi \tag{2.78}$$

$$\omega_w \equiv \frac{2\pi c}{\lambda_w} \tag{2.79}$$

The solution is symmetric with respect to the azimuthal angle ϕ and is presented in Figure 2.23. It can be seen that the radiation shows a red shift as we move from the axis, and the fundamental frequency spreads on-axis into a cone. There are no significant higher harmonics.

2.4.3 Coherent radiation

Let us now consider coherent radiation from microbunched electrons. The following applies to helical and planar undulators. We have seen that electrons will microbunch into a structure that periodically repeats itself every wavelength of the fundamental mode. This periodicity allows us to write the electron current as a Fourier series[14]

$$j(t) = \frac{a_0}{2}+\sum_{n=1}^{N}\left[a_n\cos(n\omega_L t+\phi_n)\right] \tag{2.80}$$

The value of N in principle goes to infinity, but we can stop at a relatively low values since we are interested only in the Fourier series approximation of the current. We can also see immediately that a_0 will be $2j_0$ since without the modulation we must return to the original current. This decomposition leads to a factor describing the increase in intensity of the radiation due to coherent emission in the n$^{\rm th}$ harmonic $I_{{\rm co},n}$ relative to the spontaneous intensity $I_{{\rm sp},n}$ [22].

$$I_{{\rm co},n} = \left(a_n\delta_E\delta_\phi\right)^2 N_e\, I_{{\rm sp},n} \tag{2.81}$$

δ_E is a reduction factor due to the energy spread in the electron bunch. Not all electrons entering the modulator undulator will have the same energy, but they will be distributed around an average energy. The less they are distributed the better; the easier it is for modulation and microbunching to become prominent enough and increase

[14] This can be done for time or position along the bunch.

the values of a_n. δ_ϕ is a reduction factor due to the angular spread in the electron beam. As we will see in the next chapter on emittance the electrons have a statistical distribution of angles within the bunch (they are not all traveling in the same direction). These angles will also change the effectiveness of bunching. The dominant contribution here is obviously N_e. Assuming a Gaussian distribution of energy (with σ_E) and angles (with σ_ϕ) it can be shown (page 182, [22]) that the reduction factors are

$$\delta_E = \exp\left[-\frac{1}{2}\left(\frac{2\pi n \alpha \sigma_E L_b}{\lambda_L E}\right)^2\right] \tag{2.82}$$

$$\delta_\phi = \sqrt{\frac{1+B}{2B^2}} \tag{2.83}$$

$$B^2 \equiv 1 + \left(\frac{2\pi n L_b \sigma_\phi}{\lambda_L}\right)^2 \tag{2.84}$$

where L_b is the bunch length and α the momentum compaction of the modulator undulator. Momentum compaction is closely related to R_{56} and appears in this equation because the modulator undulator also performs bunching. The momentum compaction can be written as R_{56}/l_α, where l_α is the length over which compression is applied. If a chicane is added after the undulator, the effective α must be calculated.

One important characteristic of coherent radiation is that it has a significantly narrower bandwidth since it is a result of interference between N_λ sources, unlike spontaneous radiation where we have interference of $\sim N_w$. The linewidth will be given by:

$$\left.\frac{\delta\omega}{\omega_n}\right|_{\text{co}} = \frac{1}{nN_\lambda} = \frac{\lambda_L}{L_b n} \tag{2.85}$$

2.5 Coherent harmonic generation

Without the classical laser pulse in the modulator, and with a sufficiently long undulator, the interaction between the electrons and the spontaneous radiation they produced would start spontaneously. If the undulator is long enough, modulation, bunching and finally radiation will take place. This is known as Self-Amplified Stimulated Emission (SASE) [23–25]. The radiation produced would be spectrally limited only by the bandwidth of the undulator, and would be noisy and spiky within that bandwidth since it originates from noise. Each pulse would have a different spectrum. Since this leads to final radiation with an unstable spectrum, and requires long undulators a *seed laser* is used to replace the function that was performed by noise/spontaneous radiation. This stabilizes the spectrum and allows a shorter undulator to be used. The introduction of a seed laser pulse thus shortens the process and provides coherence, but at the

cost of limiting oneself to frequencies where such seed lasers are available and their harmonics. This setup is called High-Gain Harmonic Generation (HGHG) [26, 27]. Our setup is very similar to the HGHG presented in paper [27]. The reason we do not refer to our setup as having high-gain generation is because our setup does not enter the exponential gain regime, which is a characteristic of high-power free-electron lasers. The advantage of our setup and HGHG compared to SASE is in longitudinal coherence, not power.

2.6 Discussion

Paper **II** presents the results of coherent harmonic generation with the test-FEL setup described in Chapter 3. The highlight of the paper is coherent harmonic generation in the vacuum-ultraviolet region with circular polarization. The polarization of the harmonics produced is characterized by the Stokes vectors briefly described in the Appendix. These harmonics were produced by seeding at a laser wavelength of 263 nm, bunching by the modulator and the chicane, and then extracting the higher harmonic with the radiator-undulator resonant with the higher harmonics. To achieve proper modulation, the modulator undulator must be set correctly. The resonant wavelength of the undulator is set by the gap and the electron energy. Since the energy of the electrons was not known precisely, the correct value of the gap was determined by observing the spontaneous radiation of the modulator. Opening the radiator to the maximum gap effectively removes the influence of the radiator. The gap of the modulator was set so that the spectrum of its spontaneous fundamental mode overlapped with the laser spectrum. This gap can later be tuned more precisely (once lasing has been achieved). The value of the gap was about 15.1 mm. The effects of changing the modulator gap on the intensity of a coherent harmonic are investigated in Paper **II** and shown in Figure 8 of that paper. The intensity of harmonics as a function of the modulator gap (wavelength of the fundamental harmonic) was measured, as well as the intensity of the harmonics versus the compression of the chicane. In order for the test-FEL to function properly, the electron bunch arrival time relative to the laser seed pulse and the bunch compression must be measured. This is solved by the laser technique presented in Paper **III**. Constantly available information about the arrival time allows for feedback. This feedback controls the laser timing to keep it optimal, it stabilizes the operation of the test-FEL and improves the signal-to-noise ratio for higher harmonics. This feedback was still under construction during most of the measurements presented in Paper **II** and the measurements (for example Figure 3 and 4) are done without it. Feedback was added for measurements of linearly polarized higher harmonics (44 nm and 52 nm) and was in use while collecting the data shown in Figure 6. The shortest wavelength produced depends on the modulation, the emittance (see Chapter 4) and

energy spread, and one can express the emittance as a contribution to the energy spread [28, 29].

CHAPTER 3

THE TEST-FEL

This chapter provides a description of the test-FEL, its main components and their role in the system.

The test-FEL was built using upgraded existing infrastructure (the accelerator and transport to the MAX-II ring) and newly purchased equipment (the laser system) in cooperation with the Helmholtz Zentrum Berlin (HZB), which provided the undulators.

The laser system plays two roles. One at the beginning of acceleration when it provides a laser pulse for the photocathode gun, and later when it provides the seed laser pulse in the modulator undulator. These two locations are 60 m apart, and the lasers pulses must be synchronized, for that reason two amplifiers share a common optical master oscillator and deliver pulses with the required characteristics. Since both pulses are actually amplified oscillator pulses they are synchronized. The synchronization is up to a time shift because the pulses travel different paths. This shift must be determined and removed. The amplifier providing the laser pulse for the photocathode gun is called the gun laser. It is located in the gun hutch, together

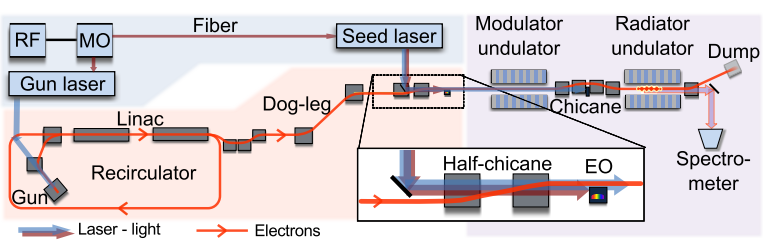

Figure 3.1. *Schematics of a test-FEL setup at MAX-lab. The accelerator, the laser system and undulators for Coherent Harmonic Generation (CHG).*

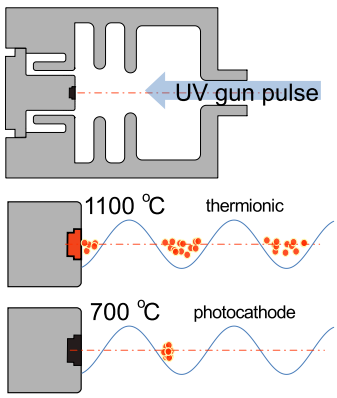

Figure 3.2. *Illustrations of the electron gun with BaO cathode. In thermionic mode, the accelerating RF field inside the gun produces electrons in every cycle. In photocathode mode, electrons are able to leave the cathode surface by the photoelectric effect only if there is a laser pulse present. The bunches produced are thus shorter and have a higher peak current.*

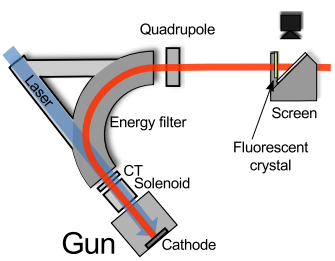

Figure 3.3. *A laser pulse on the cathode at the right RF phase creates electrons that are accelerated and bent with the energy filter dipoles into linac sections. A current transformer (CT) is used to measure the voltage created at the gun, and a solenoid is used for focusing. The quadrupole, screen and the camera used for emittance measurements are shown. Other quadrupoles and correctors are also used but have not been included in this illustration.*

with the oscillator and the RF generator for the accelerator. The other amplifier, providing the seed laser pulse, is located in the MAX-II ring and is named seed laser. It is located in the seed laser hutch. Both hutches are temperature controlled rooms housing laser equipment.

The accelerator is the standard MAX-lab accelerator with an electron gun. For development of the free-electron laser the gun was adjusted to operate as a photocathode gun. After passing through a solenoid, quadrupoles (five in total) and dipole magnets, which function as an energy filter, the electrons are accelerated, compressed and transported to the undulators.

The Undulator section of the test-FEL consists of two undulators and a chicane. The first undulator is used for energy modulation and is thus called the modulator. This undulator is planar. The chicane is used for compression, and the second undulator is called radiator. This radiator is an APPLE-II type undulator and can give radiation of arbitrary polarization.

Several diagnostic instruments are crucial parts of the setup as they ensure or facilitate the operation of the test-FEL. Various current transformers and a Faraday cup measure the current and the charge along the machine. The electro-optical sampling technique is used to monitor the compression of the bunch and the timing of the laser pulse relative to the electron arrival time. Fluorescent screens with YAG crystals are allowing tracking of transverse position of the electron beam and the lasers. Cherenkov fibers are used to monitor beam losses along the vacuum chamber of the test-FEL inside the MAX-II ring. The most important detector at the end of the beamline is the spectrometer in which the produced radiation is observed.

3.1 The accelerator

Acceleration of the electrons starts with a photocathode gun. The metallic oxide cathode of the gun is kept at high temperatures for synchrotron injections. A combination of a high temperature and a high electric field is sufficient to extract electrons from the cathode surface. Electrons are then accelerated by the field. This mode of operation is called thermionic emission. As long as the electric field is present the electrons are extracted and accelerated. This is typically several thousand cycles of the RF field, each cycle being 333 ps since the RF frequency is 3 GHz. In the photocathode regime, the heating of the cathode is lower, and the electric field inside the gun is not sufficient to extract electrons as in the thermionic mode. The gun laser pulse is used to provide the extra energy needed to extract electrons from the surface of the cathode. In this way electrons are extracted only during the short time the laser pulse is present. High peak current, better properties, and more precise energy and timing of the electron beam can be achieved compared with the thermionic mode. The gun is described in greater detail in Paper **I**. A gun laser pulse irradiates the

cathode for 10 ps and an electron bunch about 200 pC is created and accelerated to 1.6 MeV. It passes a focusing solenoid and the energy filter, and then continues into two linear accelerators (linacs). After the first pass through the linacs, the electrons are bent and sent back to pass through the linacs once again. This increases their energy to 375 MeV but also causes losses, and only about 30 to 50 pC will reach the modulator. The gun and both linacs are 3 GHz structures. The 3 GHz RF signal is generated by a signal generator in the gun laser hutch and fed to the klystrons[1] of all three accelerating structures (the gun plus two accelerating sections of the linear accelerator). The relative phase (before delivery to the klystrons) can be shifted mechanically so that each linac structure can have an independent phase relative to the gun. The phase of the gun is locked to the laser and the linac phases. The laser arrival time on the gun is set such that the created bunch has optimal emittance[2], while the phases of the linacs are set to achieve the chirp required for compression. The chicane at the exit of the recirculator and the dog-leg provide the necessary compression parameter R_{56} of -5.5 cm [30, 31]. The phase of the linacs relative to the gun is set to achieve the chirp for compression, and this results in slightly lower energy than normal operation. Instead of changing the dipoles to match the lower energy, the voltage inside the cavities is increased. The voltage inside the cavities is controlled by adjusting the voltages of the klystron modulators[3].

3.2 The laser system

A system-wide clock is generated by a 3 GHz RF clock generator *Rohde & Swartz SMA100A*[4]. This signal is fed to the klystrons and to a box called the Femtolock. The Femtolock locks the repetition of the master optical (MO) oscillator (*Femtolasers Synergy*) to the 32nd harmonic of the RF frequency with a jitter down to 0.2 ps. This is done by controlling the position of the end mirror of the optical resonator and in this way the repetition frequency of the MO. The output of the MO is thus optical pulses with a repetition rate of 93.71 MHz that follows the 3 GHz RF clock. The MO is a mode-locked [32] diode-pumped femtosecond Ti:sapphire laser with a central frequency of 790 nm and a bandwidth of about 13 nm FWHM, equipped with chirped mirrors and giving a power of 700 mW.

The pulses from the MO are stretched inside the gun laser amplifier and split in two parts. One part goes to the seed hutch through a polarization-maintaining optical fiber, while the other is amplified in a regenerative amplifier [33] and a multipass amplifier (both pumped

[1] The klystrons are RF amplifiers which for a short time amplify the RF signal, so that it can be used for the acceleration of electrons in the linacs.

[2] The lowest emittance is of course the best, but one must also consider the charge produced.

[3] Klystron modulators are devices providing power to the klystrons.

[4] The exact frequency is 2 998 775 000 Hz.

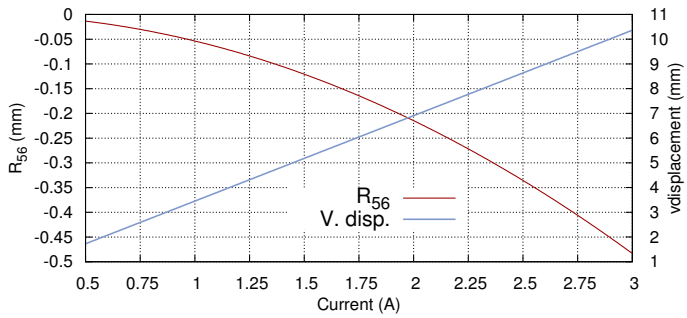

Figure 3.4. *R_{56} of the chicane and vertical displacement as a function of the electric current in the coils of the electromagnets.*

by a 10 Hz Nd:YAG system). After amplification the compressed pulse is sent to the Third Harmonic Generation (THG) unit. This results in UV pulses with a wavelength of 263 nm, 10 ps duration, 10 Hz repetition, and about 500 μJ. The output energy can be controlled by a motorized half-wave plate inside the THG unit and it is usually reduced so that 100 μJ reaches the cathode. The pulse passes a spatial filter and a delay stage which regulates the RF phase at which the laser pulse arrives.

In the seed hutch, the pulse from the fiber is sent through a regenerative amplifier (also pumped by a Nd:YAG 10 Hz pump), compressed and tripled, resulting in 263 nm light, with 5 nm FWHM bandwidth, 300 fs length, 10 Hz repetition, and about 130 μJ. This beam is sent to a UV delay stage and master delay stage. Before the THG a small sample of the infrared beam is extracted to be used for the electro-optical technique. A more detailed description of this system can be found in the chapter about Electro-Optical Spectral Decoding (EOSD). The UV delay stage regulates the timing between this IR pulse and the strong UV pulse. The master delay stage regulates the delay of both pulses relative to the electrons. Both amplifiers are commercial systems bought from *Thales* and operate on the principle of chirped pulse amplification [9].

3.3 The undulator system

The modulator is a planar permanent magnet undulator with 30 periods and a period length of 48 mm. The gap of the undulator can be changed. A smaller gap results in a higher magnetic field and a higher K-parameter, allowing the resonant energy to be set (with a fixed fundamental wavelength of 263 nm). The minimum gap is 13.2 mm and at this value the K-parameter is 3.52. The chicane consists of four electromagnets each 120 mm long, that are separated by 400 mm.

A metal obstacle with a 5 mm high horizontal slit is placed between the second and the third magnets. The slit is displaced upwards by an amount such that only electrons passing through the chicane can pass through the slit. The purpose of the obstacle is to stop the seed laser pulse. The electrons are displaced vertically in the chicane to pass through the slit while the seed laser is stopped by it. This reduces flooding of the spectrometer at the end of the FEL line with radiation from the seed laser. Figure 3.4 shows the R_{56} of this chicane as a function of the current in the magnets, and also the vertical displacement experienced by the electrons.

The radiator is an APPLE-II type undulator with 30 periods, each 56 mm long. The minimum gap is 15.2 mm and with this gap the K-parameter is 4.20 (for horizontal), 3.44 (circular) and 2.98 (vertical polarization). Both undulators are equipped with correction coils. These coils actively correct for errors in field integrals (see Figure 2.4). After the radiator, a dipole magnet bends the electron beam for about 15° into the Faraday cup and the lead/concrete beam dump.

3.4 Diagnostics

As described in Paper **II** the spectrometer used for detection of the harmonics produced receives the light after a reflection from a gold-coated on-axis spherical mirror (45° angle of incidence). The spectrometer contains a grating with 2400 lines/mm. The entrance to the spectrometer has a slit that is wide open, but since it is placed in the horizontal focus[5] of the beam the focus is defining effective "slit" size. The narrow focus of about 200 μm allows the slit to be opened to avoid intensity fluctuations due to the pointing of the beam on the slit[6]. The directional instabilities will appear as slight wavelength shifts on the detector of the spectrometer. The detector is a 1100×330 pixel CCD array that is cooled with liquid nitrogen. The resolution of the spectrometer is about 0.28 nm with 0.038 nm per pixel dispersion.

Transverse overlap of the seed pulse and electrons in the modulator is monitored by fluorescent screens placed before and after the modulator. Screens of this kind are inserted into the beam path and the image is viewed with a camera. Such screens are located at several positions, but the three most important ones are before and after the modulator undulator to monitor transverse overlap, and one placed before the linac, which was used in measurements of the emittance, presented in Paper **I** and Chapter 4.

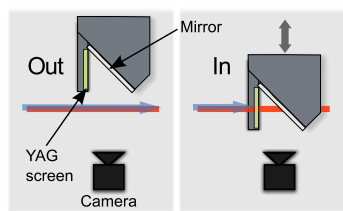

Figure 3.5. *Fluorescent YAG crystals are inserted to view the position and shape of the laser or electron beam.*

[5] After the spherical mirror the beam is astigmatic. Horizontal focusing results in a vertical line and the entrance to the spectrometer is placed where the line is narrowest (the focus).

[6] It was expected that, if the electron beam was not perfectly stable, the light produced would travel in slightly different directions on a shot-to-shot basis. This would lead to intensity fluctuations as the whole pulse could not pass through the closed spectrometer slit.

Four optical fibers run along the vacuum chamber to monitor the location of possible losses. Electrons that are steered the wrong way leave the vacuum chamber, hit the fibers and produce a Cherenkov radiation. The fibers are connected to four photomultipliers. By reading out the time of the signal the longitudinal position of the losses can be determined, while the intensity distribution between the fibers reveals the direction in which the electrons were moving.

The electro-optical setup, which is described in detail in Chapter 5, is the main longitudinal diagnostic.

CHAPTER 4

EMITTANCE

*This chapter gives an introduction to Paper **I** by describing the most important concept in it, the emittance, the way it was measured for the photocathode gun at MAX-lab, and the reason why it is interesting in a broader scope for the test-FEL.*

4.1 Definition

Ideally, the electron beam should have perfectly defined position and momentum. All the electrons having the same energy and traveling in exactly the same direction, packed as closely as possible (transversely). This, of course, is never the case. One reason for this is Coulomb repulsion between the electrons in the bunch, commonly referred to as space charge in accelerator physics jargon. Another reason is of course the initial distribution of the electrons in the source (electron gun). Only Coulomb repulsion or space charge, acts in the beam frame of reference. Space charge effects can be disregarded when discussing emittance at high energies since relativistic transformations "slow down" this interaction in the lab frame. The term *emittance* is used to describe the quality of an electron bunch that is not ideal. Six parameters are required to describe one electron, three for the position and three for the momentum (x, y, z, p_x, p_y, p_z). An electron bunch consists of a very large number of electrons (typically 10^8–10^{11})[1] and statistical moments are used to describe their distribution in six-dimensional phase space, which is usually divided into three parts (assuming no correlations between the three parts): two transverse (x, p_x), (y, p_y) and one longitudinal (z, p_z). It is customary to assume that the momentum in the transverse direction is smaller than in the longitudinal longitudinal direction ($p_x \ll p_z$,$p_y \ll p_z$), and to use the angles the p_x and p_y make with respect to the longitudinal momentum p_z. These angles are commonly marked with prime sym-

[1] 1 pC $\sim 6.241 \cdot 10^7$ electrons, 1 nC $\sim 6.241 \cdot 10^{10}$ electrons.

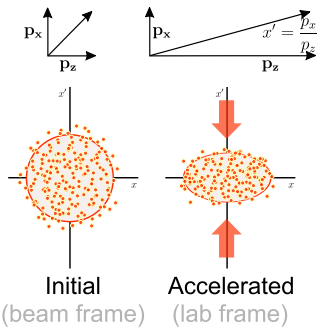

Figure 4.1. *Decrease in emittance due to acceleration. Normalized emittance remains conserved regardless of energy.*

bols as $x' = \frac{dx}{dz} = v_x/v_z$ and due to the approximation of small transverse components $x' = \tan\theta_x \approx \theta_x$. The corresponding notation is used for y'. The space of (x, x') is called trace space in contrast to the phase space which is defined by (x, p_x). The same is valid for (y,y'). The longitudinal direction is usually treated separately.

If S_x is the area of phase space (x, p_x) occupied by an ensemble of electrons, then the *normalized emittance* is

$$\epsilon_n \equiv \frac{S_x}{\pi m_e c} \tag{4.1}$$

In trace space the area $\frac{A_x}{\pi}$ of the trace space (x, x') is called *geometric emittance*,

$$\epsilon = \frac{A_x}{\pi} \tag{4.2}$$

A_x is the smallest area in trace space that contains a certain percentage of the electrons. The geometric emittance decreases with acceleration by a factor of $\beta\gamma$ and its relation to the normalized emittance is

$$\epsilon_n \equiv \beta\gamma\epsilon \tag{4.3}$$

Consider the charge density distribution $\rho(x,x')$ which when integrated over all coordinates gives the total charge of the bunch; the normalized density $f(x,x')$ is defined as:

$$f(x,x') = \frac{\rho(x,x')}{\int \rho(x,x')\,\mathrm{d}x\,\mathrm{d}x'} \tag{4.4}$$

$f(x,x')$ is a probability density function for which the multivariate moment (of two variables in this case) is defined as

$$M_{mn} = \int x^m x'^n f(x,x')\mathrm{d}x\,\mathrm{d}x' \tag{4.5}$$

Describing the large number of electrons in a typical bunch by statistical moments allows us to track their collective properties by following only first few moments of their distribution. Higher statistical moments describe the level of detail that is not of the interest and are thus ignored. This allows us to deal with experimentally common non-homogeneous distributions, and is very practical. The first moments in each variable M_{10} and M_{01} are known as the mean or average and are often denoted as $\langle x\rangle$ and $\langle x'\rangle$. The central moment is generally defined around the mean, and not around zero,

$$\begin{aligned}\mu_{mn} &= \int (x-\langle x\rangle)^m (x'-\langle x'\rangle)^n f(x,x')\mathrm{d}x\,\mathrm{d}x' \\ &= \langle (x-\langle x\rangle)^m (x'-\langle x'\rangle)^n \rangle\end{aligned} \tag{4.6}$$

The moments μ_{20} and μ_{02} are known as variances, and μ_{11} as the covariance. The mean values of these variables are set to zero, making

the general moments, M, the same as the central moments, μ. We do this as we are interested only in the distribution of the electrons and the coordinate system can then be centered around the mean position and momentum. It is possible to include higher moments, but we require only an approximate description of the electron beam and have included only second order moments. A variance-covariance matrix is now constructed which describes the beam:

$$\mathbf{\Sigma} \equiv \begin{bmatrix} \mu_{20} & \mu_{11} \\ \mu_{11} & \mu_{02} \end{bmatrix} \tag{4.7}$$

This matrix changes when the electrons travel through the accelerator. Mathematically this corresponds to the matrix transformation by the transport matrix[2] $\mathbf{M}$ according to

$$\mathbf{\Sigma}_2 = \mathbf{M}^\intercal \, \mathbf{\Sigma}_1 \, \mathbf{M} \tag{4.8}$$

The determinant of the $\mathbf{\Sigma}$ matrix will not change (since $\det \mathbf{M} = 1$). We define

$$\epsilon^2 \equiv \det \mathbf{\Sigma} = \mu_{20}\mu_{02} - \mu_{11}^2 \tag{4.9}$$

Emittance defined in this way will match the geometric emittance for a beam where distributions in x and x' are Gaussians with sigmas σ_x and $\sigma_{x'}$, and the area in trace space encompasses 39.3 % of the electrons [36]. In other words:

$$\epsilon = \sqrt{\det \mathbf{\Sigma}} = \sqrt{\mu_{20}\mu_{02} - \mu_{11}^2} = \frac{A_{x,39.3\%}}{\pi} \tag{4.10}$$

In the case when the covariance vanishes (μ_{11}=0) $\epsilon = \sigma_x \sigma_{x'}$. For general beams (not necessarily Gaussian-like) another common definition is the *rms emittance* [37], defined as:

$$\epsilon_{\mathrm{rms}} \equiv 4\sqrt{\mu_{20}\mu_{02} - \mu_{11}^2} \tag{4.11}$$

For Gaussian-like beams rms emittance covers 86.5 % of the electrons. If there are no nonlinearities in the machine, and the beam has a Gaussian distribution in the trace space, the electrons will form an ellipse (that can be rotated or skewed). This ellipse will be characterized not only by the emittance, but also by the parameters of the machine at the point we are observing the bunch (Twiss parameters or betatron amplitude functions). These parameters describe the optics of the machine, while emittance is related to the electrons. Both, the emittance and the parameters are needed to fully describe the electrons in the machine, but treating them separately provides an elegant

[2] The transport matrix is a matrix that describes a change in a vector with coordinates (x,x') when the beam propagates from position s_1 along the machine to position s_2, so the matrix depends on $\mathbf{M}(s_1, s_2)$. The matrix must also satisfy the condition that it is symplectic (this automatically means that it describes canonical transformation (see [34], pg. 383) and that its determinant is 1. Symplectic matrices form a group with respect to the multiplication operator [35].

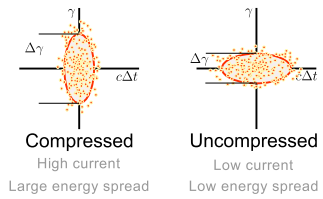

Figure 4.3. *Longitudinal components and the relation between the energy spread and the compression of the bunch.*

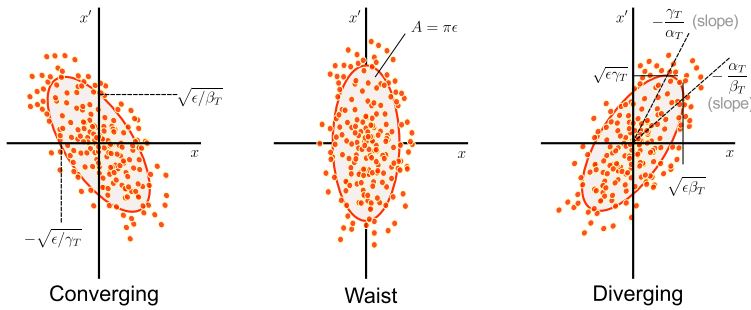

Figure 4.2. *Transverse emittance and Twiss parameters. The size of the ellipse is given only by ϵ. Beam size depends on ϵ and β_T. To completely describe the ellipse, the emittance and two of the three Twiss parameters are needed, since they are not linearly independent. α_T is a parameter proportional to the covariance between x and x' and it equals zero in the waist.*

way of discussing the properties of the bunches of particles independently of the properties related to the machine (e.g. magnets, drift sections, undulators). According to common notation, the Twiss parameters are denoted alpha, beta and gamma, which may cause confusion. Therefore the symbols used here for Twiss parameters have the subscript "T". The relation between the $\mathbf{\Sigma}$, Twiss parameters[3] and emittance is:

$$\alpha_T = -\mu_{11}/\epsilon \tag{4.12}$$

$$\beta_T = \mu_{20}/\epsilon \tag{4.13}$$

$$\gamma_T = \mu_{02}/\epsilon \tag{4.14}$$

From these relations we can see that the Twiss parameters are not independent since $\beta_T\gamma_T - \alpha_T^2 = 1$. A particle with initial coordinates (x_0, x'_0) will follow a trace space path given by:

$$\gamma_T x^2 + 2\alpha_T x x' + \beta_T x'^2 = \frac{A_x(x_0, x'_0)}{\pi} \tag{4.15}$$

This is the equation of an ellipse and it is the primary reason behind the decision to use ellipses in the definition of the emittance. This equation is invariant and independent of longitudinal position along the machine.

Figure 4.2 shows transverse emittance at three positions along the machine. Immediately after passing a focusing quadrupole the ellipse will be converging towards the focus, where there will be a waist in beam size (minimum x span). After the focal point, the beam diverges and would grow indefinitely without additional focusing. This

[3] These parameters are often met in literature as Courant-Snyder parameters, Twiss parameters or just as betatron amplitude functions.

can be used to measure the emittance: either by measuring the size of the beam at several points after the quadrupole magnet or, more commonly, by changing the strength of the quadrupole while measuring the beam size at a fixed position after the quadrupole. The latter method is called a "quad scan" and was used in Paper **I** to characterize the emittance of the photocathode gun used in the operation of the test FEL. One should keep in mind that a quadrupole focusing in one transverse plane is defocusing in the other plane.

4.2 Quadrupole scan

The idea is thus to direct the beam through a quadrupole of variable focusing strength and measure the beam size as a function of the strength at a distance L after the quadrupole. The square of the width of the beam in the focusing plane will behave as a second-order polynomial in relation to the strength of the quadrupole. We wish to calculate the emittance of the beam based on the parameters of that polynomial. Using k to denote the focusing function and l the length of the quadrupole, the focal length of the quadrupole in thin lens approximation is $f = \lim_{l\to 0} \frac{1}{kl}$ (see [38], pg. 48). We write $K = -1/f$ as $-1/f$ appears as an element in a transport matrix for a quadrupole magnet. By applying transfer matrices for a focusing quadrupole and a drift section (empty segment of length L):

$$\mathbf{M} = \mathbf{M_d}\,\mathbf{M_q} = \begin{bmatrix} 1 & L \\ 0 & 1 \end{bmatrix} \begin{bmatrix} 1 & 0 \\ K & 1 \end{bmatrix} = \begin{bmatrix} 1+KL & L \\ K & 1 \end{bmatrix} \tag{4.16}$$

These elements can be used to calculate the transformation of Twiss parameters using the following equation where M_{ij} are matrix elements of the transport matrix in equation (4.16)

$$\begin{bmatrix} \beta_T \\ \alpha_T \\ \gamma_T \end{bmatrix}_{s_2} = \begin{bmatrix} M_{11}^2 & -2M_{11}M_{12} & M_{12}^2 \\ -M_{11}M_{21} & M_{11}M_{22}+M_{12}M_{21} & -M_{12}M_{22} \\ M_{21}^2 & -2M_{21}M_{22} & M_{22}^2 \end{bmatrix} \begin{bmatrix} \beta_T \\ \alpha_T \\ \gamma_T \end{bmatrix}_{s_1} \tag{4.17}$$

We are interested in β_T since, together with emittance, it describes the size of the beam

$$\beta_{TL}(K) = M_{11}^2\beta_{T0} - 2M_{12}M_{11}\alpha_{T0} + M_{12}\frac{1+\alpha_{T0}^2}{\beta_{T0}} \tag{4.18}$$

Inserting M_{ij} and grouping by powers of K gives:

$$\sigma^2 = \epsilon\beta_{TL}(K) = \tag{4.19}$$

$$= K^2(\epsilon L^2\beta_{T0}) + K2L\epsilon(\beta_{T0} - L\alpha_{T0}) + \epsilon(\beta_{T0} - 2L\alpha_{T0} + L^2\frac{1+\alpha_{T0}^2}{\beta_{T0}})$$

Denoting the coefficients in front of descending powers of K as A, B and C, respectively, and reformulating, gives:

$$\epsilon^2 = \frac{4CA - B^2}{4L^4} \tag{4.20}$$

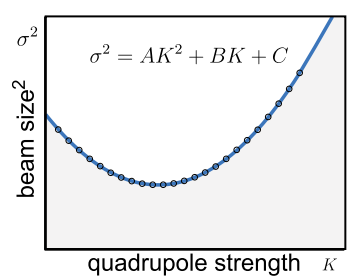

Figure 4.4. *A set of measurements showing that the relationship between the beam width (squared) and the focusing strength is a second order polynomial. The transverse emittance in the plane in which the quadrupole is focusing can then be calculated using equation 4.20.*

4.3 Discussion

As seen in the chapter on coherent harmonics we need as many electrons as possible since the signal improves considerably with increasing number. However, this increases the emittance due to Coulomb interactions within the bunch. The greater the number of electrons, the greater the charge and the greater the repulsion between the electrons. This is most evident when electrons are created before they become relativistic since acceleration “freezes”, or rather slows down their Coulomb interaction in the lab frame. High emittance leads to many detrimental effects on modulation and radiation, and thus, as high a charge as possible is not always the best alternative. For this reason it is important to have good knowledge of the performance of the gun, and this is the subject of Paper **I**. The goal was to determine the emittance of the gun as a function of the charge it produces, and to identify the best working point in terms of phase. The laser pulse is 9 ps long, while the RF cycle is 333 ps. The phase in this case was the timing of the laser relative to the RF cycle calculated in degrees. All the experiments carried out on the test-FEL were performed at the working point presented in this paper, which gives about 200 pC and 5.5 mm mrad normalized emittance. Due to design constraints, these measurements were not performed immediately after the gun, but after a dipole section used as an energy filter after the gun (when operating thermionically for ring injection). This filter scrapes off electrons, which means that the charge leaving the energy filter, and thus the emittance, will be lower immediately after the gun, but still suitable for the operation of the test-FEL.

CHAPTER 5

ELECTRO-OPTICAL SPECTRAL DECODING

This chapter presents the laser technique used for the measurements of the electron bunch arrival time and bunch length. It was used as a non-intrusive on-line diagnostic tool to obtain feedback on the laser timing to improve laser-bunch overlap and stabilize the lasing process.

5.1 History and the idea

A common, and the most direct, way of measuring the bunch arrival time and bunch longitudinal profile is to use a transverse deflecting cavity (TDC). TDC is a cavity that accelerates the beam in the transverse direction. After traveling through the TDC the electrons are monitored on a screen, and the shape and position of the pulse on the screen give information about on the arrival time and longitudinal profile of the bunch. The difficulties associated with this technique are that it requires a separate RF system to feed the cavity, it stops the electron beam, and the time measurements are relative to the RF field.

For seeding purposes, arrival time measurements are needed with respect to the seed laser pulse. This is possible using the electro-optical spectral decoding (EOSD). The first measurements using this technique were performed on laser-generated terahertz signals and later applied to electron bunches at FELIX [39]. Compared to the TDC, EOSD is non-interruptive, significantly cheaper and allows bunch length measurements. A more complicated scheme developed later, electro-optical time decoding (EOTD) also allows the measurement of longitudinal bunch profile [40, 41].

Figure 5.1 illustrates electro-optical spectral decoding. The passage of a relativistic bunch through the crystal creates a high electric field in the crystal. This makes the crystal birefringent[1] for as long

[1] This means that the crystal has optical axes with different refractive indexes and starts mixing polarization. These indexes also depend on the wavelength of light passing through the crystal. For the time being, we neglect the wavelength dependence.

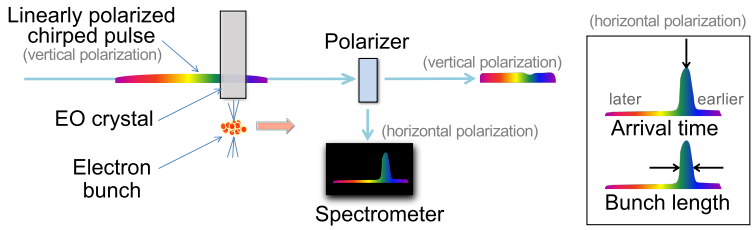

Figure 5.1. *Basics of electro-optical spectral decoding. A linearly polarized, chirped infrared laser pulse passes through a crystal with electro-optic properties and its polarization is changed. Birefringence is induced in the crystal by the electric field of the electron bunch. The electron bunch arrival time and bunch length can be decoded by filtering only the polarization that was initially absent.*

as the electric field is present. If, at the same time, a *chirped linearly polarized* laser pulse (of certain bandwidth and optical length) passes through the crystal, certain parts of the pulse will experience a change in polarization, from linear to elliptical. Afterwards, one filters only the polarization component that was not supposed to be present if there were no electrons, and sends it to a spectrometer. The time of passage of electrons relative to the laser is determined from the wavelength of the strongest signal, and the width of the signal represents the length of the electron bunch. The technique is called EOSD because the information is decoded from the spectrum of a chirped laser pulse. The pulse should be linearly chirped since this establishes the time-frequency relation.

5.2 THz field from relativistic electrons

The electric field generated by the electrons that influences the crystal is significantly enhanced due to relativistic effects. In frequency domain, a typical electron bunch will produce frequencies in the terahertz domain. We are interested in characteristics of this field and its frequencies, because the performance of EOSD depends strongly on them.

The electric field of an electron in its rest frame is spherically symmetric, and in spherical coordinates is given by

$$\mathbf{E}(\mathbf{r}) = -\frac{e}{4\pi\epsilon_0}\frac{\hat{\mathbf{r}}}{r^3} \tag{5.1}$$

where r is the distance from the charge. An electron moving with relativistic energies has an electric field mostly in the transverse direction. Relativistic boosting and transformation to cylindrical coordi-

The simplest half-wave plate or quarter-wave plate is usually made of a permanently birefringent crystal with a well defined length.

nates where the electron moves in the z-direction (and at time $t = 0$ is at $z = 0$), leads to a radial (transverse) and axial (longitudinal) field of the following form (see [20], pg. 559.):

$$E_r(r,t) = -\frac{e}{4\pi\epsilon_0}\frac{\gamma r}{\sqrt{\left(r^2+(\gamma^2-1)c^2t^2\right)^3}} \tag{5.2}$$

$$E_z(r,t) = \frac{e}{4\pi\epsilon_0}\frac{ct\sqrt{\gamma^2-1}}{\sqrt{\left(r^2+(\gamma^2-1)c^2t^2\right)^3}} \tag{5.3}$$

Based on the symmetry of the problem it is obvious that the azimuthal component of the field is zero $E_\varphi(r,t) \equiv 0$. The radial field is a factor of γ larger in amplitude, and shorter by the same factor. This is crucial because the fields become strong enough to induce birefringence. Since EOSD is based on observing the transverse field[2] it can be shown that the frequency components of such a time-dependent radial field are given by[3]

$$E_r(r,\nu_T) = -\frac{e\,|\nu_T|}{\epsilon_0 c^3\sqrt{\gamma^2-1}}K_1\left(\frac{2\pi\,|\nu_T|\,r}{c\sqrt{\gamma^2-1}}\right) \tag{5.4}$$

where K_1 is a modified Bessel function[4]. The index T in ν_T is used only to distinguish between terahertz frequencies and optical frequencies, otherwise there is no difference between ν_T and ν. We use the Fourier transform ($\mathscr{F}$) and inverse Fourier transform ($\mathscr{F}^{-1}$) as given by:

$$f(\nu) \equiv \int_{-\infty}^{\infty} f(t)\, e^{-i2\pi\nu t}\, \mathrm{d}t \tag{5.5}$$

$$f(t) \equiv \int_{-\infty}^{\infty} f(\nu)\, e^{i2\pi\nu t}\, \mathrm{d}\nu \tag{5.6}$$

Let us assume that we have a relativistic electron bunch with a certain longitudinal distribution $n(t)$ of N_e electrons, where $\int n(t)\mathrm{d}t = N_e$, and we used time instead of position along the bunch since $z = \beta ct$. The electric field of the bunch is a superposition of the electric fields of the constituent electrons. This superposition is a convolution of individual fields $E_r(r,t)$. In frequency space it is a product of individual transforms [40]:

$$E_{r,Q}(\nu_T, r) = \mathscr{F}\left[E_r(r,t)\right]\mathscr{F}\left[n(t)\right] = E_r(r,\nu_T)\cdot\mathscr{F}\left[n(t)\right] \tag{5.7}$$

The more energetic and, more importantly, the shorter the bunch, the higher the frequency components of the radial field. Dependence on r is not strong and not important (as a parameter) since the distance between the bunch and the crystal is kept constant during the measurements, typically, a few millimeters.

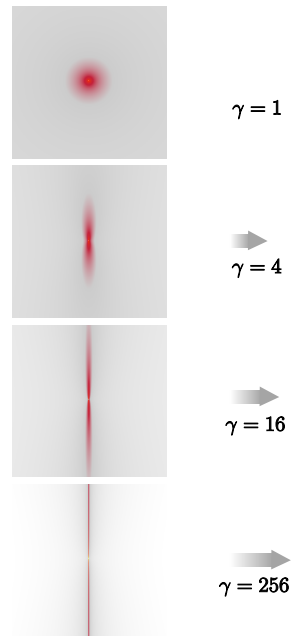

Figure 5.2. *Transformation of an isotropic electric field into a transverse field that is stronger by a factor of γ compared to the static field. Shading (logarithmic scale) is used to make the effect more apparent.*

[2] The longitudinal component of the field is γ^2 times smaller than the static (isotropic) field, and therefore negligible compared to the transverse component.

[3] Similarly to [40, 42].

[4] The modified or hyperbolic Bessel function is given by the expression: $K_\alpha(x) \equiv \frac{\pi}{2\sin(\alpha\pi)}\left(i^\alpha J_{-\alpha}(ix) - i^{-\alpha}J_\alpha(ix)\right)$, where $J_\alpha(x)$ is a Bessel function of the first kind.

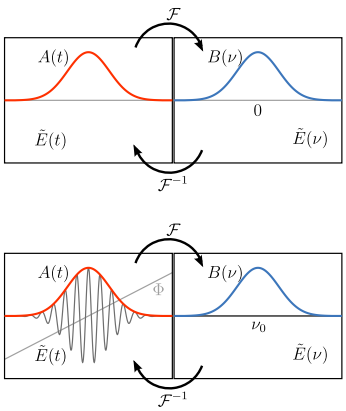

Figure 5.3. *The real-valued Gaussian envelope $A(t)$ without any phases transforms into $B(\nu)$ centered around $\nu = 0$ (upper panel). $\tilde{E}(t)$ with a real-valued Gaussian envelope $A(t)$ and a linearly time-dependent temporal phase Φ transforms into a Gaussian that is centered around $\nu_0 = \frac{\Phi_1}{2\pi}$ (Φ_1 shifts the spectrum to the right) (lower panel).*

5.3 Laser chirp

The EOSD technique requires chirped laser pulses. We are interested in relations between the pulse length and the pulse bandwidth and in a way to describe a chirped pulse. We treat the optical pulse as a complex amplitude, $\tilde{E}(t)$, where all dependence on spatial coordinates is disregarded. The (real-valued) electric field is given by $E(t) = \frac{1}{2}(\tilde{E}(t) + \tilde{E}^*(t)) = \mathrm{Re}\tilde{E}(t)$. The tilde denotes complex valued functions. In the time domain we write $\tilde{E}(t)$ in the polar form. We refer to the modulus as the envelope $A(t)$ and the argument $\Phi(t)$ as the temporal phase:

$$\tilde{E}(t) = A(t)\, e^{i\Phi(t)} \tag{5.8}$$

We can define the pulse to be centered in time without loss of generality (the envelope has a maximum at $t = 0$). For the Fourier transform of $\tilde{E}(t)$:

$$\tilde{E}(\nu) = \int_{-\infty}^{\infty} \tilde{E}(t) e^{-i2\pi\nu t}\, \mathrm{d}t \tag{5.9}$$

we can also write the polar representation

$$\tilde{E}(\nu) = B(\nu)\, e^{i\Psi(\nu)} \tag{5.10}$$

Similarly to the temporal phase, we refer to the complete $\Psi(\nu)$ as the *spectral phase*. In the case of zero temporal phase the spectral phase will also be zero and $B(\nu)$ will be a Fourier transform of $A(t)$, centered around $\nu = 0$. We now expand the non-zero temporal phase in a Taylor series up to the quadratic term and identify the roles of each term. This will reveal some important aspects of chirped pulses.

$$\begin{aligned} \Phi(t) &= \Phi(0) + \left.\frac{\partial \Phi}{\partial t}\right|_0 t + \frac{1}{2}\left.\frac{\partial^2 \Phi}{\partial t^2}\right|_0 t^2 + \ldots \\ &\equiv \Phi_0 + \Phi_1 t + \Phi_2 t^2 + \ldots \end{aligned} \tag{5.11}$$

The first term in the sum, Φ_0, does not depend on time, and is easily transformed as a constant of integration in the frequency domain. This makes it equal to the constant term of $\Psi(\nu)$. For this discussion, this term is not important[5]. All contributions to this term will be neglected since it cannot be measured by EOSD. A linear term in the spectral phase Ψ_1 will correspond to a time shift of the envelope $A(t)$. Defining $A(t)$ to be centered around $t = 0$ means that Ψ_1 is zero. Transformation of a Gaussian pulse with known length and linear temporal phase:

$$\mathscr{F}[e^{-t^2/\tau^2 + i\Phi_1 t}] = \sqrt{\pi}\tau e^{-\tau^2(\Phi_1 - 2\pi\nu)^2/4} \tag{5.12}$$

leads to a Gaussian shifted by $\nu_0 = \frac{\Phi_1}{2\pi}$. It can thus be seen that $\Phi_1 = \omega_0$. It can also be noted that the result has no imaginary components,

[5] This term is known as a carrier-envelope phase (CEP) and plays an important role in modern metrology and laser stabilization.

meaning that non-zero Φ_1 does not change Ψ. It is common to define the *instantaneous frequency* of the pulse as the time derivative of the temporal phase:

$$\omega(t) = \frac{\mathrm{d}\Phi(t)}{\mathrm{d}t} = \Phi_1 + 2\Phi_2 t + \dots \tag{5.13}$$

This shows that the instantaneous frequency changes as a result of higher order terms in the temporal phase, and the pulses in which the instantaneous frequency increases with time are called up-chirped (opposite: down-chirped) pulses. The factor $2\Phi_2$ is called the *chirp rate*. We will show below that this parameter actually has a maximum for a *given* bandwidth of the spectrum. First, by investigating the behavior of Φ_2 we will see that it leads to a stretched pulse in frequency space. Stretching in frequency space means a change in bandwidth.

With the term Φ_2 $\tilde{E}(t)$ becomes $e^{-t^2/\tau^2 + i\omega_0 t + i\Phi_2 t^2}$ and Fourier transformation leads to a stretched frequency-shifted Gaussian which has complex components. These complex components we include in Ψ. The new components in Ψ are proportional[6] to the term $(\nu_0 - \nu)^2$. It is more convenient to write the Taylor expansion of Ψ around ν_0 (instead of around zero) and define the Ψ_n terms as coefficients of $(\nu - \nu_0)^n$

$$\begin{aligned} \Psi(\nu) &= \Psi(\nu_0) + \left.\frac{\partial \Psi}{\partial \nu}\right|_{\nu_0} (\nu - \nu_0) + \frac{1}{2} \left.\frac{\partial^2 \Psi}{\partial \nu^2}\right|_{\nu_0} (\nu - \nu_0)^2 + \dots \\ &\equiv \Psi_0 + \Psi_1(\nu - \nu_0) + \Psi_2(\nu - \nu_0)^2 + \dots \end{aligned} \tag{5.14}$$

We clearly see now that Ψ_1 is the time shift of $\tilde{E}(t)$ in a similar way to Φ_1 being shift of $\tilde{E}(\nu)$. It shifts the signal backwards or forwards in time. The second term is more interesting since it is directly related to Φ_2. So far we have seen that if we introduce Φ_2 into the pulse the result is a broadened spectrum that will have components in the spectral phase such that $\Psi_2 \neq 0$. Transforming a Gaussian envelope with linear and quadratic terms (Φ_1 and Φ_2) leads to a pulse with a wider frequency. Φ_2 thus causes an increase in bandwidth. In real life, the bandwidth is a given quantity. Because we cannot change the bandwidth we now transform in the opposite direction (from the frequency to the time domain). We introduce Ψ_2 into the frequency domain to study its effect in the time domain. We know that it will lead to some value of Φ_2 and that it will stretch a pulse in the time domain. To determine how much it will stretch the pulse in the time domain, we consider our first example (with known time length, and known transform) and add Ψ_2 to the transform. We then transform back the function for which we already know the result without Ψ_2. We transform (compare with equation (5.12))

$$\mathscr{F}^{-1}[\exp\left(-\tau^2(\Phi_1 - 2\pi\nu)^2/4 + i\Psi_2(\nu - \nu_0)\right)] \sim \tag{5.15}$$

[6] Up to a constant (CEP) which we disregard.

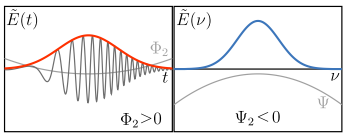

Figure 5.4. *A quadratic spectral phase leads to longer and chirped pulses. The instantaneous frequency of the pulse on the left increases with time (up-chirped pulse). The chirp rate is positive.*

$$\sim \exp\left(-\frac{t^2}{\tau^2+(\frac{\Psi_2}{\pi^2\tau})^2} - it^2\frac{\Psi_2\pi^2}{\pi^4\tau^4+\Psi_2^2} + i\Phi_{CEP}\right)$$

We can see that the pulse (envelope) became stretched (for any non-zero value of Ψ_2) by a factor of $(1+\frac{\Psi_2^2}{\pi^4\tau_0^4})^{1/2}$. The chirp rate will depend on Ψ_2 and have a maximum at $\Psi_2 = \pi^2\tau^2$, and to achieve this the pulse length must be $\sqrt{2}$ longer than the transform-limited length (the shortest length a pulse with given bandwidth can have). The duration of the pulse is usually expressed in terms of its full width at half maximum (FWHM) of the intensity (square of $\tilde{E}(t)$) $W_t \equiv \tau\sqrt{2\ln 2}$, while the bandwidth is expressed as the FWHM of the spectral intensity (square of $\tilde{E}(\nu)$) instead of a σ of distribution[7] of $\tilde{E}(\nu) \sim \exp(\frac{-\nu^2}{2\sigma^2})$, so $W_\nu = 2\sigma\sqrt{\ln 2}$. The pulse is shortest, and has a minimal time-bandwidth product without any chirp; such pulse is called a *transform-limited* pulse. Transform-limited pulses do not have second-order (quadratic) terms, or any other higher order terms, in the temporal or spectral phase. The time-bandwidth product increases with the introduction of a chirp as

$$W_t\, W_\nu = \frac{2\ln 2}{\pi}\sqrt{1+\frac{\Psi_2^2}{\pi^4\tau_0^4}} \tag{5.16}$$

Compression/stretching of pulses relies heavily on the chirp (similar to chicanes in bunch compressors). This is done in a setup that causes higher frequencies to travel a longer path (or experience a higher refractive index), or vice versa (higher frequencies experience shorter paths). A similar process takes place in most transparent optical materials at frequencies around 800 nm and this dispersion, resulting in an up-chirped pulse, is called normal dispersion (the opposite being anomalous dispersion). In the case of propagation through materials the phenomenon of non-zero Ψ_2 is called group velocity dispersion (GVD), Ψ_2 is thus often called the GVD term. A technique commonly used that does not involve passing through dispersive materials is that employing grating compressors. The distance traveled through a grating compressor depends on the wavelength. One way to model such systems is through a response function. We assume a flat frequency response (i.e. no change in amplitude) but the phases will be quadratically shifted. This results in chirping of a transform limited pulse (up or down) and compression, or even further chirping of chirped pulses. Details of this procedure can be found in [43], page 948. Stretching of pulses by adding linear chirp (to reduce the instantaneous power), amplifying them, and compressing them again is the basis of chirped pulse amplification (CPA). This method is used in both laser amplifiers (gun and seed laser), and is the basis of modern high-powered femtosecond lasers.

[7] σ is a square root of the variance.

5.4 Pockels effect

We will now consider the origins of polarization switching in the crystal that is used in EOSD. The process can be modeled in a simple way as a Pockels effect, and is almost identical to the principle intensity modulators (Pockels cells) work (see [44], pg. 521). The refractive index in isotropic materials is independent of orientation. In non-isotropic materials, the refractive index depends on the direction in which the light is traveling through it, and the polarization of the light. The crystal of interest for test-FEL EOSD is isotropic, and thus guides the light independently of direction. However, in the presence of a strong electric field the material becomes birefringent as a consequence of the Pockels effect. The Pockels effect is a non-linear effect, in which the change in refractive index is proportional to the electric field that caused it. This is discussed in detail in [43] and its origins and properties are described in [44]. The PhD dissertations of Steffen [40] and Valk [45] discuss the Pockels effect in zinc-telluride (ZnTe). A ZnTe crystal is used in EOSD at MAX-lab. The performance of EOSD depends highly on the properties and the orientation of the crystal, relative to the probe laser and terahertz field arising from the electrons. The crystal has thickness d and is cut in the (110) plane as shown in Figure 5.5. The terahertz electric field $\mathbf{E_T}$ is at an angle α relative to the $\mathbf{x}$ vector. With a perpendicularly incident terahertz field, the impermeability tensor (a tensor that describes diffractive indexes along the crystal axes) becomes:

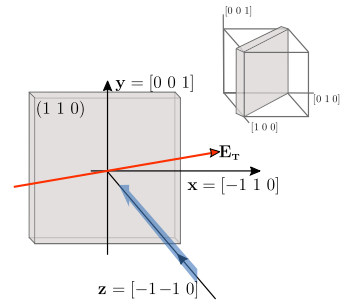

Figure 5.5. *The crystal is cut in the (110) plane. In that plane, the field* $\mathbf{E_T}$ *from electrons makes an angle* α *relative to the vector* $\mathbf{x}$*. The terahertz field and the laser field propagate in the same direction along* $\mathbf{z}$ *into the crystal.*

$$\boldsymbol{\eta}(\mathbf{E_T}) = \frac{1}{n_0^2}\begin{bmatrix}1&0&0\\0&1&0\\0&0&1\end{bmatrix} + r_{41}E_{T,0}\begin{bmatrix}0&\sin\alpha&\frac{1}{\sqrt{2}}\cos\alpha\\ \sin\alpha&0&\frac{-1}{\sqrt{2}}\cos\alpha\\ \frac{1}{\sqrt{2}}\cos\alpha&\frac{-1}{\sqrt{2}}\cos\alpha&0\end{bmatrix} \tag{5.17}$$

In the absence of the field, the refractive index of the crystal is given by n_0. The first part of the right-hand side shows that the crystal is isotropic. Addition of the terahertz field breaks this symmetry proportional to the field with Pockels coefficient $r_{41} \equiv r_{231}$. Which indices are non-zero and dominantly contributing to the Pockels effect depends on the crystal's symmetry and the way it has been cut. For ZnTe cut in the (110) plane it is r_{41}. This coefficient is about $10^{-12}\ \frac{\mathrm{m}}{\mathrm{V}}$. The impermeability tensor can be diagonalized. Eigenvalues λ_i of $\boldsymbol{\eta}$ will give three different indexes $n_i = 1/\sqrt{\lambda_i}$ for axes $\mathbf{U_i}$. The eigenvectors of $\boldsymbol{\eta}$ are the axes $\mathbf{U_1}$ and $\mathbf{U_2}$ (both in the (110) plane) and the third one, $\mathbf{U_3}$, is the same as the propagation direction.

$$\mathbf{U_1} = \frac{1}{2}\sqrt{1+\frac{\sin\alpha}{\sqrt{1+3\cos^2\alpha}}}\begin{bmatrix}-1\\1\\\frac{2\sqrt{2}\cos\alpha}{\sqrt{1+3\cos^2\alpha}+\sin\alpha}\end{bmatrix} \tag{5.18}$$

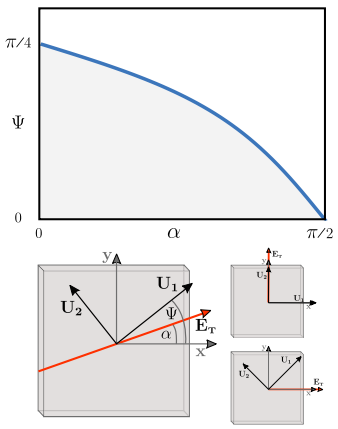

Figure 5.6. *The terahertz field is incident perpendicularly to the crystal (direction of* **z***) but its electric field makes an angle with the x -axis. The orientation of the eigenvectors* $\mathbf{U_1}$ *and* $\mathbf{U_2}$ *depends on the angle* α*. The upper graph shows the decrease in the angle* Ψ *with* α*. The strongest signal is achieved for* $\alpha = 0$*.*

$$\mathbf{U_2} = \frac{1}{2}\sqrt{1+\frac{\sin\alpha}{\sqrt{1+3\cos^2\alpha}}}\begin{bmatrix} 1 \\ -1 \\ \frac{2\sqrt{2}\cos\alpha}{\sqrt{1+3\cos^2\alpha}-\sin\alpha} \end{bmatrix} \tag{5.19}$$

The vectors in the (110) plane depend on the angle α. The refractive indexes along these vectors are:

$$n_s \equiv n_1 = n_0 + \frac{n_0^3 r_{41} E_{T,0}}{4}(\sin\alpha + \sqrt{1+3\cos^2\alpha}) \tag{5.20}$$

$$n_f \equiv n_2 = n_0 + \frac{n_0^3 r_{41} E_{T,0}}{4}(\sin\alpha - \sqrt{1+3\cos^2\alpha}) \tag{5.21}$$

$$n_3 = n_0 + \frac{n_0^3 r_{41} E_{T,0}}{4}\sin\alpha \tag{5.22}$$

The angle Ψ, which $\mathbf{U_1}$ makes with $\mathbf{x}$, depends on α as:

$$\cos 2\Psi = \frac{\sin\alpha}{\sqrt{1+3\cos^2\alpha}} \tag{5.23}$$

The difference in indexes n_1 and n_2, which depends on the terahertz field, is the main cause of polarization rotation of the laser beam passing through the crystal. It is conventional to name the two axes *slow* for higher n and *fast* for lower n, due to the difference in the speed of light. Decomposition of the incident laser field along these two axes gives the phase retardation Γ between them:

$$\Gamma(E_{T,0},\alpha) = \frac{\omega_0 d}{c}(n_1 - n_2) = \frac{\omega_0 d}{2c} n_0^3 r_{41} E_{T,0}\sqrt{1+3\cos^2\alpha} \tag{5.24}$$

The polarization rotation $\Gamma(E_{T,0},\alpha)$, is directly proportional to the thickness of the crystal and the strength of the field (which is proportional to γ and bunch charge). The consequence of a poorly oriented crystal relative to the THz field ($\alpha = \pi/2$) is a halving of the value of Γ. The phase retardation depends on the THz field, and thus maps the terahertz field onto the orthogonal polarization plane. Because of the chirp, newly created polarization has a certain color and we are able to read out $\Gamma(t)$ from the laser pulse.

5.5 The properties of ZnTe

The most important properties of EOSD, its performance and limitations, will be dominantly determined by the crystal and its properties.

5.5.1 Refractive index in the terahertz region

The refractive index in the terahertz region can be calculated from the complex dielectric function $\epsilon(\nu_T)$ of ZnTe. Determined by the lowest transverse optical lattice oscillations ([40],pg. 54), $\epsilon(\nu_T)$ can be written

as a function of the closest resonance plus a constant:

$$\epsilon(\nu_T) = \epsilon_c + \frac{S_1 \nu_1^2}{\nu_1^2 - \nu_T^2 - i\Gamma_1 \nu_T} \tag{5.25}$$

For ZnTe these parameters are $\epsilon_c = 7.4$, $\nu_1 = 5.3$ THz, $S_1 = 2.7$, and $\Gamma_1 = 0.09$ THz. Here ϵ_c is a constant that describes the contributions of all resonances, while other parameters describe the central frequency ν_1, amplitude S_1 and width Γ_1 of the lowest resonance. The complex refractive index is obtained from the complex dielectric function:

$$\sqrt{\epsilon(\nu_T)} = n(\nu_T) + i\kappa(\nu_T) \tag{5.26}$$

The real part represents the refractive index, while the imaginary part describes absorption in the crystal. Absorption peaks sharply at the resonance, and the terahertz waves at these frequencies do not propagate through the crystal. In the region close to the peak of resonant absorption the refractive index shows anomalous dispersion (n falls with ν_T). The phase velocity is given by the refractive index:

$$\upsilon_{\text{tp}} = \frac{c}{n(\nu_T)} \tag{5.27}$$

5.5.2 The Sellmeier equation

For optical frequencies we refer to the Sellmeier equation[8]. The Sellmeier equation is a common form of parametrization for refractive index in the optical domain, depending on the wavelength λ (expressed in μm), and is given here in its reduced form.

$$n(\lambda) = \sqrt{A + \frac{B\lambda^2}{\lambda^2 - C}} \tag{5.28}$$

For ZnTe these parameters are $A = 4.27$, $B = 3.01$, and $C = 0.142$ [46]. It is necessary to know the group velocity of the light to study the mismatch with terahertz waves. Based on the Sellmeier equation it is possible to calculate the optical group velocity as:

$$\begin{aligned} \upsilon_{\text{og}} &= \frac{c}{n}\left(1 + \frac{\lambda}{n}\frac{\mathrm{d}n}{\mathrm{d}\lambda}\right) \\ &= c\,\frac{B\lambda^2(\lambda^2 - 2C) + A(\lambda^2 - C)^2}{(\lambda^2 - C)((A+B)\lambda^2 - AC))\sqrt{A + \frac{B\lambda^2}{\lambda^2 - C}}} \end{aligned} \tag{5.29}$$

For $\lambda = 0.79$, the optical group velocity in ZnTe is $\upsilon_{\text{og}} = 0.300751\ c$.

[8] The Sellmeier equation is in fact the same equation as equation (5.25) but rewritten for wavelength, and sometimes modified so as not to include all resonances. In its full form the Sellmeier equation includes three resonances and the value of $\sqrt{C}$ is the wavelength of a resonance.

5.5.3 Response function and electro-optical response

The frequency-dependent phase velocity of terahertz pulses $v_{\text{tp}}(\nu_T)$ and optical group velocity v_{og} lead to a mismatch in the propagation of these two pulses through the crystal. This can be modeled by a response function:

$$\begin{aligned} M(d,\nu_T) &= \frac{1}{d}\int_0^d \int_{-\infty}^{\infty} e^{i(kz-2\pi\nu_T t)}\delta(z-v_g t)\,\mathrm{d}t\,\mathrm{d}z \\ &= \frac{1}{d}\int_0^d e^{i2\pi\nu_T z\left(\frac{1}{v_{\text{tp}}(\nu_T)}-\frac{1}{v_{\text{og}}}\right)}\,\mathrm{d}z \end{aligned} \tag{5.30}$$

By introducing a frequency-dependent transmission coefficient $A_{\text{trans}}(\nu_T)$ (transition from vacuum into crystal introduces this factor):

$$A_{\text{trans}}(\nu_T) = \frac{2}{1+\sqrt{\epsilon(\nu_T)}} = \frac{2}{1+n(\nu_T)+i\kappa(\nu_T)} \tag{5.31}$$

we can write the total response function:

$$G(d,\nu_T) = A_{\text{trans}}(\nu_T)\cdot M(d,\nu_T)\cdot r_{41}(\nu_T) \tag{5.32}$$

Electro-optical response, that is, the dependence of r_{41} on frequency ν_T, is also determined by the same resonances. This dependence of the electro-optical coefficient on frequencies is very weak for ZnTe, and can be assumed to be constant[9]. Using the response function obtained we can calculate a more realistic value of $\Gamma(t)$:

$$\Gamma(t) = \frac{2\pi}{\lambda_0} d\, n_0^3 \mathscr{F}^{-1}\left[G(d,\nu_T)\cdot E_{r,Q}(\nu_T,r)\right] \tag{5.33}$$

5.6 Detection

When a linearly polarized chirped pulse is sent through the crystal, the pulse experiences a polarization shift given by $\Gamma(t)$. This rotation is on the order of a few degrees, even under ideal conditions, and in general $\Gamma \ll 1$ is considered. To measure the polarization retardation, the pulse is sent through a polarizer and then to the spectrometer. It is necessary to insert a quarter-wave plate (QWP) before the polarizer. Depending on its angle of rotation, the QWP can remove any phase retardation that the crystal gives to the pulse inherently (without any terahertz field being present). After appropriate orientation of the QWP the polarization is linear, and it is possible to continue to the polarizer and spectrometer. The polarization after the polarizer may be incorrectly oriented for the spectrometer, since the spectrometer usually contains a grating with a preferred polarization orientation. In order to rectify this problem, a half-wave plate (HWP), again

[9] See discussion in [40], pg. 57–58 about difficulties in determining parameters and discrepancies between various sources in literature.

appropriately rotated, is inserted between the QWP and the polarizer to rotate the linear polarization. The polarizer is set so as to maximize the spectrometer's grating performance. The HWP rotates the polarization such that the polarizer extinguishes as much as possible of the unwanted polarization, and the QWP makes any residual elliptical polarization linear. A setup in which a linearly polarized pulse is sent through a crystal as described above, and only the perpendicular polarization is measured is called a *crossed polarizer setup*. A setup in which the HWP is very slightly offset, typically about 1°, is called a *near crossed polarizer setup*. The latter has the advantages of higher sensitivity to Γ and constantly providing a small background spectrum of the original pulse. The near crossed polarizer setup is the one used at MAX-lab. The so-called balanced detector setup is even better. This is a setup in which the QWP is rotated so that a circular polarization is created in the absence of the terahertz field. Using a polarizing beamsplitter both polarizations are sent to the spectrometer and can be measured separately (HWP is omitted). In this case, Γ is reconstructed from two signals, as the difference between the signals (intensities) is proportional to $\sin\Gamma$. The crossed polarizer setup gives only proportionality with the sine squared. Unfortunately, balanced detection requires a detector (e.g. a CCD) with very high dynamic range since the signal must be visible over a very strong laser background. This is expensive and unnecessary, as we can achieve our aim with a much cheaper setup.

5.6.1 Jones matrix formalism

Using Jones matrices for optical elements we can describe the intensity measured at the detector to determine the optimal angles of rotation of the waveplates. We assume the terahertz angle to be zero ($\alpha = 0$). A vertically linearly polarized laser field can be written as:

$$\boldsymbol{E_v} = E_l \begin{bmatrix} 0 \\ 1 \end{bmatrix} \tag{5.34}$$

Each optical component can be described by a matrix, for the crystal ($\boldsymbol{C}$), QWP ($\boldsymbol{Q}$), HWP ($\boldsymbol{H}$) and polarizer ($\boldsymbol{P}$). Since the basis vectors for these matrices are the horizontal vector $\boldsymbol{x}$ and the vertical vector $\boldsymbol{y}$ (Figure 5.6), and not the main axes ($\boldsymbol{U_1}$ and $\boldsymbol{U_2}$) the matrix describing the crystal must be rotated by the angle Ψ, which is $\frac{\pi}{4}$ in the case when $\alpha = 0$, using equation 5.23. Since the QWP can be rotated arbitrarily by φ_Q and the HWP by φ_H their matrices must also be rotated. This is done using the rotation matrix:

$$\boldsymbol{R}(\varphi) = \begin{bmatrix} \cos\varphi & -\sin\varphi \\ \sin\varphi & \cos\varphi \end{bmatrix} \tag{5.35}$$

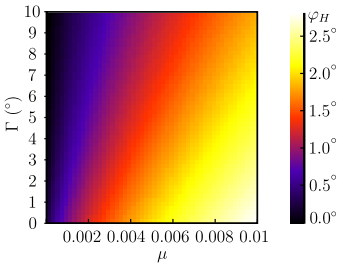

Figure 5.7. *Optimal angle of rotation φ_H of HWP as a function of the level of signal Γ and background due to imperfections relative to the maximum laser intensity μ.*

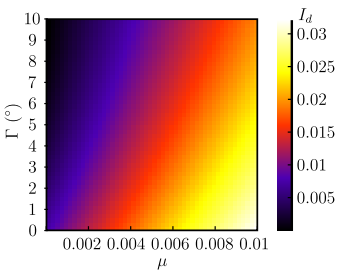

Figure 5.8. *Intensity $I_d(\varphi_H,\varphi_Q,\Gamma)$ at the optimal value of the angle φ_H given in Figure 5.7 for various values of Γ and μ. I_d is normalized.*

The electric field polarization entering the spectrometer can then be written:

$$\begin{aligned}&\boldsymbol{E_d}(\varphi_H,\varphi_Q,\Gamma)=\\&=\boldsymbol{P}\,\boldsymbol{R}(\varphi_H)\boldsymbol{H}\boldsymbol{R}(-\varphi_H)\,\boldsymbol{R}(\varphi_Q)\boldsymbol{Q}\boldsymbol{R}(-\varphi_Q)\,\boldsymbol{R}(\Psi)\boldsymbol{C}\,\boldsymbol{R}(-\Psi)\boldsymbol{E_v}\end{aligned} \tag{5.36}$$

where the matrices are given by:

$$\boldsymbol{Q}=e^{i\frac{\pi}{4}}\begin{bmatrix}1&0\\0&-i\end{bmatrix} \tag{5.37}$$

$$\boldsymbol{H}=\boldsymbol{Q}^2=e^{i\frac{\pi}{2}}\begin{bmatrix}1&0\\0&-1\end{bmatrix} \tag{5.38}$$

$$\boldsymbol{C}=\begin{bmatrix}e^{-i\frac{\Gamma}{2}}&0\\0&e^{i\frac{\Gamma}{2}}\end{bmatrix} \tag{5.39}$$

$$\boldsymbol{P}=\begin{bmatrix}1&0\\0&0\end{bmatrix} \tag{5.40}$$

Due to the polarizer, the vertical (second) component of the final field is zero. The field is then determined by the horizontal component:

$$\begin{aligned}&E_d(\varphi_H,\varphi_Q,\Gamma)=\\&E_l\frac{1+i}{\sqrt{2}}\left[i\cos(2\varphi_H-\varphi_Q-\frac{\Gamma}{2})\sin(\varphi_Q)+\cos(\varphi_Q)\sin(2\varphi_H-\varphi_Q+\frac{\Gamma}{2})\right]\end{aligned} \tag{5.41}$$

and the intensity by

$$\begin{aligned}&I_d(\varphi_H,\varphi_Q,\Gamma)=\frac{c\epsilon_0}{2}E_d\,E_d{}^*=\frac{c\epsilon_0E_l^2}{2}\left[\mu+\right.\\&\left.+\sin^2(2\varphi_H-\varphi_Q-\frac{\Gamma}{2})\cos^2(\varphi_Q)+\sin^2(\varphi_Q)\cos^2(2\varphi_H-\varphi_Q+\frac{\Gamma}{2})\right]\end{aligned} \tag{5.42}$$

Due to various imperfections[10] the intensity has an additional term proportional to the laser intensity with a factor of proportionality μ. We are interested in angles φ_Q and φ_H that optimize the modulation depth γ, defined as in [47]

$$\gamma\equiv\frac{I_d(\varphi_H,\varphi_Q,\Gamma)-I_d(\varphi_H,\varphi_Q,0)}{I_d(\varphi_H,\varphi_Q,\Gamma)+I_d(\varphi_H,\varphi_Q,0)} \tag{5.43}$$

but very close to the angles where $I_d=0$, otherwise the detector will be saturated by the laser background. The optimal values of φ_Q and φ_H depend on Γ and μ. Figure 5.7 shows the optimal rotation of HWP for various values of Γ and μ. The optimal value for φ_Q is zero, and it should be used only to remove possible ellipticity from the signal (that is to minimize μ).

[10]The imperfections in the crystal structure can cause the scattering of the chirped pulse and increase the background in EOSD. These imperfections are very common in ZnTe. Various accumulated polarization shifts and residual birefringence in all the components of the setup after the crystal, can also contribute to the background.

5.7 The limitations of the EOSD

The limitations of EOSD in reconstructing the bunch profile (and bunch width) can be divided into limitations related to the crystal, to the laser (laser bandwidth and laser chirp) and to the measuring technique itself. The limitations are distorting the function Γ and the measurement of the bunch width.

The crystal must respond to all the frequency components of the terahertz pulse and ideally does not absorb some of them more than the others. This response to the frequencies is modeled by the response function of the crystal. The crystal response function will be highly dependent on the resonances in the crystal. In equation 5.33 the response is included through the dielectric function. Resonances in the crystal on low frequencies will introduce distortions and absorption of the terahertz field. These material dependent limitations cannot be avoided by other means than finding a better material. To obtain a better signal, materials with a high electro-optical coefficients are required. Materials without resonances at low frequencies and that have a high electro-optical coefficient are required for improvements in resolution of the bunch length measurements[11]. The frequency dependent dielectric function $\epsilon(\nu_T)$ leads to different phase velocity υ_{tp} and group velocity υ_{tg} for terahertz pulses, and effectively chirps the terahertz pulse. In the optical domain, the difference between optical group velocity υ_{og} and terahertz phase velocity υ_{tp} will introduce frequency-dependent and crystal-thickness-dependent corrections $G(\nu_T, d)$. Not all frequencies are equally good at generating the change in refractive index, and thus r_{41} depends on the frequencies $E_T(\nu_T)$ of the terahertz pulse. This is modeled as $r_{41}(\nu_T)$, although for ZnTe the dependence is negligible. More detailed and consistent treatment of the phenomena present in EOSD requires considerations of the sum and difference frequency generation (SFG, DFG). This will present a limitation that is characteristic of EOSD. The frequencies of the terahertz pulse are mixed with the frequencies of the optical pulse, which results in a spectrally broader pulse [50], see Figure 5.11. Using EOSD, the spectrally broadened pulse will be wrongly interpreted as a longer electron bunch. This phenomenon places limitations on EOSD since it reduces the resolution given by the wavelength-to-time mapping given by the linear chirp. Generation of sum and difference frequencies (between optical frequencies and terahertz frequencies) leads to additional smearing of the signal over the chirped optical pulse.

Although EOSD is inferior to EOTD when it comes to measuring the bunch length, EOSD does not require a separate reference pulse and the generation of a second harmonic. This makes it simpler and

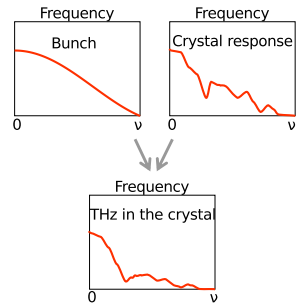

Figure 5.9. *The terahertz pulse propagating through the crystal is determined by the frequency components of the bunch and the response function of the crystal. All the negative effects lower the amplitude of the response function and reduce the amplitudes on higher frequencies.*

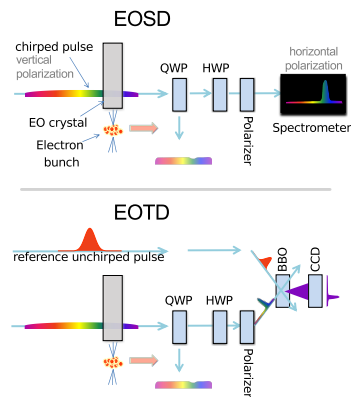

Figure 5.10. *Comparison of EOSD and EOTD. EOTD requires a reference pulse that is afterwards used for second harmonic generation in a nonlinear crystal. Most commonly the material used for this purpose is beta barium borate (BBO). EOTD measures the intensity of the created polarization instead of the spectrum. The reference pulse is much shorter than the chirped pulse and on the BBO it swipes over the chirped pulse in position. The position of the created second harmonic is read to reconstruct the intensity.*

[11] Some organic materials such as DAST (4-dimethylamino-N-methyl-4-stilbazolium-tosylate) have no resonances over a very broad range, however, the response at zero and low frequencies is very poor, and thus this material could only be used as a complement to one of the standard EO materials [48, 49].

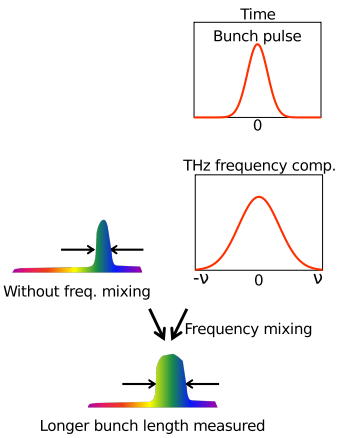

Figure 5.11. *The frequency mixing of the terahertz components and the optical components results in a broader signal on the spectrometer. This effect is more important for shorter bunches. It presents the largest limitation for EOSD bunch profile measurements.*

more reliable. EOSD is thus a very good choice among electro-optical techniques for measurement of the arrival time. Spectral upconversion is another technique that uses SFG and DFG mixing of frequencies to measure the bunch length [51]. It is very simple, and uses picosecond lasers instead of femtosecond lasers, but it can only measure the length of short bunches, and gives no information on arrival time. It decodes the bunch length from the spectrum arising only from electrons, since the picosecond laser has a narrow bandwidth.

5.8 EOSD at MAX-lab

Figure 5.12 shows schematically the way in which the infrared and the seed laser pulse are prepared. An infrared oscillator pulse guided by the optical-polarization-maintaining fiber arrives at the seed laser hutch. This pulse has the same repetition rate as the oscillator, one pulse every 10.67 ns, and is already stretched (chirped) by the stretcher in the gun laser hutch. It enters a regenerative amplifier (Regen) that is pumped with a Nd:YAG Q-switched pump laser (not shown in the figure). Inside the regenerative amplifier, only one oscillator pulse is chosen for amplification. The period of the regenerative amplifier is about 6 ns. By selecting when to open the Regen, to release the pulse, one can shift the pulses by 6 ns. The infrared pulse then continues into a grating compressor where it is compressed (the compressor has a bandwidth of about 5.5 nm). After the compressor the pulse continues to third harmonic generation (THG) where its frequency is tripled from 790 nm to 263 nm. The newly created UV light pulse is about 500 fs FWHM long and contains 100 μJ of energy per pulse. The UV pulse continues to a telescope[12]. The telescope places the focal spot of the UV beam so as to be in the middle of the modulator. After focusing optics (F#), the seed pulse continues to a translatable delay stage (UV DS). This delay stage is set so that the UV pulse can be timed synchronously with the IR pulse for EOSD. A small part of the compressed IR pulse after the compressor (< 1 μJ) is sampled for EOSD. This infrared pulse is also sent through focusing optics (the focal spot is on the EO crystal) and then transversely recombined with the seed UV light pulse in a master delay stage (DS). This motorized delay stage has a range of 150 mm (corresponding to ~ 1 ns) and the stage itself can be manually moved on a 1 m long rail on which it is mounted. After the master delay stage, both pulses can be sent to a system designed to check for temporal overlap of the IR and UV pulses (CHK). This check is based on the difference frequency generation (DFG) within a nonlinear crystal. One can say that the pulses are synchronous if the signal corresponding to the difference in energy between the IR and UV pulses (400 nm) is observed. After the master

[12] In optics, a series of lenses in which the beam is expanded and focused to a desired desired focal length is called a telescope.

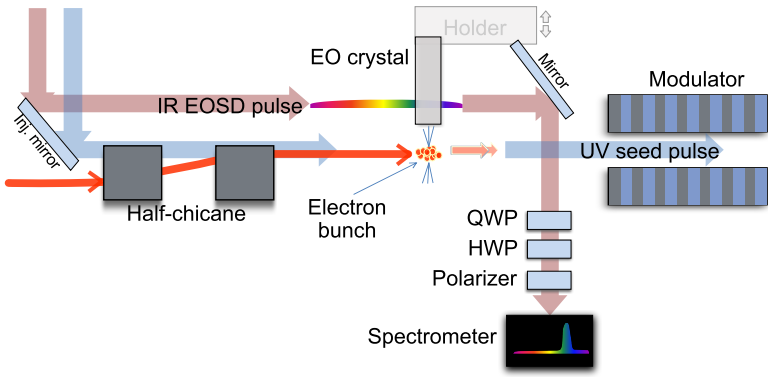

Figure 5.13. *The EOSD setup used in the test-FEL at MAX-lab. EOSD system is positioned after the seed laser injection mirror and the half chicane. The chirped IR pulse travels along the same path as the UV seed pulse to minimize the offset between them. In the case of slight misalignment the IR pulse is sent through the ZnTe crystal, while the UV pulse is transversely overlapped with the path of electrons for the purpose of seeding.*

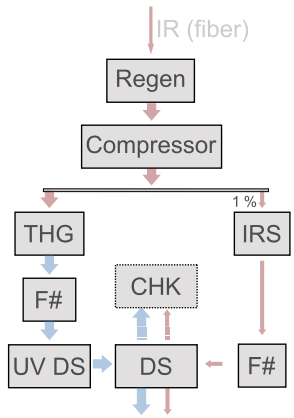

Figure 5.12. *Schematic of the seed laser amplifier and optics for IR and UV pulses. After the master delay stage (DS) the UV pulse is about* 500 *fs long with energy of up to* 100 *μJ. The IR pulse is chirped to about* 3.3 *ps with an energy of about* 1 *μJ. The UV DS regulates the delay between the UV pulse and the IR pulse, while the DS regulates delay of both pulses relative to the electron bunch. A detailed description is given in the text.*

delay stage, the pulses continue to two motorized mirrors towards the injection mirror (this is the point of entry in Figure 5.13).

Figure 5.13 shows a schematic of the EOSD and injection of the seed pulse. The laser beams are led towards the EO crystal and modulator by an injection mirror. Before this mirror the beams enter the vacuum system through a UV-transparent window. The half chicane raises the electron beam and the electron beam is aligned so that it passes through the undulator system. The UV beam is set transversely to overlap with electrons using the two motorized mirrors before the injection mirror (not in the vacuum system). The EO crystal is mounted on a translatable stage which allows the proximity to the electron beam path to be controlled. Behind the crystal a mirror is positioned at an angle 45° to send the IR beam for analysis (out of the vacuum system through another window). There is a reverse-biased photodiode on the EO holder, which is connected to a 1 GHz oscilloscope. The photodiode is used to time the arrival of electrons relative to the UV beam with a precision of about 200 ps. It is visible in Figure 5.14, which shows the holder together with two crystals and a mirror behind them. The QWP is usually set without the HWP in place, so that the background reaching the detector is minimized (this can be achieved with very good extinction). Then the HWP is inserted so that the background is again minimal. The HWP is then rotated about 1.5 to 2 degrees. The direction of rotation of the HWP is important. In one direction the terahertz signal is added to the background (as shown in the figures above), but if the HWP is rotated in the other direction the terahertz signal is mostly visible as a dip in the laser background.

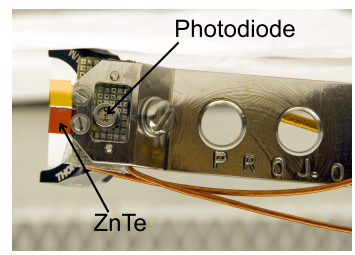

Figure 5.14. *The holder for EO crystals. The photodiode used for rough timing measurements is visible with part of its electronics (behind the holder). The lower crystal is ZnTe (*1 *mm thick) and the upper crystal is GaP (*300 *μm thick). The mirror used to deflect the IR pulse out of the EO chamber is visible behind the crystals.*

The setup after the chamber with the crystal holder consists of two silver mirrors (to realign the IR laser beam leaving the crystal), the HWP, QWP, Glan-laser polarizer, a lens (that focuses the beam onto a slit), a slit whose opening can be controlled by a micrometer screw, another silver mirror (inserted due to size constraints to prolong the path from the slit to the grating), an Al-coated reflective holographic grating (with 1200 lines/mm), a focusing lens and a Firewire camera. The camera is a Pointgrey Firefly camera with no optics mounted on it. It has a CMOS detector with 10-bit dynamic range and a horizontal resolution of a 720 pixels. Each pixel is 6 μm in size. The spectrum is read from the camera as an image. The horizontal axis represents the wavelength, while the vertical axis gives the size of the beam on the detector. It proved useful to use the image mode as low signal levels were much more easier to discern than when observing the spectrum as a projection onto wavelength axis. The camera is rather close to the beamline, and the (ionizing) radiation causes some damage, which deteriorates the quality of the image mostly by increasing the number of "dead" pixels. One or two cameras are replaced per year to have high quality images (for publication). For purposes not requiring high image quality, damaged cameras can be used for longer period that is several years.

5.9 Analysis

The image produced by the detector is transferred to a computer. Processing of images takes place afterwards, using MATLAB routines for the determination of jitter and bunch length. For on-line measurements of arrival time (in order to obtain feedback) real-time processing is carried out using LabVIEW.

For noise reduction the images without an IR pulse (dark images) are used to determine the number and position of "dead" pixels. We selected the strongest 1% of the pixels in the dark image[13] and defined them as dead pixels. The real number of dead (non-functioning) pixels changes depending on the radiation damage, typically around 1% of the total number of pixels. The coordinates of the dead pixels are then stored by the software. A new image, with the IR pulse, but without the terahertz signal, is then obtained to determine the background spectrum; the "dead" pixel values being replaced by the median values of their neighbors. This image is used for subtraction. During measurements, images are acquired, with both the IR laser pulse and the electrons, the "dead" pixels are replaced by median values of their neighbors, and the background image is subtracted. This gives the resulting image which, when summed in the vertical direction represents the final signal.

In order to transform values of wavelength into time, the EO signal is observed while moving the delay stage (shifting the laser). Since the

[13] "Dead" pixels have maximum intensity on this camera.

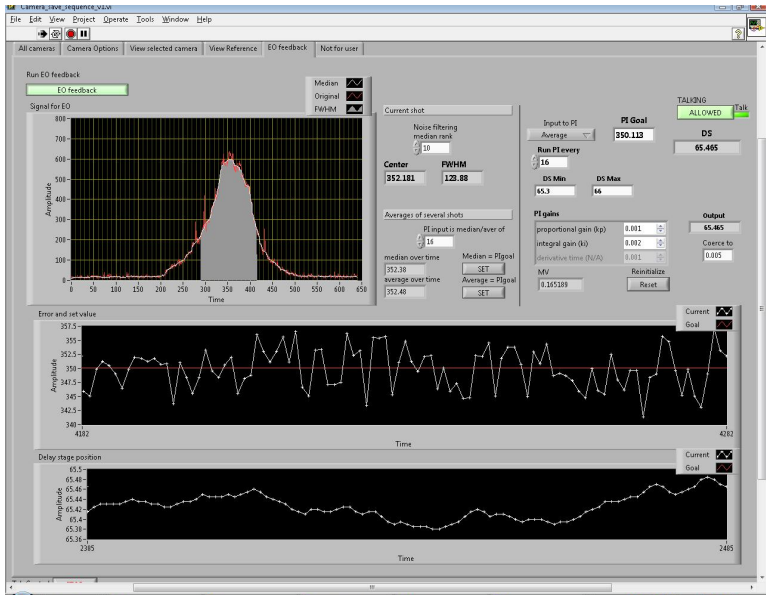

Figure 5.15. *Screenshot of the feedback software. The PID controller was used to maintain the EO peak (relative timing of the seed laser, upper-left) at a certain position to compensate for long-term drift. The delay stage moves the laser to keep the peak of the EO signal in the same position (its position is plotted at the bottom of the figure).*

EO signal itself can move during calibrating it is necessary to collect a series of images for each position. Calibration can then be carried out by fitting the average pixel position with the corresponding time shift of the delay stage. The calibration polynomial is a second order polynomial (because the chirped pulse is non-linear) and it is presented in Paper **III**.

5.10 Feedback

Paper **IV** presents results on stability improvement with the EO feedback system. The task of the feedback system, which consists of a programmed PID controller [52], is to keep the EO peak at the same pixel-position. Due to sensitivity of the controller to the jitter[14] only the proportional-integral part of the PID is used. The feedback does not react to every shot but to the average position of the peak. By examining the frequency components of the EO peak position recorded over 25 minutes it was determined that the dominant contributions to drift were at frequencies lower than those with a period of 16 seconds. It is thus possible to average the signal every 8 seconds, and to react

[14] The derivative part is sensitive to noise in the measured process variable.

to drifts in the average position. The PI is prevented from moving the delay stage unless the required shift is above certain threshold. This threshold corresponds to about 30 fs. At first, we were not sure if the long-term drift arose from the accelerator or the long fiber that connects the two laser hutches. The results presented in Paper **III** demonstrated that the long-term drift was caused by the accelerator and not the laser.

CHAPTER 6

SUMMARY AND OUTLOOK

This thesis introduces the papers that present some of the results achieved by a small group of people during four years of building and operating a test free-electron laser. An existing accelerator thermionic electron gun was operated as a photocathode gun for the purpose of running this test-FEL. Measurements of emittance and quantum efficiency were performed, and suitable operating parameters were found. These are presented in Paper **I**. To ensure the temporal overlap of electrons and the seed pulse an electro-optical spectral decoding system was built. This technique is non-interruptive and can be used to monitor the timing and bunch length online. Measurements with the EOSD system showed that the dominant cause of timing drifts between the seed laser and electrons was the accelerator and not the laser system. These results are given in Paper **III**. As the experience with the EOSD setup was positive, a similar system will probably be used for diagnostics in the future MAX IV injector. The EOSD system was used to develop a simple feedback system that stabilized the operation of the FEL. The feedback system, in combination locking to the grid frequency, reduced the timing rms jitter from well over 900 fs to 300. This is described in Paper **IV**. In practice, the reduction in timing jitter means lasing on every shot and better intensity stability. The scientific goal of this project, the generation of femtosecond coherent harmonics with circular polarization, has thus been achieved. These results are presented in Paper **II**.

Characterization of the transverse coherence and polarization properties of harmonics is currently in progress. This work will perhaps contribute even more to the aim of this project, that is gaining experience in operating free-electron lasers and collaboration within the FEL community, as one of the corner stones for a future MAX FEL. MAX FEL is a planned Ångström wavelength free-electron laser as a second-stage extension of the MAX IV project. Current enthusiasm in the scientific community with FEL light [53, 54] should be recognized and met with projects that promise similar possibilities. The advent

of light sources able to deliver nine orders of magnitude more photons with Ångström wavelengths than previously possible will open up new, unforseen areas of research.

During the work on the EOSD system, a simulation code for electro-optical setups, originally developed at DESY, was used and improved in several ways. This led to collaboration between several institutes in Europe with the aim of developing a complete, user friendly EO simulation code capable of simulating the majority of EO setups and materials.

APPENDIX

Stokes vector

There are several ways of describing the polarization of light. A good introduction to this is given in the book by Saleh and Teich [43]. In Paper **II** Stokes parameters were used to describe the polarization of the light produced.

For a wave propagating in the z-direction the E-field lies in the x-y plane. Such a monochromatic plane wave can be described as:

$$E_x = a_x \cos\left[\omega\left(t - \frac{z}{c}\right) + \phi_x\right] \tag{A.1}$$

$$E_y = a_y \cos\left[\omega\left(t - \frac{z}{c}\right) + \phi_y\right] \tag{A.2}$$

Depending on the difference $\phi = \phi_y - \phi_x$ and the values of a_x and a_y this leads to linearly, elliptically or circularly polarized light, which can generally be described by a polarization ellipse. An equivalent description of the polarization of light is a Stokes vector containing four Stokes parameters. The Stokes parameters are:

$$\begin{aligned} S_0 &= a_x^2 + a_y^2 \\ S_1 &= a_x^2 - a_y^2 \\ S_2 &= 2\,a_x\,a_y \cos\phi \\ S_3 &= 2\,a_x\,a_y \sin\phi \end{aligned} \tag{A.3}$$

as shown in Figure A.1. These four parameters satisfy the expression $S_0^2 = S_1^2 + S_2^2 + S_3^2$, where S_0 is proportional to the optical intensity of fully coherent light. For non-coherent light, generally $S_0^2 < S_1^2 + S_2^2 + S_3^2$. S_1 represents the linear polarization (in the horizontal or vertical plane). S_2 has the same meaning for linear polarization in a 45° rotated system. S_3 represents circular polarization and shows how much right circular polarization there is ($\phi = \pi/2$) relative to left circular polarization ($\phi = -\pi/2$). For a right circularly polarized wave the E-field on a certain incident plane is rotating clockwise (when looking into the direction from which the light is coming).

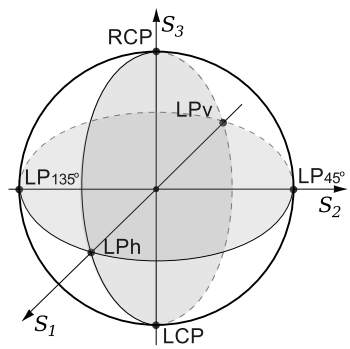

Figure A.1. *A Stokes vector on a Poincaré sphere of radius S_0 describes all possible polarizations. Pure polarizations are marked. RCP, LCP - right (left) circularly polarized. LP - linearly polarized with different angles of rotation relative to the horizontal (LPh).*

g [mm]	B_h(s=0) [T]	B_v(s=28) [T]
14.1	0.85625	0.62204
15.1	0.80742	0.57374
16.1	0.76515	0.52967
18.1	0.68646	0.45298
20.1	0.61509	0.38866
22.1	0.55078	0.33425
25.1	0.46633	0.26793
30.1	0.35271	0.18676
35.1	0.26640	0.13124
40.1	0.20098	0.09278
50.1	0.11408	0.04692
60.1	0.06455	0.02401
80.1	0.02052	0.00643
100.1	0.00649	0.00176

Table A.1. *Measurements of the radiator undulator fields performed at Helmholtz Zentrum Berlin. B_h corresponds to no shift, and B_v to the shift of 28 mm ($\lambda_w/2$).*

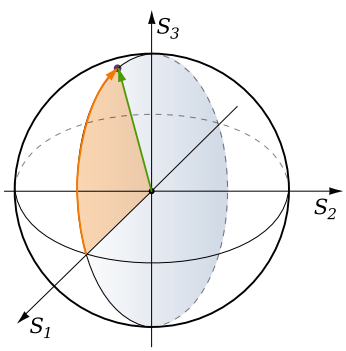

Figure A.2. *Stokes vector on a Poincaré sphere of radius S_0. For the radiator the Stokes parameter $S_2 = 0$. A shift of arrays moves the Stokes vector in that plane from $S_1/S_0 = 1$ towards $S_3/S_0 = 1$.*

Radiator gaps and polarization

The radiator undulator UE56 is an APPLE-II undulator that can change the gap g, and perform parallel motion of two diagonal arrays. It cannot perform anti-parallel shifts. Anti-parallel shifts give inclined linear polarization. In terms of Stokes vectors this means that $\phi = \frac{\pi}{2}$ and $S_2 = 0$ for all values of shifts and gaps of the undulator. It is possible to determine Stokes vectors by carrying out measurements on magnetic fields. The measurements of the fields were performed at Helmholtz Zentrum Berlin and are given in Table A.1. The vertical B_v, and horizontal, B_h, components of the field can be calculated by interpolation from the data in the table and using the fact that the field decreases exponentially with the gap. For each of the components we have:

$$\begin{aligned} B_h &= \exp\left(\frac{\ln B_{2h} - \ln B_{1h}}{g_2 - g_1}(g - g_1) + \ln B_{1h}\right) \\ B_v &= \exp\left(\frac{\ln B_{2v} - \ln B_{1v}}{g_2 - g_1}(g - g_1) + \ln B_{1v}\right) \end{aligned} \tag{A.4}$$

where B_1 and B_2 are values of the fields for gaps g_2 and g_1, chosen so that $g_1 \leqslant g < g_2$. B_v and B_h can be used to calculate effective B:

$$B_{\text{eff}}^2 = B_{h,\text{eff}}^2 + B_{v,\text{eff}}^2 \tag{A.5}$$

$$B_{\text{eff}}^2 = B_h^2 \cos^2\left(\pi \tfrac{s}{\lambda_w}\right) + B_v^2 \sin^2\left(\pi \tfrac{s}{\lambda_w}\right) \tag{A.6}$$

where s is the diagonal array shift. The radiator will have a fundamental mode wavelength:

$$\lambda = \frac{\lambda_w}{2\gamma^2}\left(1 + \frac{K^2}{2}\right) \tag{A.7}$$

where K is the K-parameter. Numerically,

$$K = 93.37287\ B_{\text{eff}}\ \lambda_w \tag{A.8}$$

The Stokes parameters can be calculated for given values of g and s since $B_{h,\text{eff}}$ and $B_{v,\text{eff}}$ are known, assuming $B_{v,\text{eff}} > B_{h,\text{eff}}$:

$$\left(\frac{S_3}{S_0}\right)^2 = \frac{2}{1 + \left(\frac{B_{v,\text{eff}}}{B_{h,\text{eff}}}\right)^2} \tag{A.9}$$

$$\left(\frac{S_1}{S_0}\right)^2 = 1 - \left(\frac{S_3}{S_0}\right)^2 \tag{A.10}$$

The requirement that the ratio of fields $\frac{B_{h,\text{eff}}}{B_{v,\text{eff}}}$ is r can be achieved by setting

$$s = \frac{\lambda_w}{\pi} \arctan\frac{1}{r}\frac{B_h}{B_v} \tag{A.11}$$

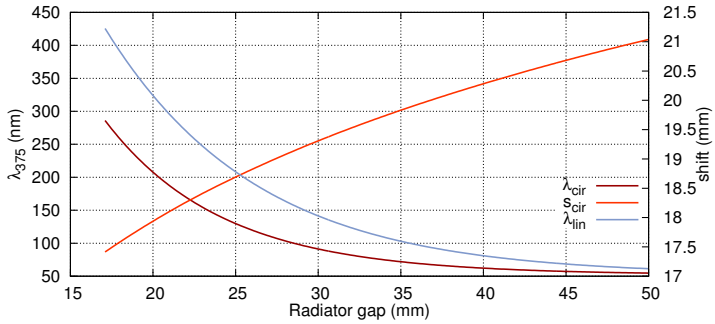

Figure A.3. *Wavelength of the fundamental for different radiator opening gaps for linear polarization ($s = 0$) and circular polarization. Wavelengths are calculated for an electron energy of 375 MeV. Values of the shifts required for circular polarization are given.*

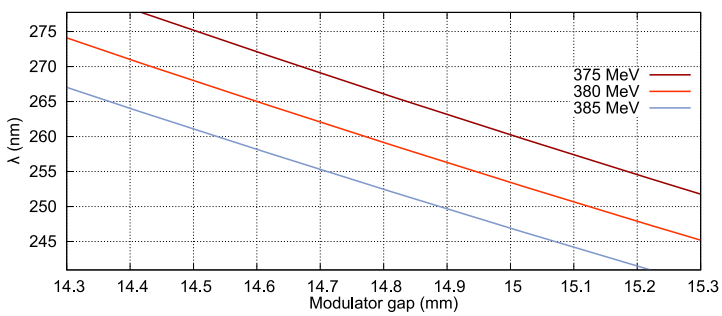

Figure A.5. *Wavelength of the fundamental as a function of modulator opening gap for different electron energies. This is an enlargement of the section of Figure A.4 in the range relevant for seeding.*

g [mm]	B [T]
10	0.9771
12	0.8540
16	0.6533
22	0.4380
30	0.2575
40	0.1324
60	0.0349

Table A.2. *Measurements of the modulator undulator fields performed at Helmholtz Zentrum Berlin. The period length of this undulator is 47.82 mm.*

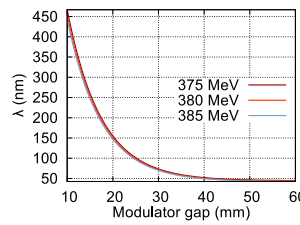

Figure A.4. *Wavelength of the fundamental for a wide range of modulator opening gaps.*

Modulator gaps

The modulator is a planar undulator with 30 periods. Measurements of the field inside the undulator as a function of the gap are presented in Table A.2 and were performed at Helmholtz Zentrum Berlin. Interpolation (A.4) was used to determine the B-field and subsequently the K-parameter and wavelength. The dependence of the wavelength on the gap is presented in Figures A.4 and A.5.

COMMENTS ON THE PAPERS

I **Photocathode operation of a thermionic RF gun**
This paper describes studies of the emittance of a thermionic gun adopted for photocathode operation. Measurements of the emittance, charge and quantum efficiency are presented. A good operating point for the test-FEL was found, and the emittance was shown to be satisfactory. I took part in the preparations, the measurements and the analysis, and contributed to parts of the manuscript.

II **Vacuum ultraviolet circularly polarized coherent femtosecond pulses from laser seeded relativistic electrons**
This paper describes the coherent production of harmonics in the VUV region with circular polarization down to 66 nm, and linear polarization down to 44 nm. I contributed to the development of the setup and participated in the experiments, the analysis of the results and the preparation of the manuscript.

III **Characterization of the arrival time jitter at the MAX-lab test-FEL using electro-optical spectral decoding**
This paper presents measurements on seed-pulse timing relative to electron bunch timing and bunch length measurements. It was concluded that the primary source of long term drifts is the accelerator. I took the initiative for the experiment, I was in charge of developing the setup and the measurements, and the analysis, and I was the main author of the paper.

IV **On-line arrival time and jitter measurements using electro-optical spectral decoding**
This paper describes a feedback system constructed to stabilize the overlap, which reduced the jitter from 900 to 300 fs RMS and ensured lasing on every pulse. I developed the feedback system, and participated in the experiments/measurements. I performed the analysis and was the main author of the paper.

REFERENCES

1. Pierce JR: *Theory of the beam-type traveling-wave tube*, Proceedings of the IRE, **35**(2):111–123 (1947), doi:10.1109/JRPROC.1947.226217.

2. Motz H: *Applications of the radiation from fast electron beams*, Journal of Applied Physics, **22**(5):527–535 (1951), doi:10.1063/1.1700002.

3. Phillips RM: *The ubitron, a high-power traveling-wave tube based on a periodic beam interaction in unloaded waveguide*, Electron Devices, IRE Transactions on, **7**(4):231–241 (1960), doi:10.1109/T-ED.1960.14687.

4. Phillips RM: *History of the ubitron*, Nuclear Instruments and Methods in Physics Research Section A: Accelerators, Spectrometers, Detectors and Associated Equipment, **272**(1-2):1–9 (1988), doi:10.1016/0168-9002(88)90185-4.

5. Madey JMJ: *Stimulated emission of bremsstrahlung in a periodic magnetic field*, Journal of Applied Physics, **42**(5):1906–1913 (1971), doi:10.1063/1.1660466.

6. Colson WB: *One-body electron dynamics in a free electron laser*, Physics Letters A, **64**(2):190–192 (1977), doi:10.1016/0375-9601(77)90712-5.

7. McClung FJ and Hellwarth RW: *Giant optical pulsations from ruby*, Journal of Applied Physics, **33**(3):828–829 (1962), doi:10.1063/1.1777174.

8. Hargrove LE, Fork RL, and Pollack MA: *Locking of He-Ne laser modes induced by synchronous intracavity modulation*, Applied Physics Letters, **5**(1):4–5 (1964), doi:10.1063/1.1754025.

9. Strickland D and Mourou G: *Compression of amplified chirped optical pulses*, Optics Communications, **56**(3):219–221 (1985), doi:10.1016/0030-4018(85)90120-8.

10. Ferray M, L'Huillier A, Li XF, Mainfray G, and Manus C: *Multiple-harmonic conversion of 1064 m radiation in rare gases*, Journal of Physics B: Atomic, Molecular and Optical Physics, **21**(3) (1988), doi:10.1088/0953-4075/21/3/001.

11. McPherson A, Gibson G, Jara H, Johann U, Luk TS, McIntyre IA, Boyer K, and Rhodes CK: *Studies of multiphoton production of vacuum-ultraviolet radiation in the rare gases*, Journal of the Optical Society of America B, **4**(4):595–601 (1987), doi:10.1364/JOSAB.4.000595.

12. Lambert G, Hara T, Garzella D, Tanikawa T, Labat M et al.: *Injection of harmonics generated in gas in a free-electron laser providing intense and coherent extreme-ultraviolet light*, Nature Physics, **4**(4):296–300 (2008), doi:10.1038/nphys889.

13. McNeil BWJ and Thompson NR: *X-ray free-electron lasers*, Nature Photonics, **4**(12):814–821 (2010), doi:10.1038/nphoton.2010.239.

14. Bonifacio R, Casagrande F, and Casati G: *Cooperative and chaotic transition of a free electron laser hamiltonian model*, Optics Communications, **40**(3):219–223 (1982), doi:10.1016/0030-4018(82)90265-6.

15. Chao AW and Tigner M, editors: *Handbook of Accelerator Physics and Engineering*, World Scientific Publishing Co. Pte. Ltd., 1st edition (2006).

16. Schmüser P, Dohlus M, and Rossbach J: *Ultraviolet and Soft X-ray Free-Electron Lasers*, Springer-Verlag Berlin Heidelberg (2008), ISBN 978-3-540-79571-1.

17. Atwood D: *Soft X-rays and extreme ultraviolet radiation*, Cambridge University Press (1999), ISBN 978-0-521-02997-1.

18. Wiedemann H: *Particle Accelerator Physics*, Springer-Verlag Berlin Heidelberg New York, 3rd edition (2007).

19. Sasaki S: *Analyses for a planar variably-polarizing undulator*, Nuclear Instruments and Methods in Physics Research Section A: Accelerators, Spectrometers, Detectors and Associated Equipment, **347**(1-3):83–86 (1994), doi:10.1016/0168-9002(94)91859-7.

20. Jackson JD: *Classical Electrodynamics*, John Wiley & Sons, Inc., 3rd edition (1999), ISBN 978-0-471-30932-1.

21. Colson WB, Dattoli G, and Ciocci F: *Angular-gain spectrum of free-electron lasers*, Physical Review A, **31**(2):828–842 (1985), doi:10.1103/PhysRevA.31.828.

22. Werin S: *Undulator physics and coherent harmonic generation at the MAX-lab electron storage ring*, Ph.D. thesis, University of Lund (1990).

23. Emma P et al.: *First lasing of the LCLS X-ray FEL at 1.5 Å*, In *Proceedings of PAC09, Vancouver, BC, Canada*, TH3PBI01 (2009).

24. Emma P, Akre R, Arthur J, Bionta R, Bostedt C, Bozek J, Brachmann A, Bucksbaum P, Coffee R et al.: *First lasing and operation of an Ångstrom-wavelength free-electron laser*, Nature Photonics, **4**:641–647 (2010), doi:10.1038/nphoton.2010.176.

25. Barletta WA, Bisognano J, Corlett JN, Emma P, Huang Z et al.: *Free electron lasers: Present status and future challenges*, Nuclear Instruments and Methods in Physics Research Section A: Accelerators, Spectrometers, Detectors and Associated Equipment, **618**(1-3):69–96 (2010), doi:10.1016/j.nima.2010.02.274.

26. Yu LH: *Generation of intense UV radiation by subharmonically seeded single-pass free-electron lasers*, Physical Review A, **44**(8):5178–5193 (1991), doi:10.1103/PhysRevA.44.5178.

27. Yu LH, Babzien M, Ben-Zvi I, DiMauro LF, Doyuran A et al.: *High-gain harmonic-generation free-electron laser*, Science, **289**(5481):932–934 (2000), doi:10.1126/science.289.5481.932.

28. Murphy JB and Pellegrini C: *Generation of high-intensity coherent radiation in the soft-X-ray and vacuum-ultraviolet region*, Journal of the Optical Society of America B, **2**(1):259–264 (1985), doi:10.1364/JOSAB.2.000259.

29. Bonifacio R, De Salvo Souza L, and McNeil BWJ.: *Emittance limitations in the free electron laser*, Optics Communications, **93**(3-4):179–185 (1992), doi:10.1016/0030-4018(92)90525-V.

30. Thorin S, Brandin M, Werin S, Goldammer K, and Bahrdt J.: *Start-to-end simulations for a seeded harmonic generation free electron laser*, Physical Review Special Topics-Accelerators and Beams, **10**(11):110701 (2007), doi:10.1103/PhysRevSTAB.10.110701.

31. Thorin S: *Studies on high brightness electron beams for short pulses and free electron laser*, Ph.D. thesis, Lund University (2009).

32. Svelto O and Hanna DC: *Principles of Lasers*, Plenum Press, New York and London, 4th edition (1998), ISBN 0-306-45748-2.

33. Murray JE and Lowdermilk WH: *Nd:YAG regenerative amplifier*, Journal of Applied Physics, **51**(7):3548–3556 (1980), doi:10.1063/1.328194.

34. Goldstein H, Poole C, and Safko J: *Classical Mechanics*, Addison Wesley, 3rd edition (2002), ISBN 0-201-65702-3.

35. *Wikipedia: Symplectic matrix* (2011), Accessed 23rd February 2011.

36. McDonald K and Russell D: *Methods of emittance measurement*, In M Month and S Turner, editors, *Frontiers of Particle Beams; Observation, Diagnosis and Correction*, volume 343 of *Lecture Notes in Physics*, pp. 122–132. Springer Berlin / Heidelberg (1989), doi:10.1007/BFb0018284.

37. Lapostolle PM: *Possible emittance increase through filamentation due to space charge in continuous beams*, IEEE Transactions on Nuclear Science, **NS-18**(3):1101–1104 (1971), doi:10.1109/TNS.1971.4326292.

38. Lee SY: *Accelerator Physics*, World Scientific Publishing Co. Pte. Ltd. (2004), ISBN 9789812562005.

39. Wilke I, MacLeod AM, Gillespie WA, Berden G, Knippels GMH, and Van Der Meer AFG: *Single-shot electron-beam bunch length measurements*, Physical Review Letters, **88**(12):124801 (2002), doi:10.1103/PhysRevLett.88.124801.

40. Steffen B: *Electro-optic methods for longitudinal bunch diagnostics at FLASH*, Ph.D. thesis, Hamburg University (2007).

41. Berden G, Gillespie WA, Jamison SP, Knabbe EA, MacLeod AM et al.: *Benchmarking of electro-optic monitors for femtosecond electron bunches*, Physical Review Letters, **99**(16):164801 (2007), doi:10.1103/PhysRevLett.99.164801.

42. Casalbuoni S, Schmidt B, and Schmüser P: *Far-infrared transition and diffraction radiation*, Technical report, DESY (2005).

43. Saleh BEA and Teich MC: *Fundamentals of photonics*, Pure and Applied Optics. John Wiley & Sons, Inc., 2nd edition (2007), ISBN 978-0-471-35832-9.

44. Boyd RW: *Nonlinear Optics*, Elsevier, 3rd edition (2008), ISBN 978-0-12-369470-6.

45. Van der Valk NCJ: *Towards terahertz microscopy*, Ph.D. thesis, Delft University of Technology (2005).

46. Marple DTF: *Refractive index of ZnSe, ZnTe, and CdTe*, Journal of Applied Physics, **35**(3):539–542 (1964), doi:10.1063/1.1713411.

47. Jiang Z, Sun FG, Chen Q, and Zhang XC: *Electro-optic sampling near zero optical transmission point*, Applied Physics Letters, **74**:1191 (1999), doi:10.1063/1.12349.

48. Schneider A, Neis M, Stillhart M, Ruiz B, Khan RUA, and Günter P: *Generation of terahertz pulses through optical rectification in organic DAST crystals: theory and experiment*, Journal of the Optical Society of America B, **23**(9):1822–1835 (2006), doi:10.1364/JOSAB.23.001822.

49. Kawase K, Hatanaka T, Takahashi H, Nakamura K, Taniuchi T, and Ito H: *Tunable terahertz-wave generation from DAST crystal by dual signal-wave parametric oscillation of periodically poled lithium niobate*, Optics Letters, **25**(23):1714–1716 (2000), doi:10.1364/OL.25.001714.

50. Jamison SP, MacLeod AM, Berden G, Jaroszynski DA, and Gillespie WA: *Temporally resolved electro-optic effect*, Optics Letters, **31**(11):1753–1755 (2006), doi:10.1364/OL.31.001753.

51. Jamison SP, Berden G, Phillips PJ, Gillespie WA, and MacLeod AM: *Upconversion of a relativistic coulomb field terahertz pulse to the near infrared*, Applied Physics Letters, **96**(23):231114 (2010), doi:10.1063/1.3449132.

52. Åström KJ and Murray RM: *Feedback Systems: An Introduction for Scientists and Engineers*, Princeton University Press (2010), ISBN 978-0-691-13576-2.

53. Seibert MM, Ekeberg T, Maia FRNC, Svenda M, Andreasson J et al.: *Single mimivirus particles intercepted and imaged with an X-ray laser*, Nature, **470**(7332):78–81 (2011), doi:10.1038/nature09748.

54. Chapman HN, Fromme P, Barty A, White TA, Kirian RA et al.: *Femtosecond X-ray protein nanocrystallography*, Nature, **470**(7332):73–77 (2011), doi:10.1038/nature09750.

Papers

PAPER I

Photocathode operation of a thermionic RF gun

S. Thorin, N. Čutić, F. Lindau, S. Werin and F. Curbis.

Nucl. Instrum. Meth. A **606**, 291–295 (2009).

Nuclear Instruments and Methods in Physics Research A 606 (2009) 291–295

Contents lists available at ScienceDirect

Nuclear Instruments and Methods in Physics Research A

journal homepage: www.elsevier.com/locate/nima

Photocathode operation of a thermionic RF gun ☆

S. Thorin [a,*], N. Čutić [a], F. Lindau [a], S. Werin [a], F. Curbis [b]

[a] MAX-lab, Lunds universitet, P.O. Box 118, SE-221 00 Lund, Sweden
[b] Hamburg University, Institute of Experimental Physics, Luruper Chaussee 149, 22761 Hamburg, Germany

ARTICLE INFO

Article history:
Received 9 April 2009
Received in revised form
23 April 2009
Accepted 1 May 2009
Available online 13 May 2009

Keywords:
Emittance measurement
BaO cathode
Photocathode gun
Quantum efficiency

ABSTRACT

The thermionic RF gun using a BaO cathode at the MAX-lab linac injector has been successfully commissioned for additional operation as a photocathode gun. By retaining the BaO cathode, lowering the temperature below thermal emission and illuminating it with a UV (263 nm) 9 ps laser pulse a reduced emittance and enhanced emission control has been achieved. Measurements show a normalised emittance of 5.5 mm mrad at 200 pC charge and a maximum quantum efficiency of 1.1×10^{-4}. The gun is now routinely switched between storage ring injections in thermionic mode and providing a beam for the MAX-lab test FEL in photocathode mode.

1. Introduction

Ultrahigh brightness low emittance electron guns are being developed at many laboratories using different techniques to produce a high quality electron beam. This is an important part of a linac based light source like a free electron laser. One of the most common and matured FEL injectors is the photocathode RF gun, where a short electron bunch is produced when a laser pulse hits a cathode surface. The electron bunch is then immediately accelerated in an RF cavity where emittance and energy spread are minimised.

At MAX-lab a test FEL facility is being constructed where the already existing injector and linear accelerator is used to test coherent harmonic generation and other related FEL techniques and concepts. The MAX-lab injector is usually used for injections into three synchrotron storage rings with a thermionic BaO cathode RF gun as electron source. This gun produces 100 ns long electron pulses with high emittance and energy spread and is therefore not suitable for the FEL test facility. In order to create the appropriate electron beam for the test FEL, the existing thermionic electron gun has been converted to a photocathode gun producing 9 ps long electron pulses with low emittance and energy spread. The gun has been successfully commissioned as a photocathode injector and now alters between thermionic injections into the rings and photocathode gun operations for the test FEL. In this paper characterisation of its performance is presented through emittance and charge measurements. The properties we want to explore is the quantum efficiency of the BaO cathode, i.e. how much charge is extracted depending on laser energy, and how the emittance is influenced by charge, RF phase in the gun cavities.

2. The FEL test facility

The MAX-lab injector [1] consists of the thermionic gun, a linear accelerator and a beam transport system. The gun is an RF gun with a BaO cathode surface and will be described in detail later in the paper.

The acceleration is done in two 5.2 m long linac structures each providing for a beam energy of up to 100 MeV. When the electrons have passed both linacs they are bent into a recirculator, turning them around 360° and passing them through the linacs one more time. This gives a total beam energy of around 400 MeV. The exit from the recirculator is done in a chicane and the electrons are then transported through a translating achromatic dogleg up the location of the undulators. The magnetic optics in the recirculator, chicane and dogleg provide enough first and second order momentum compaction for compressing the beam and producing a short spike of high current needed for the coherent harmonic generation.

Apart from the injector system, the FEL test facility needed an optical klystron [2] and a laser system to drive the seeding interaction. In a seeded FEL [3] and seeded harmonic generation, a high intensity laser pulse interacts with a high brightness electron bunch in an undulator causing the electrons to be energy modulated at the laser wavelength. The energy modulation will micro-bunch the electrons in a subsequent chicane after which they will radiate coherently in a following undulator tuned to either the modulation wavelength or a higher harmonic. The

☆ This work has partially been supported by the EU Commission in the sixth framework program, Contract no. MEST-CT-2005-020356, and the Swedish Research Council.

* Corresponding author. Tel.: +46 46 222 3964; fax: +46 46 222 4710.
E-mail address: sara.thorin@maxlab.lu.se (S. Thorin).

0168-9002/$ - see front matter © 2009 Elsevier B.V. All rights reserved.
doi:10.1016/j.nima.2009.05.004

optical klystron was provided by BESSY and consists of one planar and one APPLE II type undulator and an intermediate magnetic chicane.

Start-to-end simulations of the test FEL facility have determined some important parameters for the electron beam that put certain demands on the electron gun. From time-dependent GENESIS [4] calculations of the system it was found that an emittance of 5.5 mm mrad at a charge of 70 pC is sufficient to test the harmonic generation. Other than emittance, the peak current and energy spread of the electron bunch are of great importance, but as long as the gun produces enough charge these parameters are set in the acceleration and compression process.

3. Description of the gun system

The gun was originally designed as a thermionic RF injector for the synchrotron radiation storage rings at MAX-lab [6]. It is a $\frac{1}{2}+\frac{1}{2}+1$ cell structure operating at 3 GHz and a field of around 25 MV/m at the cathode surface and 80 MV/m in the main cavity. The electron source in the gun is a heated BaO cathode of 3 mm diameter. After the gun cavity the electrons reach a kinetic energy of 1.6 MeV. The layout of the gun structure can be seen in Fig. 1.

At the gun exit a solenoid magnet adjusts for the defocusing caused by space charge effects and different focusing due to the varying RF field. Tuning the solenoid becomes extra important when the gun is operated as a photoinjector with low emittance.

To reduce the low energy tail from the beam when using the thermionic cathode, an energy filter is mounted between the gun and the main accelerator, where the beam is bent in two 60° bending magnets. Between the dipoles a slit can filter out the low energy electrons.

To adapt the gun to a photocathode injector a 9 ps, 263 nm laser pulse is used to illuminate the cathode surface. The laser is synchronised to the RF voltage of the gun and the accelerator. The transmission of the energy filter depends on the energy spread in the electron beam, which in turn is influenced by the RF phase in the gun and the energy of the laser pulse. To switch from thermionic to photocathode operation the temperature on the cathode needs to be reduced from 1100 to 700 °C.

4. Laser system and timing

Pulses from a Ti:sapphire oscillator (790 nm, 93.7 MHz, *Femtolasers Synergy*) are stretched, amplified, compressed and tripled (*Thales Alpha* 10) to give a laser pulse that is used to shine on the cathode (263 nm, 9 ps pulse, 130 μJ, 10 Hz). The UV-pulse passes through a mechanical delay stage (for control of timing relative to the RF), a spatial filter and finally through focusing lenses before hitting the cathode (the laser spot-size diameter is about 1 mm).

The energy of the laser pulse can be reduced and is controlled and measured by a photodiode (previously calibrated with an energy-meter *Ophir Nova* II). To ensure phase stability relative to the RF, the optical oscillator is locked to the 32nd subharmonic of the 3GHz RF oscillator (with jitter of 0.3 ps). The position on the cathode can be changed by the last mirror (motorised) and controlled on a virtual cathode.

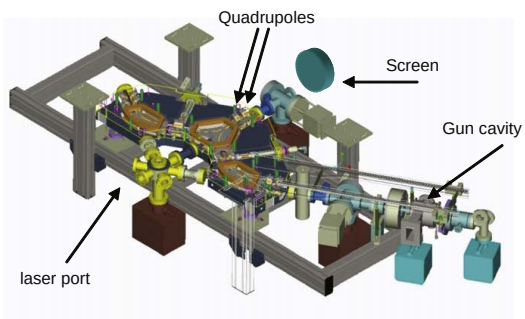

Fig. 1. Drawing of the gun and energy filter.

5. Experimental set-up

The emittance measurements were done with quadrupole scans [5] after the gun energy filter and the current measurements were made both after the gun cavity and a few meters down stream of the scanned quadrupole. A schematic view of the experimental set-up can be seen in Fig. 2.

For the quantum efficiency measurement the laser energy was varied between 0.2 and 130 μJ and the extracted charge was detected with a current transformer (CT) right after the gun cavity. The signal from the CT was recorded on an oscilloscope and the total charge was calculated from the integral of the current signal. For these very short electron bunches, it was checked that the integrated current from the CT still gave a valid measurement of the charge by cross-calibrating with a Faraday cup.

The quadrupole scans were made using the horizontally focusing quadrupole after the energy filter. The signal from the electrons hitting a fluorescent YAG screen was collected with a 10 bit IEEE1394 camera.

When investigating the emittance dependence on charge, the laser energy was varied in the same way as for the quantum efficiency scan and a quadrupole scan was recorded for each value.

For the RF phase scan, the laser arrival time in the RF cycle was varied between 5 and 50 ps using an optical delay stage. This corresponds to a scan over 50° in the part of the RF cycle that gives a detectable current from the gun.

6. Data analysis

To get some statistics in the emittance measurement, four images were saved for each quadrupole setting. The images were

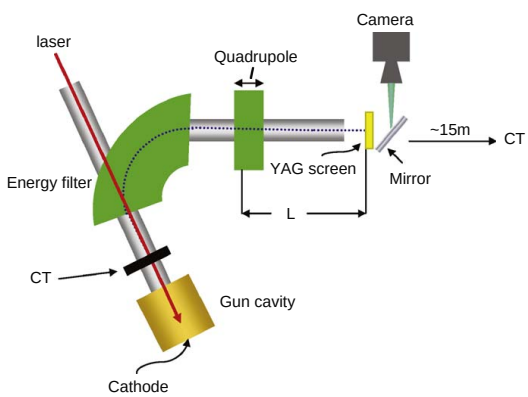

Fig. 2. Schematic image of the experimental set-up with the gun, energy filter, quadrupole, screen, camera and current transformer (CT).

then imported and analysed in MATLAB to extract the beam size. A parabolic fit was made of the beam sizes as a function of quadrupole k-value and from the parabola coefficients the emittance could be calculated.

The following formulas give the expression for rms beam size, σ as a function of emittance ε, Twiss parameters α and β, quadrupole length l, distance between the quadrupole and the screen L and quadrupole strength k. The beam size as a function of k-value turns into a second order polynomial where the emittance can be solved from the coefficients c_1, c_2 and c_3:

$$\sigma_x^2 = \varepsilon_x^2 L^2 l^2 \beta_0 k^2 + \varepsilon_x^2 Ll(L\alpha_0 - \beta_0)k + \varepsilon_x^2\left(\beta_0 - 2L\alpha_0 + L^2\frac{1+\alpha_0^2}{\beta_0}\right)$$
$$= c_1 k^2 + c_2 k + c_3$$

$$\Rightarrow \varepsilon = \frac{1}{L^2 l}\sqrt{c_1 c_3 - \frac{c_2^2}{4}}$$

Two different methods were used to calculate the beam size from camera images. In one of them a line of one or several pixel rows through the central part of the electron spot was projected on to one axis and fit with a Gaussian function. The fitted value for σ in the Gaussian function directly gives the beam size.

The other method works by calculating the second central moment of the electron distribution. To remove noise, the images are first median filtered and then thresholded at a level retaining 97% of the electrons. The square root of the second central moment gives the standard deviation, and is equivalent to σ in the case of a Gaussian distribution.

The two methods gave very similar results and the difference were within the error margin of the measurement.

The top half of Fig. 3 shows an example of a set of beam images from a quadrupole scan and in the bottom half the square of the corresponding beam sizes are plotted and fitted as a function of quadrupole strength.

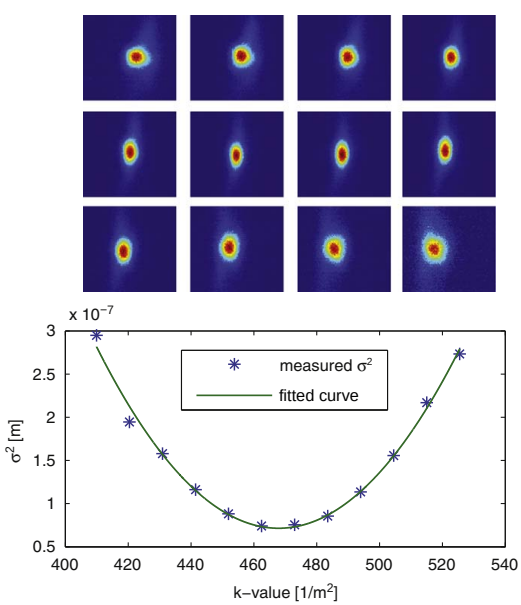

Fig. 3. Sample set of images at different k-values from a quadrupole scan (a). In (b) the square of the corresponding beam sizes are plotted as a function of quadrupole k-value, together with a second order polynomial fit. From the fit, the emittance of the beam can be calculated.

7. Results

The results from the quantum efficiency measurements can be seen in Fig. 4. Here the charge extracted from the cathode is plotted against the laser energy in one pulse. At low laser energy the data points follow a fairly linear pattern. The saturation that occurs at laser energies over 40 μJ can be explained by longitudinal space charge effects where the field from the extracted electrons becomes large enough to begin to cancel out the accelerating field in the gun cavity. This corresponds well to earlier observations of quantum efficiency in photocathode RF guns [7].

The resulting quantum efficiency of 1.1×10^{-4} is given by the slope of a line fitted to the measured points before saturation. This number is consistent with similar quantum efficiency measurements of BaO cathodes [8].

To examine the emittance dependence on charge, a measurement was made where the current collected from the cathode,

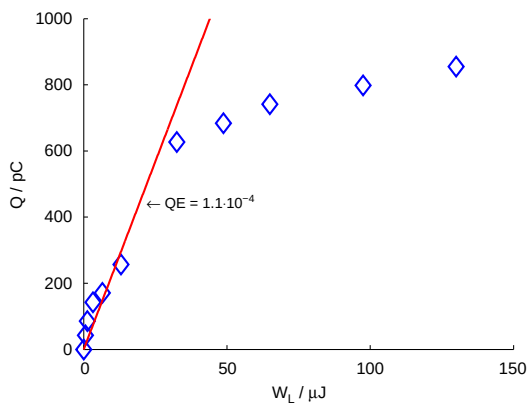

Fig. 4. Measurement of the BaO quantum efficiency.

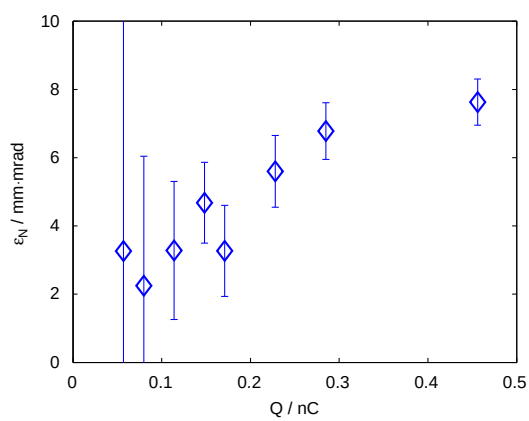

Fig. 5. Emittance as a function of extracted charge, measured on the CT after the gun.

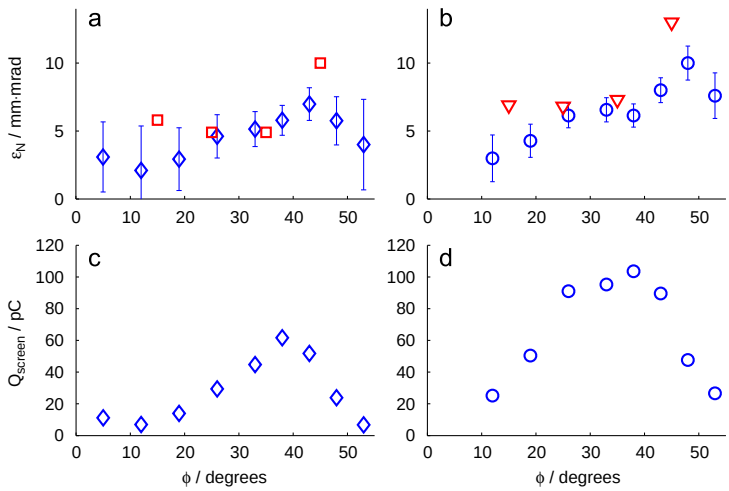

Fig. 6. The emittance as a function of RF phase in the gun is plotted for 110 pC (a) and 220 pC (b) extracted charge, together with simulation prediction from PARMELA. In parts (c) and (d) the corresponding charge transmitted through the energy filter is plotted. The error-bars in the emittance plots comes directly from the transmitted charge and shows that the results where most of the current has been scraped off cannot be trusted.

measured on the CT after the gun, was scanned by changing the laser energy. During this scan, the RF phase was kept at 20°, where simulations show a minimum emittance. The result is plotted in Fig. 5. The plot shows a linear dependence on charge as predicted by theory [9].

The large error-bars at low charge are due to a very poor signal at the screen, which leads to a high uncertainty in the measurement and analysis. PARMELA [10] simulations of the gun and energy filter give slightly higher emittance values than the measurement which could be explained by beam losses in the filter. The simulation does not fully explore the scraping off of electrons in the narrow vacuum tube which, if included, would result in a lower emittance.

The results from measuring the emittance dependence on RF phase can be seen in parts (a) and (b) of Fig. 6 together with predictions from the PARMELA simulation. The scan was made for two different gun charges, measured at the CT directly after the gun. In parts (c) and (d) the charge transmitted through the energy filter is plotted for the two data sets.

During one scan, the laser energy was changed to always give the same extracted charge from the gun, while the settings on the energy filter were kept constant. The RF phase influences both the focusing and the energy spread and together with the laser energy the space charge effects. For that reason the transmission through the filter varied a lot, which can be seen in parts (c) and (d) of the figure. High beam losses in the energy filter seem to give a lower resulting emittance in the analysis, why the results with very low transmission cannot be trusted. The error-bars in the emittance scan are directly calculated from the charge at the screen. The part of the scan where transmission was high gives a very good agreement with simulations.

The emittance due to the cathode is dependent both on the temperature of the cathode and the excess photon energy above the workfunction of the material. The normalised emittance is given by [11]

$$\varepsilon_{n,rms} = \frac{R}{2}\sqrt{\frac{2\Delta E}{3m_e c^2} + \frac{2kT}{m_e c^2}}$$

where R is the cathode radius, ΔE the excess photon energy and T the temperature of the cathode (m_e electron mass, c velocity of light, k Boltzmann's number). The workfunction of a BaO impregnated tungsten cathode can be as low as 2.4 eV [12] giving a ΔE of $4.7 - 2.4\,\text{eV} = 2.3\,\text{eV}$. The temperature of the cathode is given both by the pre-heating we apply to the cathode (around 1000 K) and potential transient heating. The dominating charge from the cathode increases linearly with deposited laser energy (and thus temperature) which is the signature of photoemission. Less than 10% of the charge is generated by other effects, including transient heating (with other temperature and/or time relations than photoemission). The pre-heating and the excess photon energy gives a background normalised emittance of 0.9 mm mrad, dominated by the excess photon energy, which is low enough to not influence the measured emittances.

Simulations have indicated that an emittance of 5.5 mm mrad and a charge of 70 pC is sufficient for the purposes of the FEL test facility, and according to these measurements, that specification can just be met. We believe we can reach even higher charges with an optimisation of the energy filter, since the measurements at the CT after the gun show that over 200 pC can be produced at an emittance of 5.5 mm mrad.

8. Conclusion

The MAX-lab thermionic RF gun has been successfully commissioned as a photoinjector for the test FEL facility and the two different modes of operation are easy and fast to switch between.

The performance of the gun as a photoinjector corresponds well to simulations and meets the necessary operating conditions needed for the test FEL.

The quantum efficiency of the BaO cathode was measured to be 1.1×10^{-4} and an emittance of 5.5 mm mrad can be achieved at a charge of over 200 pC measured after the gun.

The added flexibility of this RF gun is not only usable for the test FEL but also for producing short pulses of spontaneous radiation in the FEL undulators, increasing injection efficiency,

lowering losses in electron transport and for producing single bunch patterns in the storage rings.

References

[1] S. Werin, et al., Nucl. Instr. and Meth. A 445 (2000) 413.
[2] J. Bahrdt, et al., Undulators for a seeded HGHG-FEL at MAX-lab, EPAC, 2006.
[3] L.H. Yu, Phys. Rev. A 44 (1991) 5178.
[4] S. Reiche, Nucl. Instr. and Meth. A 429 (1999) 243.
[5] X. Qiu, et al., Phys. Rev. Lett. 76 (1996) 3723.
[6] S. Werin, et al., Nucl. Instr. and Meth. A 491 (2002) 307.
[7] J. Rosenzweig, et al., Nucl. Instr. and Meth. A 341 (1994) 379.
[8] B. Leblond, Nucl. Instr. and Meth. A 317 (1992) 365.
[9] K.-J. Kim, Nucl. Instr. and Meth. A 275 (1989) 201.
[10] L. Young, J. Billen, The particle tracking code PARMELA, PAC, 2003.
[11] N. Yamamoto, et al., J. Appl. Phys. 102 (2007) 024904.
[12] A.R. Shulman, T.S. Kirsanova, Sov. Phys. J. 14 (9) (1971) 1214.

Paper II

Vacuum ultraviolet circularly polarized coherent femtosecond pulses from laser seeded relativistic electrons

N. Čutić, F. Lindau, S. Thorin, S. Werin, J. Bahrdt, W. Eberhardt, K. Holldack, C. Erny, A. L'Huillier and E. Mansten.

Phys. Rev. Spec. Top. Accel. Beams **14**, 030706 (2011).

PHYSICAL REVIEW SPECIAL TOPICS - ACCELERATORS AND BEAMS **14**, 030706 (2011)

Vacuum ultraviolet circularly polarized coherent femtosecond pulses from laser seeded relativistic electrons

N. Čutić, F. Lindau, S. Thorin, and S. Werin
MAX-lab, Lund University, P.O. Box 118, S-221 00 Lund, Sweden

J. Bahrdt, W. Eberhardt, and K. Holldack
Helmholtz-Zentrum Berlin für Materialien und Energie GmbH, Wilhelm-Conrad-Röntgen-Campus, Albert-Einstein-Straße 15, D-12489 Berlin, Germany

C. Erny, A. L'Huillier, and E. Mansten
Physics Department, Lund University, P.O. Box 118, S-221 00 Lund, Sweden
(Received 9 December 2010; published 28 March 2011)

We have demonstrated the generation of circularly polarized coherent light pulses at 66 nm wavelength by combining laser seeding at 263 nm of a 375 MeV relativistic electron bunch with subsequent coherent harmonic generation from an elliptical undulator of APPLE-II type. Coherent pulses at higher harmonics in linear polarization have been produced and recorded up to the sixth order (44 nm). The duration of the generated pulses depends on the temporal overlap of the initial seed laser pulse and the electron bunch and was on the order of 200 fs. Currently, this setup is the only source worldwide producing coherent fs-light pulses with variable polarization in the vacuum ultraviolet.

DOI: 10.1103/PhysRevSTAB.14.030706 PACS numbers: 41.60.Cr, 42.65.Ky, 42.25.Ja

I. INTRODUCTION

Brilliant synchrotron radiation as produced in third generation storage rings is used in many user facilities worldwide featuring polarization control of the radiation using elliptical undulators. However, in the vacuum ultraviolet (VUV) and x-ray regime the synchrotron radiation is only partially coherent transversely, and multiparticle (gain) effects are nonexistent. Time resolved measurements are limited by the electron bunch length of typically 10–100 ps. Specific operation conditions, so-called low-alpha optics, provide bunch lengths on the ps scale [1]. The pulse duration can be further reduced with slicing techniques, where only a part of the bunch charge is used [2,3]. However, these pulses are temporally incoherent and the photon flux is limited.

Coherence properties as well as the photon flux can be significantly improved with free-electron lasers (FELs). Self-amplified spontaneous emission (SASE) FELs generate high peak brilliance, transverse coherence, short pulse lengths, and wavelengths [4–6] but since they start from noise they suffer from intensity variations, the signal longitudinally coherent only within the slippage length (shorter than the bunch length), and spiky resulting spectra. Introduction of a seed pulse (to avoid buildup from noise) significantly improves longitudinal coherence but creates new challenges to find a suitable seed source. Various seeding schemes have been proposed or carried out: seeding with high harmonics generated in a gas [7,8], self-seeding schemes [9], extraction of a harmonic after bunching at a long wavelength [high-gain harmonic generation (HGHG)] [10–13], or recently by echo-enabled harmonic generation [14].

The radiation from these sources [4–14] is linearly polarized since planar radiators were used. In the VUV regime, quarter wave plates converting linear to circular light are not available. One has to rely on reflection optics with low reflection efficiency and small tuning ranges. Thus, the linearly polarized radiation of existing FELs or the radiation from a high harmonic generation source cannot be easily converted to circular polarization using optics and helical undulators have to be used instead. The FERMI project which is under construction will have variably polarizing radiators [15].

Here, we show the first experimental results of combining temporal coherence, circular polarization, and fs pulse length down to 66 nm wavelength using the experimental layout depicted in Fig. 1. The same layout is also used to generate even higher harmonics in linear polarization (down to 44 nm).

The method we used is similar to high-gain harmonic generation (HGHG) as in Ref. [11] but with the differences that we use an APPLE-II type undulator as a radiator to produce harmonics with variable polarization, and our seed pulse is in the UV region. The modulator undulator (although tunable) is set to resonance with the seed laser frequency ω, whereas the radiator undulator fundamental

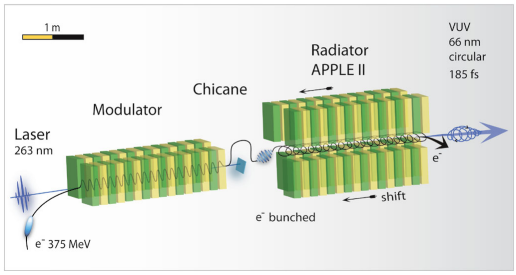

FIG. 1. Principle of the experimental setup of the MAX-lab test FEL (undulator section). Seeding occurs at 263 nm in the modulator which applies a horizontal field to the electron beam. After bunching in a dispersive section (chicane), the radiator emits circularly polarized coherent pulses up to the 4th harmonic at 66 nm.

mode is set to $n\omega$ ($n \geq 1$). Since the length of our radiator is such that the exponential amplification process just begins, we refer to this method as coherent harmonic generation (CHG) instead of HGHG.

II. EXPERIMENTAL SETUP AND METHODS

The complete experimental setup is shown in Fig. 2. The four major parts of our setup (the accelerator, the laser system, the undulator section, and the diagnostics) are presented in this section.

A. The accelerator

The test FEL facility is built around the MAX injector [16] which in normal operation provides the injection beam for the three storage rings at MAX-lab (MAX I, II, and III). The electron source is an rf gun [17] which can be operated both in thermal mode (ring injection) and in photocathode mode (test FEL)[18]. The electron bunches for the test FEL are created by a Ti:sapphire gun laser system. The pulse length is 10 ps. The rf accelerating phase in the gun is adjusted relative to the laser pulse to achieve minimum emittance. The main acceleration is done in two 3 GHz linac structures. The electron beam is recirculated such that the linacs are passed twice and a total energy of 375 MeV is reached. The beam exits the recirculator

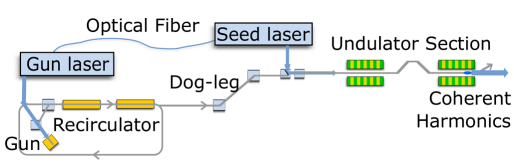

FIG. 2. Layout of the CHG-FEL test setup at MAX-lab, including electron accelerator, undulator section, the seed laser beam line, as well as the laser synchronization scheme.

through a chicane and is transported from basement level to ground level by a dog-leg. These latter systems provide the necessary R_{56} (momentum compaction) to compress the electron bunches.

After longitudinal compression the beam enters the test FEL beam line via a "half chicane" which lifts the beam 20 mm. This allows us to inject the seed laser beam on top of the electron bunch. A slight remaining dispersion is created by the half chicane, but the effect is negligible compared to the electron beam size. Focusing is achieved by a quadrupole doublet in the transport line upstream of the half chicane.

B. The laser system

The laser system, providing pulses for photocathode gun and seeding, is locked to the master rf oscillator by locking the master laser oscillator (Femtolasers Synergy, 93.71 MHz, 790 nm central wavelength, 13 nm FWHM bandwidth) with a jitter of about 0.2 ps. The laser oscillator pulses are stretched and split into two branches: one branch for the gun laser where it is subsequently amplified and tripled (263 nm, 10 ps, 500 μJ) to be used for the photocathode gun; the second branch of the oscillator pulse is guided through a 90 m polarization maintaining fiber to the seed laser where it is also amplified, compressed, tripled, delayed (to regulate arrival time), and focused into the modulator undulator (263 nm, 500 fs, up to 100 μJ). A small part of the infrared seed pulse before the tripling is sampled to be used for an electro-optical detection.

C. The undulator section

The undulator section consists of two undulators and a dispersive section. In the first undulator, which is called the modulator, the electrons interact with a 263 nm photon beam from the Ti:sapphire laser. For the current experiments it is operated at 10 μJ pulse energy (maximum 100 μJ) and 0.5 ps pulse length. The modulator must be resonant with the seed photon energy to imprint an energy modulation to the electron bunch. Within a dispersive section the energy modulation is subsequently converted into a spatial modulation. The required energy modulation $\Delta\gamma$ is determined by the natural relative energy spread σ_E. Beam bunching efficient enough for the CHG at a certain harmonic n requires $\Delta\gamma \geq \sigma_E \cdot n$, e.g., an energy spread $\sigma_E = 5 \times 10^{-4}$ requires an energy modulation of $\Delta\gamma = 1.5 \times 10^{-3}$ and 2.5×10^{-3} for the 3rd and 5th bunching harmonic, respectively.

The modulator is a pure permanent magnet planar device with a period length of 48 mm and 30 periods. At a minimum gap of 13.2 mm a K parameter of 3.52 is achieved. The radiator is a variably polarizing undulator of APPLE-II type, where APPLE stands for advanced polarizing photon light emitter [19]. This type of undulator consists of four permanent magnet rows, two above and two below midplane, which can be moved individually in

the longitudinal direction. Shifting two diagonal rows simultaneously in the same direction changes the polarization of the generated light. The state of polarization, horizontal, elliptical or vertical, is defined by the longitudinal shift. If the same rows are moved in opposite directions linearly polarized light is produced, where the inclination angle with respect to the midplane depends on the row shift. APPLE-II type undulators are used in many third generation synchrotron radiation facilities, because they deliver the highest horizontal on-axis fields among all planar elliptical devices. The radiator has 30 periods with a period length of 56 mm. At a minimum gap of 15.2 mm the maximum K parameters for horizontal, circular, and vertical polarization are 4.20, 3.44, and 2.98, respectively. The dispersive section between undulators (see Figs. 1 and 2) is built from four electromagnets where the magnet centers are separated by 400 mm. The length of each magnet is 120 mm. The magnets are powered in a way to produce a symmetric displacement of the electron trajectory. Separation of the electron trajectory from the common axis of both undulators in the chicane allows a laser beamstop to be placed inside. The beamstop prevents flooding of the diagnostics after the radiator with the strong seed laser pulse. The undulator section is followed by a 15° bending magnet separating the electron beam from the photon beam. The electrons are passed to the beam dump. THz pulses from the dump, as emitted by the short bunch, are used to verify the bunch compression.

D. Diagnostics

The main diagnostics used throughout the accelerator are current transformers and fluorescent screens with YAG crystals. The transverse overlap is secured by observing UV laser and electron bunch fluorescence on the YAG screens positioned before and after the modulator and overlapping them by controlling the position of the UV beam and electron bunches. Because of the long focal length (7 m) with which the seed laser pulse is focused, the UV beam has the approximately same small size on both screens while achieving focus inside the modulator. The electron beam size is approximately FWHM 2.5 and 1.2 mm and the UV beam size is 2.5 and 1.5 mm, before and after the modulator, respectively. The resolution of the two screens is 47 μm/pxl and 54 μm/pxl. The integral of a current transformer signal before the modulator undulator can be calibrated to a Faraday cup (at the dump) and thus provides an adequate charge reading.

The photon beam after the radiator is collected by a gold coated on-axis spherical mirror at 45° angle of incidence. The entrance slit of a Seya-Namioka monochromator (2400 l/mm grating) is placed at the vertical focus of the resulting astigmatic beam. This narrow line focus (~ 200 μm wide) allows us to open the entrance slit to the spectrometer to avoid cutting photons due to pointing variations in the electron beam. Pointing variations will instead appear as a small shift in wavelength because of a displacement of the source point. The spectrometer resolution is 0.28 nm with a 0.038 nm/pixel dispersion. The signal is recorded on a liquid nitrogen cooled CCD array (330×1100 pixels).

The precise temporal overlap between the electron bunch and the laser pulse is achieved by an electro-optical spectral decoding (EOSD) system [20] providing a sub-ps measure on the relative arrival times of the two pulses. Stability of the longitudinal overlap between the seed laser pulse and the electron bunch is improved by adding a feedback loop from the EOSD system to the seed laser delay stage. This ensures generation of higher harmonics in every shot [21]. Compression of the electron bunch is achieved by adjusting magnets and rf phases of the fields inside the linear accelerator for maximum compression to which fine adjustments are done while monitoring the width of the signal on the EOSD system. The measured bunch length is 1 ps (FWHM).

III. RESULTS AND DISCUSSION

A. Harmonics

CHG was observed in the linear mode of the radiator at all harmonics of the seed laser up to 6th (44 nm) at bunch charges of 25 pC and 2 Hz repetition rate. After switching to the circular mode by shifting two of the magnetic rows of the radiator, a circular coherent emission up to the 4th harmonic (66 nm) has also been recorded.

Single shot spectra taken at the 2nd harmonic (131 nm) in circular mode of the radiator are depicted in Fig. 3 revealing that a coherent signal occurs at every shot but

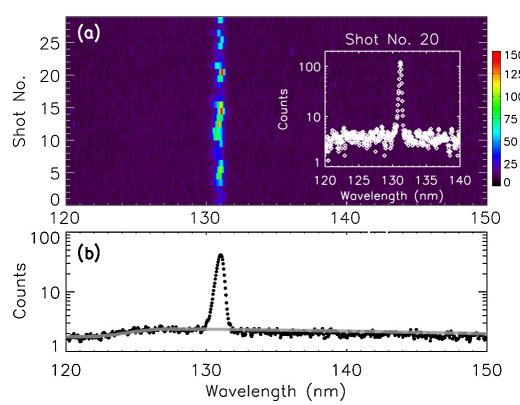

FIG. 3. A series of single shots taken at the 2nd harmonic at 131 nm (a) and the time averaged intensity over these 30 shots (b). A single shot spectrum is depicted in the inset. The calculated incoherent undulator harmonic was fitted for the pulse energy calibration [gray line in (b)]. These measurements were done before stability improvements on laser-electron overlap.

with fluctuating intensity. The appearing shot-to-shot variation in wavelength arises from the pointing stability of the radiator beam passing the monochromator at different positions through the large entrance slit of 1 mm. The highest coherent signal compared to the incoherent background was a factor of 78 at 25 pC bunch charge.

All measured coherent peaks at any harmonics exclusively occur due to radiation from the radiator while coherent emission from the dipole magnet (dump) is negligible. This fact is proven by the complete disappearance of the coherent signals in case of detuning the radiator (not shown). Changing the resonance of the radiator to the 4th harmonic of the laser, a corresponding trace of single shots could be recorded in the planar mode of the radiator as well, as shown in Fig. 4. Again, the signal compared to the incoherent light is fluctuating shot to shot but is typically smaller than 10. A pulse energy of 3.3 pJ could be estimated by calibrating each shot by the incoherent light appearing as the broad spectral feature beneath the narrow CHG peak. Changing the radiator shift parameter (see Fig. 1) to circular emission, CHG at the 4th harmonic (66 nm) of the same order of magnitude is observed (see Fig. 5). According to our calculations using the measured real field map in this case the degree of circular polarization yields $S3/S0 = 0.89$ at 66 nm. Here S3 and S0 are the Stokes vectors. The obvious difference to the ideal case $S3/S0 = 1.0$ is due to the large angular acceptance ($\geq 1/\gamma$) of the detection setup and due to a slight misalignment of the magnetic row phasing. The polarization degree of coherent light is assumed to be equally high as in the incoherent case as it is based on the circular trajectory of the electrons only. The polarization degree of spontaneous circular VUV light from the same type of undulator

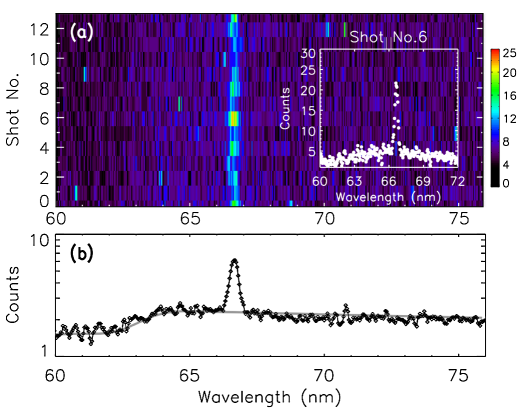

FIG. 4. A series of color coded single shots (a) and the average of them (b) recorded in the linear mode of the radiator at 66 nm. A single shot spectrum is plotted in the inset. The calculated incoherent undulator harmonics (light gray line) is fitted for the pulse energy calibration.

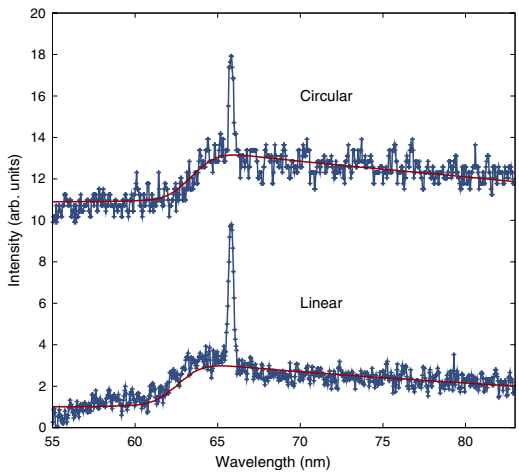

FIG. 5. Coherent 4th harmonic in circular and linear polarization. The full lines indicate the expected incoherent undulator harmonic according to SPECTRA simulations. The coherent gain is of the same order of magnitude in both cases and its difference is within the margins of overall stability fluctuations of the system.

(UE56) has been carefully measured and compared to undulator theory at the BESSY II storage ring [22]. The agreement is within the measurement accuracy of 3%.

Figure 6 shows coherent harmonics on wavelengths corresponding to the fourth and sixth harmonic of the seed pulse. The radiator is set to 131 nm so that these two harmonics are second and third harmonic of the radiator. The 44 nm signal is relatively weak. Harmonics with wavelengths of 88 and 52 nm in linear polarization were also produced but are not presented in this work.

The measured linewidth of the coherent photon pulses (Fig. 7) is broadened due to the resolution of the spectrometer. Taking the broadening into account and assuming transform limited Gaussian pulses, the pulse duration was

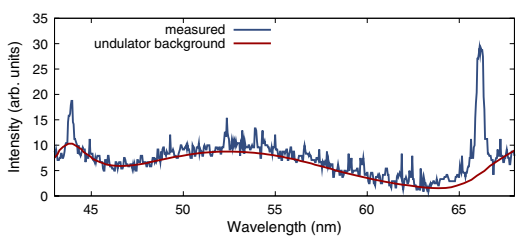

FIG. 6. Coherent fourth and sixth harmonic (66 and 44 nm) in linear polarization. Incoherent undulator harmonic background indicated separately. The radiator undulator is set to the second harmonic of the modulator undulator (131 nm).

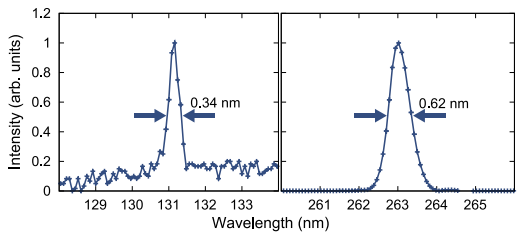

FIG. 7. Full-width half maximum linewidth of a peak measured at 131 and 263 nm is used to estimate the pulse length. Both spectra are normalized. The noise is less prominent on the fundamental due to higher intensity.

estimated to be 200 fs. Start-to-end simulations [23] suggested a pulse length of 150 fs (FWHM) which corresponds well to the measured values.

B. Energy modulation and microbunching

Clear evidence that the coherent signal originates exclusively from microbunching of the electron beam is given by Fig. 8. The disappearance of the signal is shown after detuning the resonance by 19 nm (0.6 mm gap change) which is larger than the bandwidth of the modulator's 1st harmonic. The shift is a factor of 60 larger than the measured laser bandwidth (0.3 nm at 263 nm) as depicted in the inset of Fig. 8.

The energy modulation depends on the spectral overlap of the laser beam and the spontaneous undulator radiation [24]. In the case of a narrow laser spectrum, a minimum width of $\Delta\lambda = \frac{\lambda}{N} = 8.8$ nm is expected, where λ is the resonance wavelength and N the number of undulator periods ($N = 30$). The measured resonance width is 11.2 nm wider than expected from the on-axis spectra in the inset of Fig. 8 (electron beam emittance ignored). However, detuning by 19 nm, there is no spectral overlap

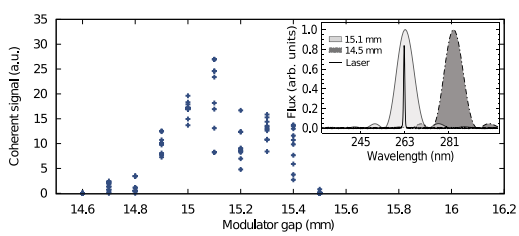

FIG. 8. Coherent signal for different gap settings of the modulator. For a given electron energy of 375 MeV the resonance was found at 15.1 mm gap. No energy modulation is observed at 0.6 mm detuning (19.4 nm), which is accompanied by disappearing coherent signal. Inset: Overlap of the measured laser spectrum with calculated spontaneous spectra of the modulator for two different gaps. The seed laser is resonant with a gap of 15.1 mm and off-resonant with a gap of 14.5 mm.

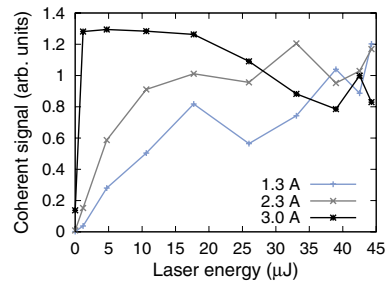

FIG. 9. Dependency of coherent signal at 133 nm on laser energy and chicane strength allows estimates of optimal parameters for energy modulation and compression.

between laser and undulator field anymore and bunching as well as CHG disappears as expected. The discrepancy between the expected and measured widths may be explained by suboptimal use of the length of the undulator. The central part will give the dominating modulation effect, and this gives a lower effective number of periods: $N_{\text{eff}} < N$, and thus a larger line width.

To determine optimal bunching conditions that produce strongest coherent signals, we scanned the dependence of the coherent signal at 131 nm relative to the strength of the chicane and the seed laser energy (Fig. 9). The signal strength was averaged over 20 consecutive shots after which the laser energy was changed. The results indicate overbunching with strong chicane and high laser energy since the coherent signal drops. The sensitivity to the laser energy sharply increases with chicane strength for small laser intensities. The driving currents through the chicane dipoles were 1.3, 2.3, and 3 A for which the corresponding R_{56} parameters were -0.091, -0.283, and -0.483 mm (respectively, calculated from field strengths and geometry).

IV. CONCLUSION

The MAX-lab test-FEL facility in Lund produces linearly and circularly polarized harmonics of a tripled Ti: sapphire system. The most interesting case of those, the 66 nm in circular polarization, with 25 pC of electron bunch charge is estimated to give 3 pJ in pulse energy. It is shown that microbunching is the main reason of coherent signal based on the disappearance of the signal for a detuned modulator undulator. The pulse length is estimated based on spectral width of the harmonics to be on the order of 200 fs. Further upgrades to the system are in progress to measure transverse coherence and directly characterize the polarization.

Although the original target for the MAX-lab test facility has been reached (extraction of the 5th harmonic in linear mode) and surpassed, measurements on the harmonics will continue. The main goal of the facility is investigation, preparation, and training for future FEL facilities,

such as the possible MAX IV FEL [25]. The project will during the coming year focus on the characterization of the generated CHG pulses, tests, and investigation of diagnostics and seeding with a focus of providing a firmer platform for the MAX IV FEL development.

ACKNOWLEDGMENTS

We thank A. Gaupp and A. Meseck for helpful discussions. This work is partly funded by IRUVX-PP, an EU cofunded project under FP7 (Grant Agreement No. 211285), the European Research Council (Grant ALMA 227906), and the Swedish Research Council.

[1] M. Abo-Bakr, J. Feikes, K. Holldack, P. Kuske, W. B. Peatman, U. Schade, G. Wüstefeld, and H.-W. Hübers, Phys. Rev. Lett. **90**, 094801 (2003).
[2] R. W. Schoenlein, S. Chattopadhyay, H. H. W. Chong, T. E. Glover, P. A. Heimann, C. V. Shank, A. A. Zholents, and M. S. Zolotorev, Science **287**, 2237 (2000).
[3] S. Khan, K. Holldack, T. Kachel, R. Mitzner, and T. Quast, Phys. Rev. Lett. **97**, 074801 (2006).
[4] T. Shintake *et al.*, Nat. Photon. **2**, 555 (2008).
[5] W. Ackermann *et al.*, Nat. Photon. **1**, 336 (2007).
[6] P. Emma *et al.*, Nat. Photon. **4**, 641 (2010).
[7] G. Lambert *et al.*, Nature Phys. **4**, 296 (2008).
[8] A. Azima *et al.*, in Proceedings of IPAC, Kyoto, Japan (2010), TUPE009, http://accelconf.web.cern.ch/AccelConf/IPAC10/papers/tupe009.pdf.
[9] J. Bahrdt, B. Faatz, R. Treusch, V. Miltchev, and R. Reininger, in Proceedings of FEL, Berlin, Germany (2006), MOPPH050, http://accelconf.web.cern.ch/AccelConf/f06/PAPERS/MOPPH050.PDF.
[10] L.-H. Yu, Phys. Rev. A **44**, 5178 (1991).
[11] L.-H. Yu *et al.*, Science **289**, 932 (2000).
[12] X. J. Wang, Y. Shen, T. Watanabe, J. B. Murphy, J. Rose, and T. Tsang, in Proceedings of FEL, Berlin, Germany (2006), MOAAU05, http://accelconf.web.cern.ch/AccelConf/f06/PAPERS/MOAAU05.PDF.
[13] A. Doyuran *et al.*, Phys. Rev. ST Accel. Beams **7**, 50701 (2004).
[14] D. Xiang *et al.*, Phys. Rev. Lett. **105**, 114801 (2010).
[15] Sincrotrone Trieste, The FERMI Conceptual Design Technical Report (2007), http://www.elettra.trieste.it/FERMI/index.php?n=Main.CDRdocument.
[16] Å. Andersson, M. Eriksson, S. Werin, S. Biedron, and H. Freund, Nucl. Instrum. Methods **445**, 413 (2000).
[17] B. Anderberg, Å. Andersson, M. Demirkan, M. Eriksson, L. Malmgren, and S. Werin, Nucl. Instrum. Methods **491**, 307 (2002).
[18] S. Thorin, N. Cutic, F. Lindau, S. Werin, and F. Curbis, Nucl. Instrum. Methods **606**, 291 (2009).
[19] S. Sasaki, Nucl. Instrum. Methods Phys. Res., Sect. A **347**, 83 (1994).
[20] N. Cutic, C. Erny, F. Lindau, and S. Werin, Nucl. Instrum. Methods **626**, 16 (2011).
[21] N. Cutic, F. Lindau, S. Werin, and E. Mansten, in Proceedings of FEL, Malmö, Sweden (2010), THOA4, http://accelconf.web.cern.ch/AccelConf/FEL2010/papers/thoa4.pdf.
[22] M. Weiss *et al.*, Nucl. Instrum. Methods **467**, 449 (2001).
[23] S. Thorin, M. Brandin, S. Werin, K. Goldammer, and J. Bahrdt, Phys. Rev. ST Accel. Beams **10**, 110701 (2007).
[24] A. A. Zholents and K. Holldack, in Proceedings of FEL, Berlin, Germany (2006), THPPH059, http://accelconf.web.cern.ch/AccelConf/f06/PAPERS/THPPH059.PDF.
[25] N. Cutic, M. Eriksson, F. Lindau, S. Thorin, and S. Werin, in Proceedings of FEL, Malmö, Sweden (2010), WEPA11, http://accelconf.web.cern.ch/AccelConf/FEL2010/papers/wepa11.pdf.

PAPER III

Characterization of the arrival time jitter at the MAX-lab test-FEL using electro-optical spectral decoding

N. Čutić, C. Erny, F. Lindau and S. Werin.

Nucl. Instrum. Meth. A **626–627**, 16–19 (2011).

Nuclear Instruments and Methods in Physics Research A 626–627 (2011) 16–19

Contents lists available at ScienceDirect

Nuclear Instruments and Methods in Physics Research A

journal homepage: www.elsevier.com/locate/nima

Characterization of the arrival time jitter at the MAX-lab test-FEL using electro-optical spectral decoding

Nino Čutić [a,*], Christian Erny [b], Filip Lindau [a], Sverker Werin [a]

[a] MAX-lab, Lunds Universitet, P.O. Box 118, SE-221 00, Lund, Sweden
[b] Department of Physics, Lund Institute of Technology, P.O. Box 118, SE-221 00, Lund, Sweden

ARTICLE INFO

Article history:
Received 6 August 2010
Received in revised form
15 October 2010
Accepted 19 October 2010
Available online 29 October 2010

Keywords:
FEL seeding
Bunch arrival
Electro-optical spectral-decoding
Timing jitter
Bunch length

ABSTRACT

Electro-optical spectral decoding is used as an online diagnostic tool at the MAX-lab test-FEL to characterize the arrival time of electrons relative to the seed-laser pulse, measure the jitter between them and to measure the relative width of the electron bunch in order to optimize compression. Frequency characteristics of the jitter are presented. The measurements are used to get information on possible causes of the jitter and accompanying drifts.

1. Introduction

The interplay of light and electron bunches inside an undulator is crucial for free electron lasers (FEL) and the spectral and coherence properties of the light they produce. One common way of improving these properties is seeding, in which an electron bunch entering the undulator is copropagated with a high power laser pulse (seed laser pulse). Knowing the electron bunch arrival time relative to the seed-laser pulse with good precision is a prerequisite for an easier and faster start of operation of the seeded free electron laser. One would like to avoid long time-scans to achieve overlap. Aside from the timing, timing stability, low drifts and jitter are also crucial. Characterization of the jitter and its possible origins are of importance for further stability improvements of the system. Knowledge about the possible origins of the jitter allows upgrades to the system to compensate or remove them. Further, a better stability ensures generation of harmonics on every shot, and with an averaging detector this improves signal to noise sufficiently enough to allow generation and detection of higher order coherent harmonics than without stabilization.

At MAX-lab, as a part of the test-FEL project [1], an Electro-Optical Spectral Decoding (EOSD) system was built and used to position the seeding pulse in time as well as to monitor the compression of the electron bunches online. One major advantage of this technique is that it is non-destructive and thus allows for online operation. The EOSD technique was chosen because of: its low cost (since the laser was already available), the possibility to do single shot measurements and its relative simplicity to build. The first measurements with this technique were done at laser based THz sources; and later for electron bunches [2,3]. Several similar techniques have been proposed or tested. Those include: temporal decoding [4–6], spatial decoding [7–9] and spectral up-conversion [10] for bunch length measurements of short electron bunches.

2. Experimental setup

The test-FEL (Fig. 1) consists of three major parts: the electron accelerating section, the laser system and optical klystron (modulator, chicane and radiator). The EOSD is placed upstream of the optical klystron.

The MAX-lab accelerator provides 380 MeV electron bunches with a charge of 30 pC and a repetition rate of 10 Hz (currently limited to 2 Hz due to radiation safety). The linac RF system is driven by a 3 GHz RF oscillator. The accelerator is a recirculating structure with each electron bunch passing twice through the linacs. Compression of the electron bunch has to be performed in order to get sufficiently high peak current (charge density) within the seed laser pulse window. This is achieved by operating first linac at a certain phase of the RF cycle (8° off-crest) and the compression happens in the chicane following the recirculator [11].

The laser system consists of two amplifiers (Thales Alpha 10) referred to as the gun-laser and the seed-laser (Fig. 1). They share a

* Corresponding author.
E-mail address: nino.cutic@maxlab.lu.se (N. Čutić).

0168-9002/$ - see front matter © 2010 Elsevier B.V. All rights reserved.
doi:10.1016/j.nima.2010.10.090

N. Čutić et al. / Nuclear Instruments and Methods in Physics Research A 626–627 (2011) 16–19

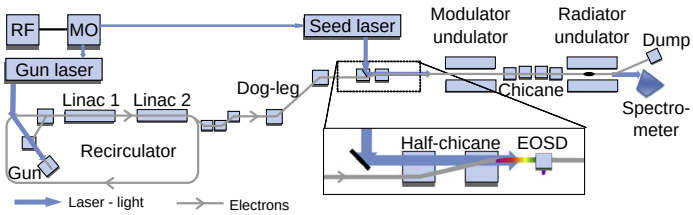

Fig. 1. The test-FEL setup. The electron bunch created by the laser pulse on a photocathode gun passes an energy filter (two dipoles) and a recirculator where it passes through the two linacs twice. The chicane right after the recirculator compresses it. After the dog-leg/transport the electrons are displaced in the half-chicane to insert laser pulses from the seed-laser. Its energy is modulated inside the modulator undulator, turned into density modulation in the chicane and finally radiated on a higher harmonic inside the radiator undulator. The electrons are dumped and the UV radiation continues to the spectrometer. The position of the chamber and the crystal (EOSD) is shown in the enlarged section. The insertion mirror shown in enlarged part before the half-chicane is used as an entrance for all optical pulses.

common master oscillator (Femtolasers Synergy, Ti:Sapphire, 790 nm, 13 nm bandwidth, 93.68 MHz). Its repetition rate is locked to the 3 GHz RF signal with a relative jitter of 0.1 ps by controlling the length of the oscillator cavity. The oscillator signal is stretched and split into two parts, feeding two chirped pulse amplifiers. The first amplifier (the gun-laser) is frequency tripled (263 nm, 10 ps, 150 μJ) and used for photo-cathode operation. The second part is transmitted through a 90 m polarization maintaining fiber to the seed-laser amplifier, where, after amplification and compression, the pulse is again split into two parts. One part is the infrared pulse (IR) used for the EOSD, and the second part is tripled to ultraviolet (UV, 263 nm, 110 μJ, 350 fs) and used for seeding the FEL. The IR (5 nm FWHM bandwidth) pulse is stretched to 3.3 ps FWHM and overlapped temporally and spatially with the UV pulse. Their timing is controlled with two separate delay stages. One stage controlling the timing for both (UV and IR) pulses relative to the electron bunches. The other stage shifts the UV pulse relative to the IR until they overlap. This is ensured using a difference frequency generation in a separate non-linear crystal. The relative timing to the electrons determined this way is sufficient to operate the FEL and any residual offset can be adjusted once the FEL is running.

EOSD is a scheme in which an electron bunch passing close to a crystal temporarily causes a change in the birefringence of the crystal and thus a polarization change in a chirped laser pulse passing through the crystal. The change in polarization is encoded into a part of the chirped pulse that was at the moment of electron bunch pass within the crystal. The chirped pulse is subsequently sent through a set of polarizing optics and a spectrometer where it is possible to determine the timing of the electron bunch relative to the laser pulse and to estimate the bunch length. Fig. 2 shows the EOSD setup within the test-FEL, positioned between insertion "half-chicane" and the modulator-undulator (see Fig. 1). The UV pulse (not shown) and IR-diagnostic pulse are both injected into the vacuum system with a mirror inside the upstream "half-chicane". They are pointing in slightly different directions so that after 6.5 m of propagation the IR passes through the crystal while the UV continues into the modulator-undulator overlapping with the electrons. This allows for continuous monitoring with EOSD while the FEL is running. Any influence due to the proximity of the crystal and the mirror behind it (that is used to reflect the IR pulse out of the vacuum system) on the generation of coherent harmonics because of electron wake-fields has not been observed. The birefringent crystal is 5×5 mm^2 ZnTe, 1 mm thick and cut in the (1 1 0) plane. The crystal axis [0 0 1] is collinear with the polarization plane of the IR pulse, in Fig. 2 orthogonal to the paper (coming out). The [−1 1 0] axis is pointing in direction of the THz field (up, in the figure). The crystal, the mirror and a reverse biased photodiode (not shown in Fig. 2) are mounted on a translatable stage, inside the vacuum system. The stage enables them to be positioned transversely arbitrarily close to the electron beam path.

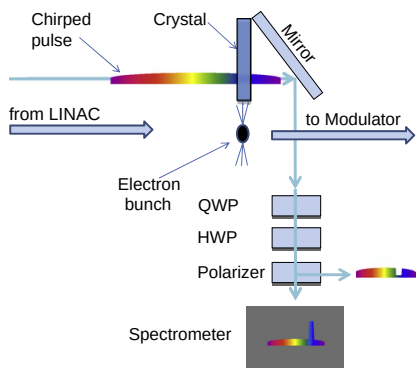

Fig. 2. The EOSD setup. The linear polarization of the chirped laser pulse is modified in the crystal by the electron bunch induced birefringence. Analysis of the pulse is performed outside of the vacuum system next to the crystal chamber. The chamber extends approximately 5 cm along the transport line.

The photodiode connected to an oscilloscope is used for approximate timing with a precision of ~200 ps. The mirror reflects the IR beam out of the vacuum system to the EOSD detector. The energy of the IR pulse reaching the crystal is below 1 μJ.

The EOSD detector consists of a quarter-wave plate (QWP, corrects residual birefringence of the crystal), a half-wave plate (HWP, sets the polarization of interest to S-polarization of the grating inside the spectrometer), and a Glan-laser polarizer (filters polarization of interest). The beam is then focused into a spectrometer. The spectrometer grating is an Al-reflective holographic 1200 mm^{-1} grating and the detector is a 10 bit CMOS Firewire camera (Pointgrey Firefly MV) with 6 μm pixels.

3. Results

Measuring the jitter time, the spectrum of that jitter and the electron bunch width first required calibration of the system. The chirp of the laser pulse was determined using EOSD itself. Knowledge about the chirp is a calibration since it is correspondence between pixel number (wavelength) and the time of arrival. This was done by controlling the position in time of the laser pulse (using the delay stage) and monitoring the position of the signal from electrons within the spectrum. Fig. 3-left shows that the chirp is not linear. The second order polynomial fit to these data was used as the calibration for further measurements. In order to eliminate the possibility that the drifts in time distort the calibration, this calibration was repeated with same end results.

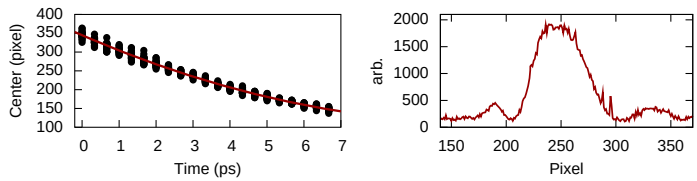

Fig. 3. The calibration data (left) and a typical signal (right). The calibration data and the fitted polynomial determine time to wavelength mapping. The wavelength is determined from the pixel number on the CMOS, and the signal is moved with the delay stage that regulates timing of the laser pulses relative to the electrons. Higher times correspond to earlier arrival of the IR pulse. Twenty spectra were acquired at each position. A typical signal profile after subtraction of the reference image (the image that contains information about hot pixels and oscillator spectrum for that delay stage position, see the text) is shown to the right. The signal to noise ratio varies depending on the electron bunch compression. The sidepeaks present in the signal are attributed to the frequency mixing effects between the terahertz pulse and the optical pulse.

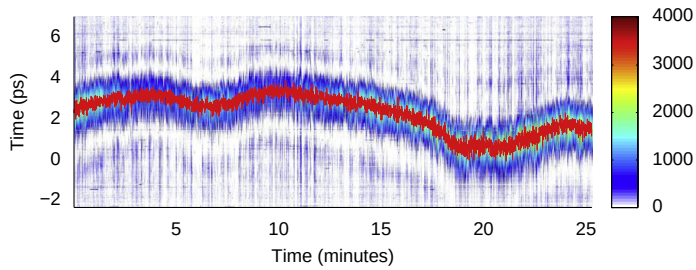

Fig. 4. A 25-minute measurement of the relative delay between the laser pulse and the electron bunch. Each spectrum is shown on the vertical axis and color mapped by intensity. Each pixel of each spectrum is mapped to corresponding time (using the calibration polynomial in Fig. 3) and then relinearized to be shown on this image. On top of the scan shown with a superimposed line is the calculated central point for each shot.

All the measurements were done in a near cross-polarized configuration (half-wave plate is offset by $\sim 1^{\circ}$) which means that the spectrum of the chirped laser pulse is slightly visible even when no electrons are present. The background spectrum had to be subtracted from each measurement image. The background spectrum was recorded for all positions of the delay stage used in the calibration because of small pointing fluctuations of the mirrors carried by the delay stage. The wavelength in the spectrometer is changing along the horizontal axis of the camera sensor. The image with the signal from electrons and the laser background minus the image with just the laser (reference image) and then projected on the horizontal axis (summation of values of pixels) is our signal. Beforehand, the radiation damaged "hot pixels" are determined (defined as the 1% of the pixels with highest values in a dark frame) and their values are replaced by the median value of neighboring pixels in the reference frames and signal frames. A typical signal during a measurement is shown in Fig. 3-right.

In order to determine the spectral characteristics of the relative jitter between the arrival times of the electron bunch and the laser pulse, a scan with 3000 shots was done. Spectra (with subtracted background) are linearized in time and shown for all shots in Fig. 4. The calculated center of the signal is shown in red (superimposed). The signal shows noticeable drifts limiting a stable operation of the FEL. The RMS jitter of the total signal position is 910 fs and that reduces to ~ 200 fs if low frequency drifts would be completely taken away (moving average subtracted).

Fig. 5 shows the mean square frequency analysis of the signal featuring two peaks: one corresponding to low frequency drifts, and a 0.45 Hz peak. The 0.45 Hz peak contributes about 40 fs to the jitter. Its origins were determined later to be connected to an undersampled power grid frequency since a trigger lock to the power grid in later work removed the peak. For the low frequency drifts, initially, thermal drifts in the fiber guiding the oscillator

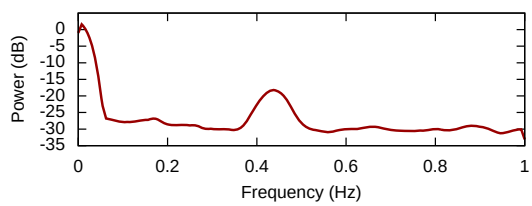

Fig. 5. Mean square (power) spectrum of the jitter that is shown in superimposed line in the Fig. 4. The spectrum was obtained using the Welch method and the function *msspectrum* in MATLAB software.

pulse to the seed-laser were suspected. The electron bunch width and the arrival time are correlated. Fig. 6 shows the width of the EOSD signal (related to bunch length) and arrival time of the electrons. This suggests that electron-energy instabilities inside the recirculator might be the leading cause of these drifts. Any other source of these drifts that is not linked to the accelerator (e.g. optical fiber drifts) would cause arrival time shifts that are independent from compression in the accelerator (the width of the signal). The spectrum of the width is very similar to the spectrum of arrival time, i.e. the 0.45 Hz peak is present (this is not shown).

The EOSD measurements of the electron bunch width in our case are limited by the frequency mixing between the chirped optical pulse and the frequencies of the terahertz pulse generated by the electron bunch inside the crystal. This is a known limitation of EOSD [12]. The correspondence between measured width versus "real" width improves for longer electron bunches and less chirped optical pulses. Simulations show that in our case measurements overestimate the real bunch length by about 6% for shorter

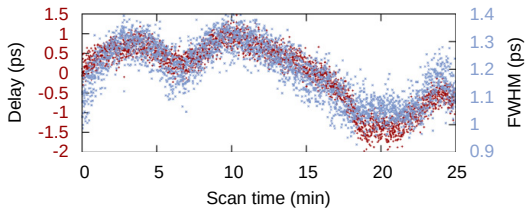

Fig. 6. The timing of the electron bunch and the width of the EOSD pulse shown on different scales in order to demonstrate correlation. The connection between compression and electron-bunch arrival time suggests that the main contributions to the jitter are not laser system related but accelerator related.

measurements (1 ps), and about 3% for longer (1.3 ps). This implies that the "real" bunch width is between 0.95 ps FWHM and 1.26 ps FWHM depending on the measured width and assuming a Gaussian shape of the bunch.

4. Conclusion

By measuring the arrival time jitter using a single pulse electro-optical technique that can run online with the FEL and comparing it to the bunch width it was determined that the origins of drifts are coming from the accelerator. Initially the laser system was suspected (thermal drifts in a long optical fiber) to be the main contributor to the loss of overlap between the electron bunches and the seed-laser pulse. The time jitter shows a clear peak at 0.45 Hz which is probably due to undersampling of higher frequencies in the accelerating system. The most dominant contribution to the jitter are drifts below 0.05 Hz. This provides an opportunity to feedback control on low frequencies in order to improve the overlap between the electrons and the seed laser pulses (although the compression would still be "drifting"). Of course, since EOSD also gives information about compression, there is a possibility of additional feedback which would compensate and keep the compression constant. The EOSD technique is relatively cheap and showed to be functioning robustly during operations of the test-FEL, it also facilitated a simple search for the overlap and setup of electron bunch compression and became a prerequisite for daily operations.

Acknowledgements

The authors thank Erik Mansten and Bernd Steffen for valuable discussions. This work has been partially supported by the EU Commission in the sixth framework program. Contract no. MEST-CT-2005-020356, and the Swedish Research Council. C.E. acknowledges the support of the European Research Council (Grant ALMA 22906).

References

[1] S. Werin, N. Cutic, F. Lindau, S. Thorin, J. Bahrdt, K. Holldack, et al., The test FEL facility at MAX-lab, in: Proceedings of the FEL09, Liverpool, UK, TUPC034, 2009.
[2] T. Tsang, V. Castillo, R. Larsen, D.M. Lazarus, D. Nikas, C. Ozben, et al., J. Appl. Phys. 89 (2001) 4921 . doi:10.1063/1.1358322.
[3] I. Wilke, A.M. MacLeod, W.A. Gillespie, G. Berden, G.M.H. Knippels, A.F.G. van der Meer, Phys. Rev. Lett. 88 (12) . doi:10.1103/PhysRevLett.88.124801.
[4] G. Berden, A.F.G. van der Meer, S.P. Jamison, B. Steffen, E.A. Knabbe, B. Schmidt, et al., Single shot longitudinal bunch profile measurements at FLASH using electro-optic techniques, in: Proceedings of the EPAC06, Edinburgh, UK, TUPCH026, 2006.
[5] B. Steffen, Electro-optic methods for longitudinal bunch diagnostics at FLASH, Ph.D. Thesis, Hamburg University, 2007.
[6] B. Steffen, V. Arsov, G. Berden, W.A. Gillespie, S.P. Jamison, A.M. MacLeod, et al., Phys. Rev. Spec. Top. Accel. Beams 12 (3) (2009) 032802. doi:10.1103/PhysRevSTAB.12.032802.
[7] A. Cavalieri, D. Fritz, S. Lee, P. Bucksbaum, D. Reis, J. Rudati, et al., Phys. Rev. Lett. 94 (11) (2005) 114801 . doi:10.1103/PhysRevLett.94.114801.
[8] T. Srinivasan-Rao, M. Amin, V. Castillo, D.M. Lazarus, D. Nikas, C. Ozben, et al., Phys. Rev. Spec. Top. Accel. Beams 5 (4) (2002) 42801 . doi:10.1103/PhysRevSTAB.5.042801.
[9] X. Yang, T. Tsang, T. Rao, J.B. Murphy, Y. Shen, X.J. Wang, Appl. Phys. Lett. 95 (2009) 231106. doi:10.1063/1.3266919.
[10] G. Berden, A.F.G. van der Meer, S.P. Jamison, A.M. MacLeod, W.A. Gillespie, P.J. Phillips, Longitudinal electron beam diagnostics via upconversion of THz to visible radiation, in: Proceedings of the FEL09, Liverpool, UK, WEPC80, 2009.
[11] S. Thorin, M. Brandin, S. Werin, K. Goldammer, J. Bahrdt, Phys. Rev. Spec. Top. Accel. Beams 10 (2007) 110701. doi:10.1103/PhysRevSTAB.10.110701.
[12] S.P. Jamison, G. Berden, W.A. Gillespie, A.M. MacLeod. Limitations of electro-optic measurements of electron bunch longitudinal profile, in: Proceedings of EPAC08, Genoa, TUPC042, 2008.

PAPER IV

On-line arrival time and jitter measurements using electro-optical spectral decoding

N. Čutić, F. Lindau, S. Werin and E. Mansten.

Proceedings of FEL10, Malmö, Sweden, THOA4 (2010).

ON-LINE ARRIVAL TIME AND JITTER MEASUREMENTS USING ELECTRO-OPTICAL SPECTRAL DECODING

Nino Čutić†, Filip Lindau, Sverker Werin, MAX-lab, Lund
Erik Mansten, Department of Physics, Lund University, Sweden

Abstract

Electro-optical spectral decoding was used to on-line monitor the arrival time of the electron bunches relative to the seed laser pulse at the test FEL facility at MAX-lab. An infrared chirped pulse coming from the seed laser is influenced by an electron bunch induced birefringence in a ZnTe birefringent crystal and the arrival time is determined from its spectrum. The possibility of running simultaneously with the FEL allowed for a feedback scheme to be built to compensate for the long term drifts in the system. Also, the whole system (the accelerator and the lasers) were synchronized to the power grid frequency. This lock increased the stability and was monitored by the EO setup. Measurements of the bunch length were performed and their correlation with arrival time pointed towards main contributors to the jitter in the system.

INTRODUCTION

The MAX-lab test-FEL recently demonstrated generation of coherent harmonics at 66 nm (circular and linear polarization) 53 nm and 44 nm (linear polarization) combining seeding at 263 nm and relativistic electron bunch from MAX-lab linac using APPLE II type undulators. One of the crucial components of the test-FEL is a device based on electro-optical spectral decoding (EOSD) which allowed on-line monitoring of the bunch compression and the electron bunch arrival time relative to the seed laser pulse. Since the electron bunch and the seed laser pulse are of subpicosecond duration a technique that allows timing measurements with better precision than what can be achieved with photodiodes ($\sim$200 ps) is needed. Electro-optical schemes using the interaction of a terahertz field created by traveling electron bunch and a laser pulse passing through a crystal have been developed (first in laser based sources of THz radiation) and later modified and applied for measurements of bunch arrival time and duration at accelerators [1, 2, 3]. These technique have shown to be robust enough and comparatively cheap since a required laser pulse for seeded facilities is readily available without major extra costs.

* This work has been partially supported by the EU Commission in the sixth framework program, Contract no. MEST-CT-2005-020356, and the Swedish Research Council.

† Corresponding author; nino.cutic@maxlab.lu.se

EXPERIMENTAL SETUP

The Test-FEL

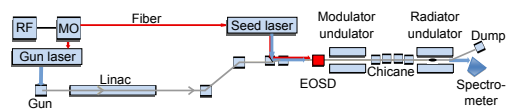

Figure 1: Position of the EOSD within the test-FEL setup. The test-FEL spans about 90 meters in length. The gun laser pulse is used on photo-cathode gun and the seed laser pulse is used for seeding inside the modulator undulator. The master oscillator (MO) is locked to the RF signal generator (3 GHz). Part of the infrared pulse in seed laser is taken and stretched to 3.3 ps FWHM and used for EOSD.

The test-FEL setup is shown in Fig. 1 and consists of 3 major parts [4, 5]. The accelerator (photocathode gun and a recirculating linac, that accelerates 30 pC electron bunches to 375 MeV), the optical klystron (modulator undulator, chicane and radiator undulator) and the laser system (master optical oscillator 93.7 MHz, 790 nm, 13 nm bandwidth, locked to 3 GHz RF clock), two laser amplifiers referred to as the gun laser (263 nm, 10 ps, 10 Hz) and the seed laser (263 nm, 350 fs, 10 Hz, 150 μJ;) which are positioned in separate laser hutches optically connected by a polarization maintaining fiber that is transferring the oscillator pulse to the seed laser. The energy of the electron bunch is modulated inside the planar modulator undulator due to interaction with the seed laser pulse. It is therefore crucial that the seed laser pulse is transversally and longitudinally (in time) overlapped with the electron bunch, thus the main part of the EOSD system (EOSD chamber) is placed in front of the modulator undulator.

The EOSD System

The EOSD system consists of 3 major parts and operates using a small sample ($<$ 1 μJ) of the amplified seed laser pulse (before it is tripled to UV). The first part of the system is in the seed laser hutch and it consists of a separate stretcher built for IR pulses, focusing optics (telescope focusing onto the crystal inside the EOSD chamber, 6.5 m focus), delay stages (a main delay stage controlling the delay of both pulses relative to the electron bunch, and a UV delay stage shifting the UV pulse relative to the IR pulse) and a UV-IR overlap monitor based on difference frequency generation (DFG). The second part is the EOSD

chamber which is the only part of the EOSD system placed in vacuum. The chamber holds the crystal, a mirror and the photodiode (for rough timing) on a translation stage (used to position the crystal transversally arbitrarily close to the passing electron bunch). The third part is the EOSD detector consisting of the polarization optics and a spectrometer which is placed outside of the vacuum system right next to the chamber. Transverse overlap is controlled by two motorized mirrors before the seed laser pulse enters the vacuum system and it is monitored using two YAG screens positioned before and after the modulator undulator. IR (for EO) and UV (for seeding) pulse are pointing in slightly different directions so that the IR pulse passes through the crystal and hits the mirror behind the crystal (that sends it out of the EOSD chamber into EOSD detector) while UV pulse passes next to the crystal and overlaps with the electron bunch. There is also a slight difference in focusing since the UV pulse is focused in the middle of the modulator undulator.

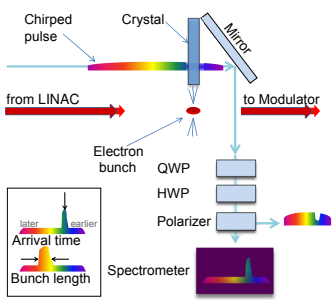

Figure 2: The EOSD chamber and detector. The crystal and the mirror are placed inside the vacuum system on a translatable stage. IR chirped pulse passes through the crystal and is reflected out of the chamber to the detector. The detector consists of polarization optics (Quarter-wave plate, half-wave plate and Glan-laser polarizer) which filters the polarization of interest and the spectrometer. Based on the position of the peak in the signal on spectrometer it is possible to determine the arrival time of the electron bunches relative to the IR pulse and estimate the length of the electron bunch from the width.

Figure 2 shows what is described as the EOSD chamber and EOSD detector. A linearly polarized chirped (3.3 ps FWHM, 5 nm FWHM bandwidth, 790 nm central wavelength) pulse from the seed laser passes through a ZnTe crystal (cut in (110) plane, $5 \cdot 5$ mm^2, 1 mm thickness, with [-110] axis pointing up in the figure). The electric field from the electron bunch induces birefringence in the crystal and the crystal changes polarization of the part of the chirped pulse that is currently passing through it. The pulse hits the mirror after the crystal and leaves the vacuum system going into the detector. A quarter-wave plate (QWP) is used to eliminate any residual birefringence in the crystal when there are no electrons present. The half-wave plate (HWP) rotates the polarization of the pulse to the S-polarization of the grating of spectrometer that follows.[1] The pulse passes through the Glan-laser polarizer that filters only the polarization that is not supposed to be present in the pulse (if there are no electrons). The pulse is then sent to the spectrometer. The spectrometer is built using Al-holographic grating 1200 mm^{-1} with Pointgrey Firefly MV camera.

Image Analysis

The images captured by the spectrometer's camera are used to determine the timing of the electrons relative to the UV pulse (since the IR and UV have a fixed delay). The images are median filtered and dead pixels (determined as 1% highest value pixels in dark frame) are attributed the median value of their neighboring pixels. The background spectrum (present without electrons) is subtracted. All pixels in a region of interest are vertically summed and thus resulting curve is considered as signal. Calibration of the pixels to time is done using the signal from electrons themselves and scanning the delay stage that controls the delay of the laser pulse relative to the electrons. This effectively "walks" the peak over pixel values. A polynomial of second order is then used to determine timing of each pixel. A polynomial of second order is used because the chirp of the laser pulse (current frequency along the duration of the pulse) is slightly non-linear. This calibration is repeated several times to remove the contribution from drifts during the calibration itself.

Feedback

To stabilize the drifts a feedback routine is built that controls the position of the peak of the signal so that it is always on desired position (the laser pulse is at desired timing relative to the electrons). This is done by controlling the main delay stage (Thorlabs 150 mm). The routine uses a PI controller whose input is the pixel value of the peak of the signal and parameters are determined using Ziegler-Nichols method. The PI is not compensating on every shot but responds slower after every n shots; this is usually 16 or 8 shots, where the repetition rate is 2 Hz. The change of the delay stage position is suppressed if the required change is less than what would correspond to 30 fs shift in time.

50 Hz Lock

To reduce jitter caused by the 50 Hz grid frequency, the triggering of devices should be synchronized to this frequency. The synchronization is done by a microcontroller sending a trigger pulse every 5 grid cycles to obtain the desired 10 Hz pulse rate. The grid AC is transformed down to

[1] Actually, HWP is offset by about $\sim 1^\circ$ so that even when no electrons are passing the spectrometer can notice the background spectrum of the laser pulse. This is called near-crossed polarizer setup and has certain advantages.

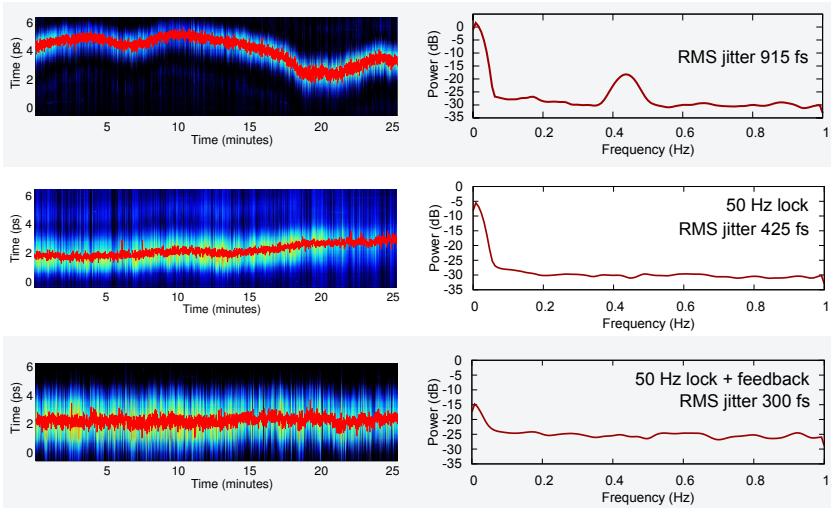

Figure 3: Measurements of the long term drifts and jitter (left) and the corresponding power spectra of the arrival time (right). On the left side each spectrum captured (about 3300 of them, corresponding to 25 minutes) is converted to time and shown vertically using the false coloring of the signal's intensity. The central position is calculated and shown in red overlaid curve. The right side shows power spectra of these red curves. Top - without feedback; middle - with 50 Hz lock; bottom - with EOSD feedback and 50 Hz lock. The RMS jitter drops respectively from 915 fs to 425 fs to 300 fs.

12 V and connected to a comparator input of the microcontroller. When the voltage reaches a set value, an interrupt is generated. To eliminate spurious response around the set value, the microcontroller inhibits the comparator for 16 ms after the first detected crossing.

The trig pulse output from the microcontroller is connected to the trig input of the main delay/trigg generator of the FEL, a Masterclock from Thales Laser, ensuring that the whole system is synchronized to 50 Hz. A jitter of a few tens of microseconds, i.e. less than a degree, has been measured on the 10 Hz trig compared to the grid frequency, mostly due to high frequency components overlaid the 50 Hz signal (from e.g. RF noise). Heavy low-pass filtering would reduce this jitter, but the additional gain in system stability would be minimal.

MEASUREMENT AND RESULTS

Jitter Measurements and Feedback

The first measurements of jitter were done without the feedback and the 50 Hz lock. Figure 3 on left shows three images each showing a series of spectra through time. A spectrum from spectrometer is shown vertically and converted to time using the calibration polynomial. All three measurements last 25 minutes. Overlaid red line shows the center of each shot. Figures on the right show a power spectrum of the overlaid line determined by using the function *msspectrum* in MATLAB software. The frequencies on the right span to 1 Hz because the repetition (sampling) frequency is 2 Hz. The top two images belong to measurement done without any feedback. The middle two are with the 50 Hz lock is active. And the lower two are with 50 Hz lock active and a PI controller controlling the position of the peak at certain point. Noticeable improvement in stability is visible. Turning on the 50 Hz lock reduces the RMS jitter from 915 fs to 425 fs. It also removes the 0.45 Hz peak which was an influence of the power grid to the system probably on higher frequencies that was undersampled. This still leaves majority of long term drifts below 0.05 Hz which are lowered 10 dB more by the delay stage feedback giving final RMS jitter of 300 fs

Drifts and Bunch Length

Measurements of the bunch length are done simply by determining the width of the EOSD signal. Their main limitation is the large thickness of the ZnTe crystal. Larger thickness of the crystal influences the effective cutoff frequencies of the system (makes the EOSD "slower" due to mismatch between the propagation of the THz and optical pulses through the crystal) but improves the signal strength (larger thickness means more polarization rotation).

Figure 4 shows the correlation between the measured pulse width and arrival time for the case without any feedbacks (overlaid red curve from top left in Fig. 3). Assuming the Gaussian shape of the bunch, simulations show that our setup overestimates the real bunch length by 6% for shorter measurements (1 ps) and 3% for longer (implying the bunch width to be ranging from 0.95 ps to 1.26 ps

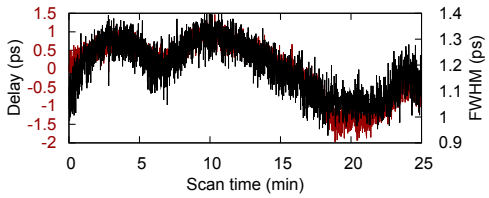

Figure 4: Correlation between the arrival time of electron bunches and the width of the EOSD signal (approximately bunch length, see text). This correlation points to the accelerator as the main cause of drifts.

FWHM). Obvious correlation between the arrival time of electrons and their compression is a sign that the drifts are coming from the linac and not the laser system. If the laser system was the main cause of drifts the compression would not correlate so good with the drifts. During these measurements no automatic control of the compression was used (this requires further work on accelerator side) and is mainly due to hardware contraints.

CONCLUSION

We used electro-optical spectral decoding to online monitor the compression and arrival time of the electrons relative to the seed laser pulse. A lock to grid frequency and feedback controlling the arrival pulse allowed the reduction of the RMS jitter from 915 fs to 300 fs. These improved conditions were sufficient to achieve the coherent harmonic generation in every shot which effectively increased the signal to noise on the detection side and allowed measurement of lower harmonics (53 and 44 nm). Drift compensation was done controlling the seed laser pulses although the main cause of the drifts comes from instabilities of the accelerator which was determined by observing the correlation between the electron bunch arrival time and the bunch length.

ACKNOWLEDGEMENTS

Authors acknowledge the use of some of the MATLAB routines to simulate the EOSD developed by Dr. Bernd Steffen which were further modified to estimate the real bunch length from the measured width.

REFERENCES

[1] I. Wilke, A. M. MacLeod, W. A. Gillespie, G. Berden, G. M. H. Knippels and A. F. G. van der Meer, "Single-Shot Electron-Beam Bunch Length Measurements", Phys. Rev. Lett. **88**, 124801 (2002). doi:10.1103/PhysRevLett.88.124801

[2] T. Tsang, V. Castillo, R. Larsen, Lazarus D. M., D. Nikas, C. Ozben, "Electro-optical measurements of picosecond bunch length of a 45 MeV electron beam", J. Appl. Phys. **89** 4921 (2001). doi:10.1063/1.1358322

[3] B. Steffen, PhD thesis "Electro-Optic Methods for Longitudinal Bunch Length Diagnostics at FLASH", (2007).

[4] S. Werin, J. Bahrdt, N. Čutić, C. Erny, K. Holldack, A. L'Huillier, F. Lindau, E. Mansten, S. Thorin, "First Results of Coherent Harmonic Generation at the MAX-Lab test-FEL", Proc. of the FEL10, Malmö, Sweden, WEOA4, 2010.

[5] S. Werin, N. Čutić, F. Lindau, S. Thorin, J. Bahrdt, K. Holldack, "The test-FEL facility at MAX-lab", Proc. of the FEL09, Liverpool, UK, TUPC034, 2009.